THE SURFACE ELECTRONIC AND MAGNETIC PROPERTIES OF RARE EARTH SILICIDES AND IRON NANOCLUSTERS USING METASTABLE DE-EXCITATION SPECTROSCOPY

Charles William Woffinden

Thesis submitted for the degree of DOCTOR OF PHILOSOPHY

Department of Physics,
University of York

January 2010

Abstract

Metastable de-excitation spectroscopy (MDS) is a technique that probes the surface of materials using metastable atoms (in our case He 2^3S) to produce an electron energy spectrum that is characteristic of the surface's electronic structure. These metastable atoms can, additionally, be spin polarised, enabling the magnetic properties of a surface to be probed by comparing the electron emission yield produced by the two spin states of the incident metastable atoms relative to the magnetisation direction of the sample.

The aim of this research project is to use and develop a current instrument capable of performing MDS and spin-polarised MDS (SPMDS). This instrument has been used for surface analysis to probe and characterise the electronic and magnetic surface properties of a variety of materials.

In particular, the electronic characteristics of the reconstructions between rare earth silicide nanowires and the implications these have to the surface and nanowire formation has been investigated.

The surface electronic and structural differences of 2-dimensional when compared to 3-dimensional rare earth silicides have been studied and compared to results from ultraviolet photoelectron spectroscopy (UPS) and density functional theory (DFT) to determine where particular states arise. A process of deconvoluting the MDS spectrum that arises from the resonance ionisation and Auger neutralisation spectrum to reveal the effective density of states has been demonstrated and compared to a DFT predicted density of states, and found to agree.

The magnetic, electronic and structural properties of ferromagnetic iron nanoclusters deposited on silicon substrates have been investigated using a range of techniques including SPMDS and MDS. An asymmetry in the SPMDS spectrum has been observed with a large magnitude, suggesting an asymmetry in the spin-split density of states above the bulk iron value.

All developments to the instrumentation are also detailed, including the construction of an *in situ* magneto optic Kerr effect (MOKE) magnetometer.

Contents

List of Tables

List of Figures

Acknowledgements

I have thoroughly enjoyed my Ph.D. and there are a number of people who have made it possible and much more entertaining than it might otherwise have been.

I would like to thank my supervisor, Steve Tear for all his guidance, advice and support.

I am extremely grateful for the support of all the department and the Surface Physics Group, especially Andrew Pratt, Chris Eames, Chris Bonet, Andrew Vick, Tomas Stanton and the Magnetic Materials Research Group.

The help of support staff in the department has been vital, especially Rich Armitage and Dave Coulthard for all their technical know-how and leak-testing expertise.

I acknowledge the Engineering and Physical Sciences Research Council for funding this project. Thanks for the cash.

I would finally like to thank my family for their support, and my friends, especially Zoë, for always providing me with a bit of escapism from the world of physics.

Declaration

The work presented in this thesis is based on my own research except where it is explicitly stated in the text. No part of this work has previously been submitted for any other qualification.

Most of the MDS data presented within this thesis were obtained with the kind assistance of Dr. Andrew Pratt.

Charles Woffinden

Publications

The following publications have arisen so far from the work presented in this thesis:

Metastable de-excitation spectroscopy and scanning tunneling microscopy study of the 2×4 and 2×7 reconstructions of Ho on Si(001). Physical Review. B. 78, 155430 (2008),

Structural and electronic properties of rare-earth nanowires. Materials Research Society Symposium Proceedings, 14, 1144-LL04-24 (2009),

Surface electronic structure of two- and three-dimensional holmium silicide on Si(111). Physical Review. B. 79, 245406 (2009),

Enhanced surface spin polarization of Fe nanoclusters Transactions on Magnetics - Conferences, *Submitted* (2009),

Hydrogen sorption sites in holmium silicide on silicon (111). Surface Science. *In Press* (2010).

Chapter 1

Introduction

1.1 Introduction to Surfaces

As a new generation of novel materials is developed, often with nanoscale components, the role of the surface is increasingly important and surface behaviour plays a greater part in determining a material's properties. It is necessary to understand the properties of surfaces for fundamental reasons and so that new materials may be developed and existing ones improved upon.

Breaking of the lattice symmetry by the formation of a surface causes relaxations or reconstructions to occur which in turn modifies the density of states (DOS) of the surface compared to that of the bulk. As such, surfaces may have very different properties to the bulk of a material, and it is these surfaces with which this thesis is concerned. In the context of this thesis, the definition of a surface is the top few atomic layers of a material.

A comprehensive introduction to surface structure is presented by Duke.[1]

1.2 Introduction to Techniques

There are many techniques used to detect surface characteristics. An introduction to the ones used to obtain data for this thesis are provided hereafter.

1.2.1 Low Energy Electron Diffraction

Low energy electron diffraction (LEED) is a technique used to investigate the crystal structure of a surface. This was first employed by Davisson and Germer in 1927 to demonstrate the wave nature of the electron.[2] As electrons with energies between 10 and 400 eV do not penetrate far into a surface, as can be seen in figure 1.1, they are an ideal probe of the surface structure and play an important role in many other surface techniques. However, as these electrons are so sensitive to the surface, the technique requires a well-ordered, clean surface. And so any investigations must be conducted at ultra high vacuum (UHV).

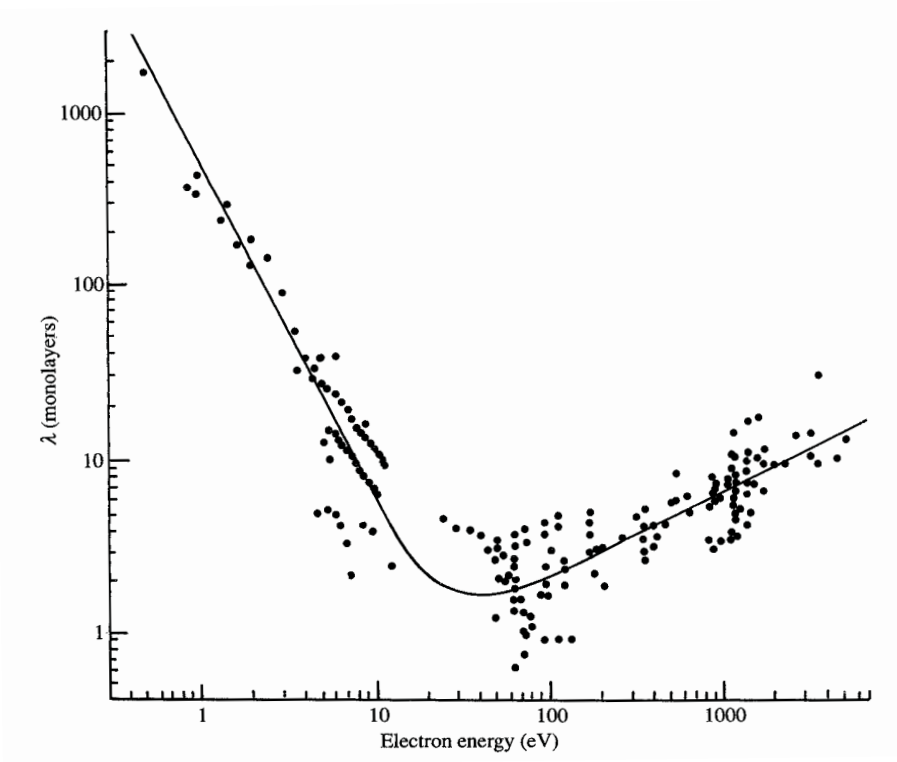

Figure 1.1: Graph of the variation in electron penetration depth for different emergent kinetic energy electrons. Data are taken from a wide variety of materials.[3] It is apparent how surface sensitive low-energy electrons between $\sim$ 10-100 eV are.

In LEED, these low energy electrons are projected at the surface from an electron gun towards the surface. Upon arrival at the surface, the electron beam will be diffracted by the crystal surface and the elastically backscattered beam shows interference patterns which are projected onto a fluorescent screen. The arrangement of the maxima on the screen shows the reciprocal lattice of the surface.

1.2.2 Ultraviolet Photoelectron Spectroscopy

Ultraviolet photoelectron spectroscopy (UPS) is a method of probing the occupied DOS of the near surface of a material.

In this technique, UV photons of energy $h\nu$ are created in a continuous discharge source by applying a high voltage to a gas to cause breakdown. The photons are then targeted onto the sample under investigation. These photons will liberate electrons with sufficient energy, from the sample and into the vacuum where their kinetic energies may be analysed to gain an idea of their energy origin in the DOS using the relationship:

$$E_{kin} = h\nu - E_B - \phi. \tag{1.1}$$

where ϕ is the sample work function. This process is illustrated in figure 1.2.

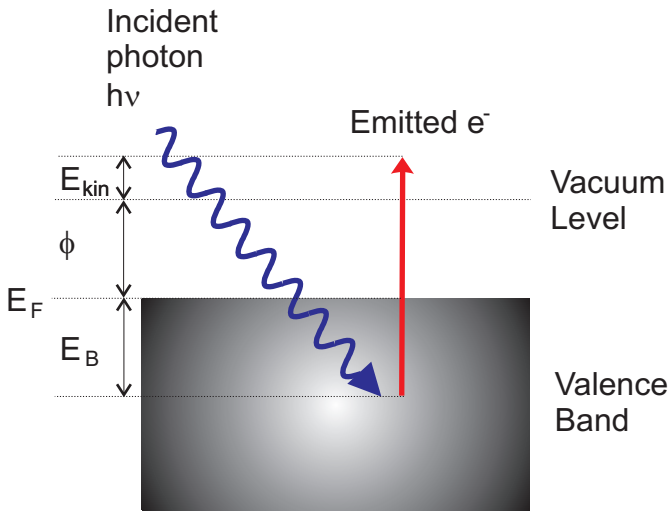

Figure 1.2: Energy diagram of electron emission in photoelectron spectroscopy. Electron energy is plotted vertically.

As the photon may penetrate several nanometres into the surface, some bulk states as well as surface electronic states are probed via this technique. As such, the escape depth of the electron involved is also important.

In our UPS arrangement, we use photons generated by the He I α transition which have a characteristic energy of 21.22 eV ($\lambda = 58.43$ nm). This energy is close to that of the 2^3S metastable He state used in metastable de-excitation spectroscopy (MDS). For this reason, UPS acts as a very useful complementary technique to MDS.

1.2.3 Auger Electron Spectroscopy

Auger emission occurs in an atom after a core electron is removed by either an incident photon or electron of sufficient energy. This results in an electron hole in this core shell. An electron from an outer orbital may then drop down and fill this hole. The energy released by this process is passed onto another, less tightly bound electron which may, if the energy is sufficient, be liberated into the vacuum. These electrons may originate from depths of typically a few angstroms, making this technique extremely surface sensitive.[4] It is also possible for this energy to be released as a photon.

The transition is depicted in figure 1.3.

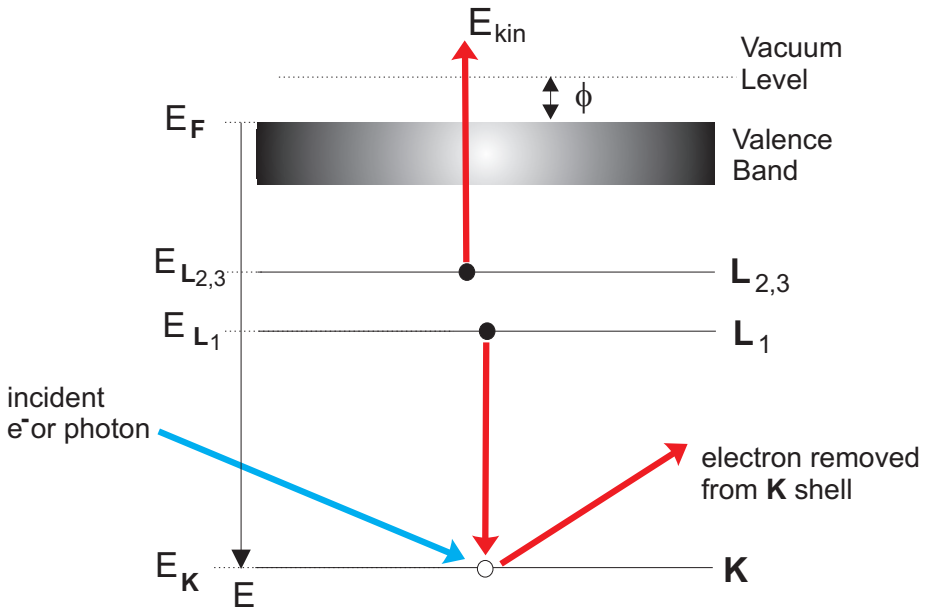

Figure 1.3: Emission of an Auger electron into the vacuum due to an incident electron or photon. Electron energy is plotted vertically.

The energy of the escaping Auger electron is given by the expression:

$$E_{kin} \sim E_K - E_{L1} - E_{L2,3}. \tag{1.2}$$

The particular energies of these Auger electrons are characteristic to specific elements since the binding energies of particular shells are unique to individual elements. Auger electron spectroscopy (AES) utilises this process by bombarding a sample with electrons and scans through an energy spectrum where Auger emission will occur. The energy spectrum of the emitted electrons is plotted, with spikes in the electron intensity revealing if a particular element is present.

1.2.4 Magneto Optic Kerr Effect

When linearly polarised light is incident on a metallic or light absorbing magnetic material, electrons in the material are oscillated parallel to the plane of polarisation. If the material is ferromagnetic, then when a magnetic field is applied across the material, parallel to the plane of incidence, a Lorentz force induces a small component of the electron vibrational motion perpendicular to the primary motion and magnetization direction. This causes re-emitted light to become elliptically polarised. This magnetisation within the sample is known as the longitudinal magneto optic Kerr effect (MOKE) and was first discovered in iron by John Kerr.[5] The effect is illustrated in figure 1.4.

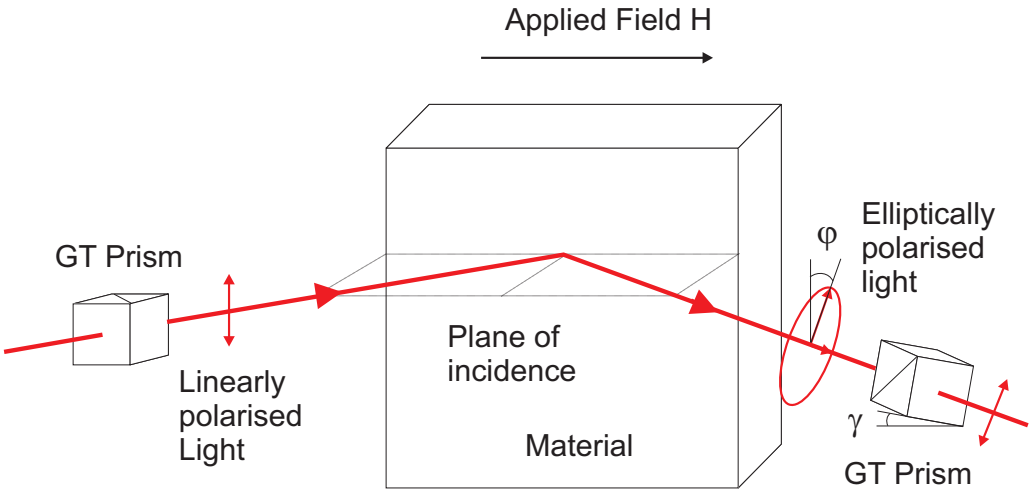

Figure 1.4: Linearly polarised light is elliptically polarised by the magnetised material in MOKE.

The semi-major axis of the ellipse may be slightly rotated from the original linear polarisation (typical rotations are in the order of milliradians). The degree of this rotation is proportional to the magnetisation of the material. Thus, if the magnetisation is altered by the applied field, the semi-major axis of polarisation rotates.

The intensity of the light reaching the photodetector, derived from Snell's Law, is given by:

$$I = I_R \sin^2(\gamma + \varphi), \tag{1.3}$$

where I_R is the intensity of the light reflected by the sample. γ and φ are illustrated in figure 1.4.

As the magnetisation of the sample alters by varying H, the intensity of the light passing through the analysing prism (analyser) will alter. If the analyser is offset by an angle γ,

so that $\gamma > \varphi$ then I has a Taylor expansion approximately linear with φ, and the intensity will be approximately proportional to the material's magnetisation . This principle is used to measure the magnetic hysteresis of a material. However, absolute values of a sample's magnetisation cannot be achieved without some form of calibration.

The MOKE in metals and semiconductors originates from around the top 20 nm of the surface. This is the maximum penetration depth of the light. This effectively makes MOKE a bulk measurement technique.[6,7]

1.2.5 Alternating Gradient Force Magnetometry

Alternating gradient force magnetometry (AGFM) is a method of determining the bulk magnetic characteristics of a material. In a typical AGFM arrangement, a sample is attached to the end a rod which is subjected to an alternating gradient magnetic field which results in a periodic force on the sample, where the sample oscillates at the mechanical resonance frequency. This force is proportional to the magnetic moment of the sample and the magnitude of the gradient of the field, and causes the sample to be deflected. This deflection is detected by piezoelectric elements on the sample rod which output a voltage proportional to the moment once the gradient field is taken into account. A direct current (dc) applied magnetic field from a pair of electromagnets on either side of the sample is slowly looped from no field, to a positive maximum, down to a negative minimum and then returning to the maximum to measure the output at different field strengths. Typical AGFMs are capable of achieving sensitivities down to 1×10^{-8} emu.[8]

1.2.6 Scanning Tunnelling Microscopy

Scanning tunnelling microscopy (STM), originally developed in 1986 by Binnig and Rohrer,[9] is a widely used technique in surface physics as it is one of the few techniques that has the ability to image individual atoms. It is able to probe the electronic properties of these atoms by investigating their *I/V* characteristics.

In this technique, an atomically sharp conducting tip at a potential relative to the sample is moved towards the sample surface using piezoelectric transducers until a tunnelling current occurs. This tunnelling current varies exponentially with the sample-tip separation distance. In a constant current arrangement, a feedback circuit alters the distance between

the sample and the tip to maintain a set current value as the tip is raster-scanned across the surface, so that a height profile of the surface can be deduced.

Alternatively, a constant height mode may be employed such that the current through the tip is measured as the tip is scanned at a fixed height across the surface. This results in a current profile of the surface. The voltage parameters may also be varied to reverse the current direction. This allows both the filled and empty states within the surface to be probed.

1.2.7 Scanning Electron Microscopy

Scanning electron microscopy (SEM), a technique originally pioneered by Knoll in 1935,[10] is a method of surface imaging that uses high-energy electrons ($\sim$0.5 - 30 keV) as the probe. These are produced in a thermionic or field emission source and are then focused onto the surface using a lens column where the beam is raster-scanned across the surface. This electron beam liberates secondary electrons in the top few nanometres of the surface through inelastic scattering, although beam electrons may be elastically reflected (backscattered electrons) and x-rays may also be produced. These secondary electrons pass into a detector with an energy cut-off selected to accept only secondary electrons (generally $<$ 50 eV) and an image of the surface may be compiled as the beam is scanned. The number of secondary electrons detected depends upon both the surface electronic characteristics and the sample-beam interaction angle. The technique is capable of achieving resolutions typically in the order of a few nanometres at a magnification of approximately 1,000,000 times.

1.2.8 Transmission Electron Microscopy

Transmission electron microscopy (TEM) is an imaging technique analogous to optical transmission microscopy. An effectively parallel electron beam is passed through a thin sample, and is then focused onto an imaging device. As electrons pass through the sample, they may be scattered, retarded or pass unheeded, affecting the resulting image. In a High Resolution (HR) mode, a TEM is capable of producing images representative of the atomic arrangement in a material.

1.2.9 Density Functional Theory

Density functional theory (DFT) is a theoretical technique to predict the electronic structure of ground-state, many-body systems. Instead of calculating the wave-functions of individual atoms in a system, DFT uses electron density functionals to simplify the calculation. DFT may be used to calculate the band structure of systems and the DOS. More details of the theory and the `CASTEP` code used for calculations in this thesis can be found in reference 11.

1.2.10 Metastable De-excitation Spectroscopy

When the orbitals of metastable atoms overlap those of a target atom or molecule, de-excitation of the metastable occurs. The process which leads to this de-excitation depends on the work-function of the target. In materials where the work-function is low such that the Fermi energy (E_F) is energetically above the excited state of the metastable helium (He) electron, Auger de-excitation (AD) occurs, where an electron from the surface tunnels into the ground state of the He atom. The exited electron in the metastable atom is simultaneously ejected into the vacuum with the energy released by the initial electron transfer. In higher work-function materials where E_F is lower than the metastable electron, resonance ionisation occurs followed by Auger neutralisation (RI+AN). Here, the metastable electron tunnels into a free state in the surface. This leaves a He^+ ion that continues to approach the surface. Eventually, another electron from the surface tunnels into the ground state to neutralise the ion. The energy released in this transition is used to liberate another electron from the surface, not necessarily of the same initial energy. These ejected electrons from both transition events are captured and their energies analysed. After many of these de-excitation and electron emission events, an electron energy spectrum may be constructed, where the spectrum is related to the DOS of the target material. As the metastable atoms are travelling with near thermal energies and the transition cross-section is high, the de-excitation events occur with the outermost orbitals of the surface. This makes MDS incredibly surface sensitive. This technique is discussed in greater detail in section 1.4.

1.3 Research Overview and Motivation

This thesis is primarily motivated by the resolve to determine the influence of surface atoms in a variety of structures that hold both technological and fundamental interest. These structures are investigated primarily with MDS and spin polarised MDS (SPMDS) where appropriate due to these techniques' unique ability to only probe the outer-most electronic states of the surface. Other techniques are also used to further characterise the properties of structures and reinforce the MDS and SPMDS results.

1.3.1 Instrument Development

To accommodate new additions to the sample chamber and to provide extra capability for future experiments as well as for good vacuum practice, modifications had to be made to the experimental arrangement.

A sample preparation chamber was added so that more flanges were made available for sources etc. A separate preparation chamber would also keep the analysis chamber cleaner. Methods of transfer between the two also had to be developed. A fast-entry lock was added to the system to prevent the need to bake out every time a sample was changed. Various other improvements were also made to the vacuum system.

An *in situ* MOKE experiment was added to the analysis chamber to allow magnetic measurements *in vacuo*. This allowed a comparison between the bulk magnetic properties and the surface magnetic properties measured using SPMDS.

1.3.2 Deconvolution

When MDS is conducted on a surface with a work-function that is above the level of the excited electron in the probing metastable atom, the two-stage de-excitation process of RI+AN takes place. This process results in a self-convoluted MDS spectrum, where features are much more vague than those produced by a single electron process.

Many efforts have been made over the years to deconvolute these spectra, but although the mathematics behind these deconvolution algorithms are sound, the data subjected to these processes were inherently noisy due to the low purity of the metastable beam itself.[12]

The resulting deconvoluted spectra which should reflect the effective surface DOS did not agree well with predicted DOS from theoretical calculations.[13]

As the intensity of our metastable beam is an order of magnitude greater than conventional MDS experiments,[12] the noise level on the spectrum is greatly reduced and so features in the deconvoluted spectrum may be ascertained more clearly with less spurious features arising from noise. This has allowed a fresh attempt at deconvolution for which a deconvolution algorithm has been derived.

Deconvolution has been conducted on spectra of holmium silicide and its hydrogen terminated equivalent and compared to a DFT derived DOS as a test of the procedure.

1.3.3 Rare Earth Silicides

Metal semiconductor interfaces play a crucial role in electronics and hold great potential in upcoming research areas such as spintronics. Rare earth (RE) silicides are one type of metal semiconductor interface with great technological potential due to their unusually low Schottky barrier heights on *n*-type silicon, good epitaxial matching with certain Si surfaces and good electrical conductivity.[14] Work on these systems was initially conducted by Baglin *et al.*[15] A detailed review up to 1995 of RE silicides on Si is provided by Netzer.[16]

For this study, holmium (Ho) has been used as the RE element, which is a typical, trivalent RE.

RE on Si(111)

When 1 monolayer (ML) of trivalent RE is deposited on the (111) surface of Si and annealed to $\sim$800 K, a two-dimensional (2D), hexagonal RE disilicide with 1×1 periodicity is formed as shown in figure 1.5.

The RE atoms locate above the bulk Si substrate but remain below a buckled bi-layer of Si atoms that has a buckling direction reversed to that of the bulk.

Furthermore, when more than 1 ML of RE is deposited onto Si(111) and annealed, a three-dimensional (3D) RE silicide forms where alternating layers of RE and Si exist above the substrate. This structure is again terminated by a buckled Si bi-layer. This

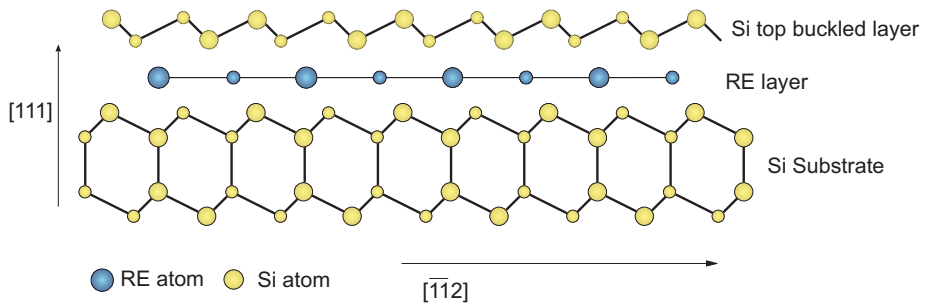

Figure 1.5: Side view of the 2D RE silicide structure which forms upon deposition of 1 ML of trivalent RE and subsequent annealing. Smaller circles represent atoms that are further away from the cross-section plane.

structure differs from that of the 2D by the existence of vacancies in the single Si layers. These exist to relieve stress within the structure and result in a $\sqrt{3} \times \sqrt{3}$ periodicity. The structure is illustrated in figure 1.6.

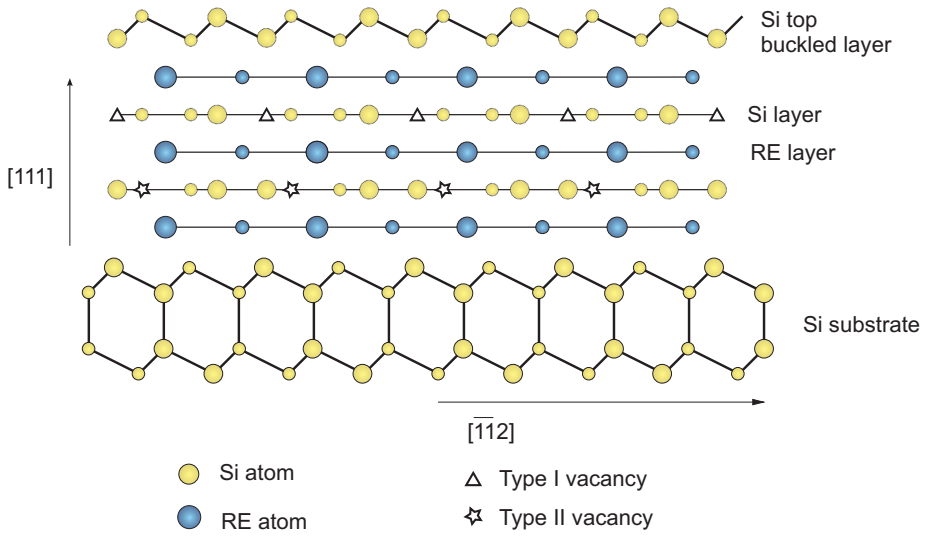

Figure 1.6: Side view of the 3D RE silicide structure containing vacancies within the graphitic Si layers. A B-type buckled surface is shown. Smaller circles represent atoms that are further away from the cross-section plane

The surface electronic states of the 2D and 3D RE silicide have been investigated with MDS and UPS to try and determine whether any difference exists in the surface DOS. Several different RE thicknesses have been investigated. These MDS results have been compared to UPS results which probe deeper into the surface.

It is not known whether these vacancies alter the atomic structure of the top buckled layer between 2D and 3D RE silicides.[17,18] Such differences would affect the surface electronic structure and should therefore be detectable using MDS.

Additionally, the MDS spectra have been deconvoluted so that these results may be directly compared to the DFT calculated DOS. As such, any major differences between the experimental results and those produced by the theoretical structural model may be detected.

The exposure of the surface to atomic hydrogen is expected to drastically alter the surface atomic structure and electronic properties. There has been much evidence suggesting the possible location of adsorbed hydrogen in the unit cell.[19,20] MDS provides us with a new way of investigating this when compared to DFT calculations for various possible sites.

Rare Earth on Si(001)

When RE metals are deposited on Si(001) at an elevated temperature within a certain coverage range (0.1 - 0.5 ML), then RE silicide nanowires (NWs) form across the substrate surface.[21] Self assembled NW such as these hold promise in technological applications such as component interconnects in nanoelectronics;[22] however there is little control over quite where they form.

NW formation occurs due to a lattice mismatch between the RE silicide and the Si(001) substrate which limits the NW growth in the direction of the greatest mismatch, but allows growth where the mismatch is minimal. When the RE is initially deposited on Si(001), Stranski-Krastanov growth occurs whereby nanostructures form on top of a 2D wetting layer. Although little work has been conducted attempting to characterise these regions, they are the precursors to NW growth. When Ho is used as the RE, this wetting layer assumes a 2×4 and a 2×7 reconstruction.[23]

In this study, MDS and STM have been used to investigate this region between the NWs. As NWs only occupy a small fraction of the surface, any MDS spectrum will be dominated by features arising from the states of this wetting layer. MDS probes the valence band of the surface and so provides evidence of the particular bonds between the RE and underlying Si atoms. STM has been conducted to complement the MDS and help identify the atomic features in this layer.

The formation conditions of the 2×4 and 2×7 have been investigated. Suggestions are made as to the identities of atoms giving rise to STM features.

1.3.4 Magnetic Fe Nanoclusters

Evidence suggests that the surface of a ferromagnetic material behaves very differently to the bulk.[24,25] The proportion of a structure that can be classed as surface, increases as the size of the structure decreases. This results in a narrowing of the valence bands, increasing any asymmetry in the spin-split DOS at E_F and making features arising from particular states appear more prominent.

To this end, Fe nanoparticle clusters of mean diameters of approximately 14 nm have been formed using the Small Leicester University Mesoscopic Particle Source (SLUMPS) and deposited onto Si substrates. SPMDS and AGFM measurements have been used to assess the different magnetic contributions. MDS, TEM and SEM have been used to determine details on the clusters' electronic and structural properties. The effects of exposure to oxygen and annealing on the structural, magnetic and electronic properties have also been investigated with a range of techniques.

1.4 Background to MDS

A critical review of literature and theory relevant to the experiment and project is provided. It should be noted that in the literature, MDS appears under a variety of names such as metastable atom electron spectroscopy (MAES), metastable quenching spectroscopy (MQS) and metastable impact electron spectroscopy (MIES). Many publications also report Penning ionisation electron spectroscopy (PIES) and ion neutralisation spectroscopy (INS); these techniques use ions instead of metastable atoms to bombard the surface. The use of ions alters the de-excitation processes that occur.

1.4.1 De-excitation Channels

The first observation of the release of electrons from a target by metastable atoms was made by Webb when a nickel grid was bombarded with mercury in a metastable state.[26] No discussion was given on the process of energy transfer to the grid from the metastable atoms. This was left to Penning who suggested that an ionisation process takes place when a gas state metastable atom, G^*, collides with a target atom or molecule, M, such that:

$$M + G^* \rightarrow M^+ + G + e^-. \tag{1.4}$$

In the paper, the resulting electron is omitted.[27]

This process was further witnessed and studied by Oliphant in 1929.[28] Oliphant used helium atoms excited to the metastable 2^3S_1 state to bombard molybdenum, nickel and magnesium targets. The energy of electrons released from the various surfaces was investigated. This is the first report of metastable de-excitation spectroscopy.

The primary work developing a theoretical description of the energy transfer from the metastable atom to the surface was conducted by Massey.[29] It was claimed that for ions to cause electron emission at a surface, they would initially neutralise to a metastable state by resonance neutralisation and then release an electron by Auger de-excitation.

Cobas and Lamb discussed the release of an electron from a metal surface when bombarded by metastable He^* atoms.[30] An elementary theory for this electron emission process was presented. Cobas and Lamb also showed that the wrong matrix element had been used in Massey's previous work, and so a more accurate interaction distance between the metastable and surface was calculated. All calculations are made for a Mo surface, where the work-function is relatively small; so this theory only stands for the Auger de-excitation process. The process involved in high work-function materials is not discussed.

In 1954 MDS gained a new lease of life when Hagstrum predicted a possible method of de-excitation through a two-stage process of resonance ionisation followed by Auger neutralisation for surfaces where the Fermi edge is below the energy of the metastable state.[31]

With the advent of improved vacuum conditions, the hypotheses proposed by Massey and Hagstrum were reinforced by experimental evidence, where surfaces were characterised with the reactions of incident ions.[32,33] Hagstrum's work on INS and UPS culminated in a review article.[34] This concentrates on the electron transition processes that occur between a surface and incident ion and on using this technique as a viable and insightful spectroscopy. Particular attention is paid to exploring the characteristics of adsorbate surfaces and the sensitivity of this instrument to surface adsorption. A useful discussion is also provided into the uniqueness and limitations of INS.

A review has since been compiled by Harada focusing on developments after Hagstrum's

review.[35] This is specifically on MDS (or MAES as it is referred to) and is more inclined to the study of surfaces rather than the de-excitation processes. Many new samples that MDS has been applied to are reviewed such as organic and liquid surfaces, semiconductors and surface reactions.

Very few noteworthy developments have been implemented to the instrumental arrangement of MDS in its recent history. Notably Yamamoto produced a system capable of metastable electron emission microscopy (MEEM),[36] where the electrons emitted by the surfaces as a result of metastable impact are imaged by an electron lens system. This system proved to be a completely surface sensitive microscope with a lateral resolution of 0.3 μm.

In the conventional MDS experiment, metastable 2^3S He atoms are produced with either cold or hot discharges. Singlet 2^1S He atoms are also produced in the discharge and are quenched with a He discharge lamp through the 2^1S to n^1P to 1^1S transition. Photons are removed with a velocity dependent chopper wheel. This method results in a very low intensity beam due to the inverse square reduction in intensity with distance. The advent of laser cooling by Hänsch and Schawlow in 1975 heralded the possibility to cool atoms using lasers by removing dimensional components of their velocity.[37] This was further developed by Aspect who used this cooling to show that collimation of a metastable He beam was possible.[38] A laser collimated He source was first used in an MDS experiment by Pratt *et al.* in 2005.[39] The beam intensity was increased by more than ten-fold over the source intensity alone.[12] Pratt *et al.* also demonstrated the applications of focusing a 2^3S He beam in MDS by adapting work on magneto-optical traps for the preparation of Bose-Einstein condensates by Dalfovo *et al.*[40]

Several techniques exist for creating metastable atoms. Of these, the dc discharge type is the most suited for producing continuous streams of metastable atoms. These have previously been achieved using a hot needle cathode inside a gas reservoir with an opening into the vacuum chamber,[41] but while dc discharge has remained the typical means of producing triplet metastable helium, more intense, cooled cathode sources have been developed.[42]

Metastable de-excitation spectroscopy has been used to investigate a wide range of organic and inorganic systems providing a valuable insight into their electronic, magnetic and structural properties that other techniques are incapable of investigating alone. Metal

and semiconductor surfaces such as Pd,[43] Fe,[44] Si,[45] GaAs[46] and graphite[47] have been researched at length with the technique to provide information on surface states. MDS is particularly capable of determining changes in surfaces upon exposure to liquids and gases. The Si-O,[13], Si-H[48] and Cu-CO[49] systems to name but a few have been characterised in this way. The technique has also be used to provide information on the orientation of the adsorbed molecule when compared to UPS.[35] Investigations have also been carried out on organic systems such as the alkanes.[50] As only the outer face of the molecule will cause de-excitation, MDS is sensitive to only the outer-most molecular orbitals.

1.4.2 Deconvolution

Hagstrum and Becker provided a theoretical description of the Auger neutralisation process in which they proposed that the electron distribution is a convolution of electron transition probabilities.[51] A model of the convolution is provided along with a critical comparison of possible deconvolution methods. It is suggested that differentiation of the spectrum is more advantageous than deconvolution as it is simpler and yields similar results. In the same year, Mularie and Peria used a deconvolution process to interpret data achieved with Auger electron spectroscopy.[52]

Hagstrum later extended deconvolution methods to INS, where he concluded that matrix elements may be factored into relative transition probability terms, so that the matrix elements would not have to be separately calculated.[34] The deconvolution process involved in INS is more complicated than that necessary for RI+AN.

The deconvolution technique using Hagstrum's step-by-step spline fitting method was demonstrated by Boiziau *et al.* who compared deconvoluted MDS with the calculated DOS for Mo, which showed some agreement in the states present in both.[53] Tagle *et al.* went on to suggest that when using the discrete Fourier transform method of deconvolution developed by Mularie and Peria,[52] care must be taken, as the choice of sign of square root of the Fourier transform is lost.[54]

Sesselmann compared different deconvolution methods and concluded that spline fitting is the most appropriate way to account for noise inherent in the experimentally obtained spectrum.[43] The differences between the spline fit and experimental data are minimised to produce the best possible fit. Adjustable parameters are then obtained for the most effective spline fit, which are used to calculate the effective DOS.

Pasquali used this technique to investigate the electronic structure of GaAs(110) and compared the deconvolution to a tight-binding theory predicted DOS.[46] It is again determined that spline fitting is the most effective method of filtering noise from the experimental spectrum before deconvolution is conducted. It is stated that the reliability of the deconvolution should be tested by ensuring that the reconvolution of the deconvoluted signal gives the original spectrum; and like Hagstrum,[51] he stated that although differentiation and deconvolution are based on different mathematical principles, the first differential and the deconvolution should show features in the same energy positions albeit of different magnitudes.

1.4.3 Polarisation

Stern and Gerlach were the first to demonstrate the existence of spin (intrinsic) angular momentum using a beam of silver atoms in 1922.[55] This principle was developed by Kastler who discussed the the possibility of spin polarising atoms using circularly polarised light tuned to the transition frequency of the particular atom by increasing the proportion of atoms in a particular magnetic sub-level.[56] This was experimentally achieved by Brossel *et al.* using a beam of Na atoms,[57] and was extended to He atoms by Schearer using the illumination of the 2^3S_1 state with 1083 nm radiation to excite it to the 2^3P_2 state.[58] The theory of optical pumping is discussed in detail within this work. Riddle *et al.* developed this technique further by managing to produce a polarisation of the He beam of approximately 50 % as measured with a Stern-Gerlach spin state analyser.[59] The ease of polarisation reversal by rotating a quarter-wave plate was also demonstrated. This source would later be used in some of the first SPMDS studies.

1.4.4 SPMDS

The initial developments towards SPMDS were conducted by Keliher *et al.* in 1975.[60] It was observed that for the AD transition, the spins of electrons emitted through MDS matched those of the incoming metastable atoms. Experiments were conducted on a range of gaseous targets and contaminated surfaces. The RI+AN transition was not considered in this study, but was later investigated by Onellion *et al.* who reasoned that it was possible to probe the surface magnetisation by measuring the difference in electron counts emitted between the two different spin states of the incident metastable atoms without having

to probe the spins of the emitted electrons.[61] The asymmetry in the number of electrons ejected by the different metastable atom spin states was investigated over a range of ejected electron energies for the Ni(110) surface. The surface sensitivity of SPMDS was demonstrated by exposing the Ni to CO in order to show the reduced asymmetry in the DOS with increased surface contamination. Investigations of the surface Curie temperature were also conducted using this approach. Penn and Apell later gave an in depth theoretical description of the technique specifically referring to the RI+AN de-excitation process.[62]

1.5 Chapter Summary

Chapter 2 introduces the de-excitation processes of MDS and SPMDS in more detail and provides a theoretical description of the laser cooling and polarising processes.

Chapter 3 describes the technical details of the experimental arrangement used to perform MDS and SPMDS. A description of the instrument development conducted as a part of this project is also detailed such as the creation of an *in situ* MOKE and a sample preparation chamber with fast-entry lock.

Chapter 4 is concerned with formation of reconstructions on the Ho silicide on Si(001) surface. The evolution of the surface with varying Ho coverages and at different annealing temperatures is discussed. MDS, LEED, UPS and STM are used to support a growth model and identify STM features.

Chapter 5 investigates the electronic structure of Ho silicide on Si(111). A comparison between 2D and 3D surfaces is made, using UPS and MDS. The MDS spectra are deconvoluted and compared to DFT predicted DOS to derive the origins of different features within the spectra.

Chapter 6 is a preliminary study of the electronic, magnetic and structural properties of Fe nanoclusters deposited onto Si substrates. MDS, SPMDS, TEM, SEM and AGFM have been conducted to determine these properties, which are then compared to those of bulk and thin-film Fe. The effects of annealing clusters on Si substrates are also investigated.

Chapter 7 provides concluding remarks on all the systems investigated and any commonality between them. Possible directions of future work on these systems and the MDS instrument are discussed.

Chapter 2

Theory of Metastable De-excitation Spectroscopy

2.1 Metastable Atoms

A metastable state exists in an atom when it is able to remain in an excited state for a relatively long period of time. This is the case for the excited 2^3S_1 state of helium (referred to hereafter as the 2^3S state or triplet state) where one electron occupies the $1s$ ground state and the other occupies the $2s$ excited state, where both electrons have equal spin angular momenta (both spin-up or both spin-down). The ground state for helium is the 1^1S_0 state, where both electrons occupy the $1s$ level and satisfy the Pauli exclusion principle by having opposing spins (one spin-up and one spin-down). Both of these cases are illustrated in figure 2.1. This metastable state in helium exists because a transition to the only lower state, the 1^1S_0 state, is forbidden by selection rules. Any transition would require an integer spin change from +1 to 0 which is forbidden as ΔS must equal zero. Also, the total orbital angular momentum in both these situations remains constant (l = 0), however, selection rules require this quantum number to change by +1 or -1 ($\Delta l = \pm 1$).

Any de-excitation from the 2^3S state would only be possible through a double photon transition by emission of radiation from an oscillating magnetic dipole moment or through an oscillating electric quadrupole moment.[63] The doubly forbidden nature of this transition leads to its extremely long half-life of approximately 8000 - 9000 s.[64,65] This de-excitation transition releases an energy of 19.8196 eV as illustrated in figure 2.2.[64]

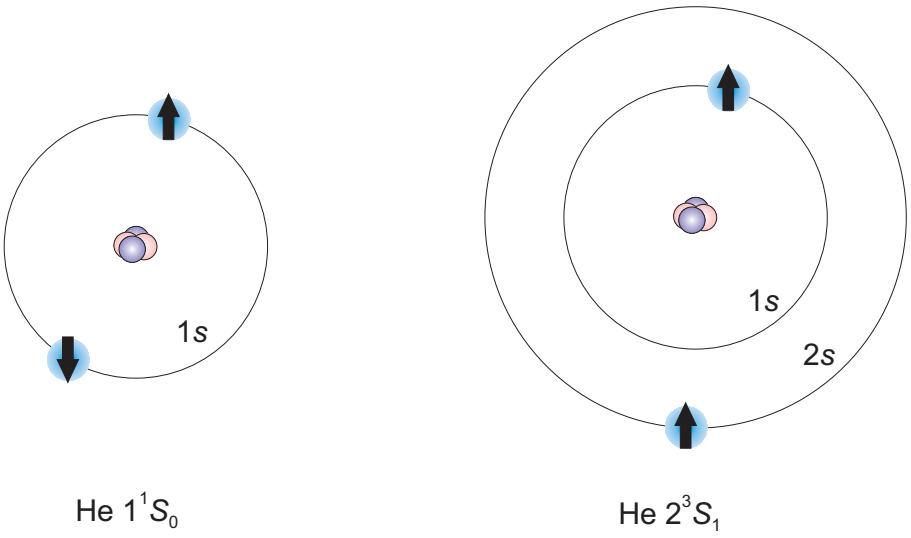

Figure 2.1: The ground state and metastable 2^3S state of He. The energy difference between the two states is 19.82 eV.

2.2 Sources of Metastable Helium

Metastable triplet (2^3S) helium has a number of properties that make it favourable for use in MDS: there is only one possible de-excitation route, so that the energy released by a transition to the lower state is constant; the relatively long half-life ensures that a very large proportion of the helium will reach the target still in its metastable state and the helium metastable states store more energy than any other metastable transition of the Nobel gases. This final property aids spectroscopy by broadening the range of energies accessible in a target. Helium is also unique in that it is possible to alter the spin states of the metastable from $m_s = -1$ to $m_s = +1$ and vice versa via optical pumping tuned to a transition frequency of the He. This is known as polarisation and is described in more detail in section 2.4.4. Such an ability to choose a spin state presents the opportunity for SPMDS which will be discussed later in this chapter.

The triplet state cannot easily be reached through optical pumping due to the same limitations that prevent de-excitation by photon emission. The simplest way of inducing helium from the ground state into this metastable state is by electrical discharge with an energy greater than or equal to the transition energy. The source used in this experimental arrangement is based on a design by Swanson *et al.*[42,66] This design uses a hollow cathode with a much larger surface area than a needle cathode and as such is able to operate at much lower pressures and produces much higher metastable intensities. This source is

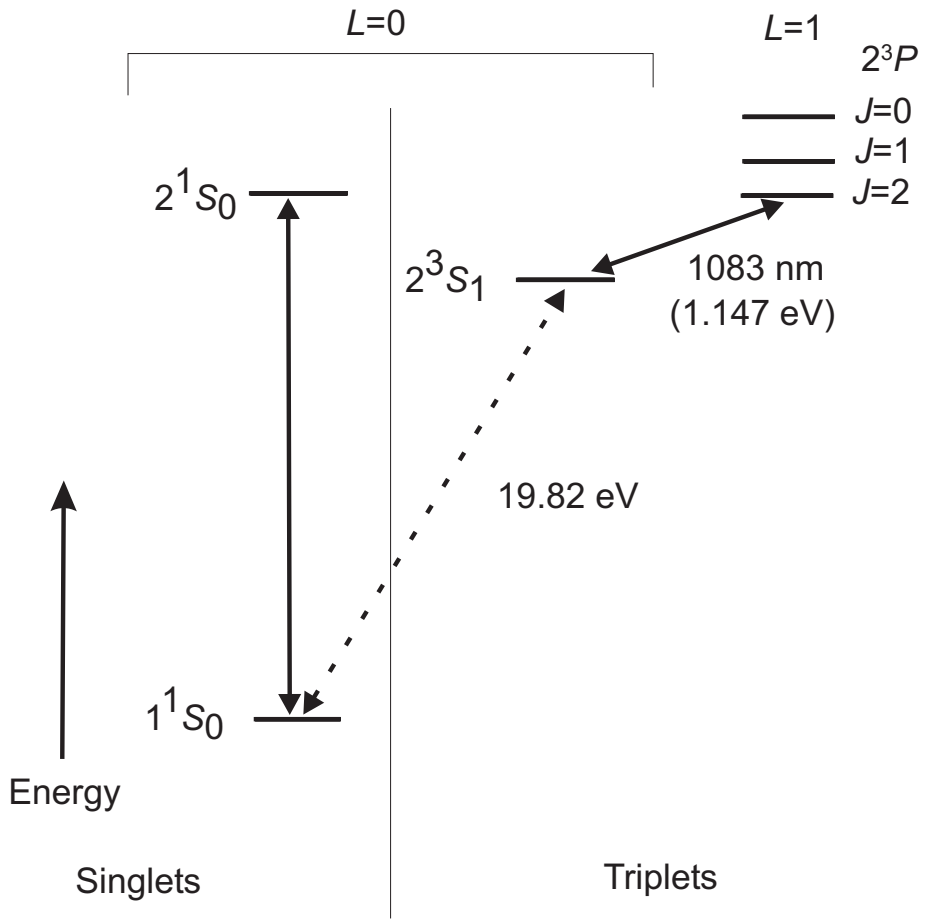

Figure 2.2: Energy level diagram for particular states in singlet and triplet helium. The forbidden transaction between the 2^3S and 1^1S state is marked with a dashed line. Allowed transactions are marked with solid lines.

cooled with liquid nitrogen so as to reduce the initial atomic velocity. Such a source produces a supersonic discharge and has a very narrow velocity distribution, which makes the collimation process more effective.

Another metastable state also exists in helium with the same electron level occupation as the 2^3S, but this time with opposing electron spins. This is the 2^1S singlet state which has a transition energy to the ground state of 20.62 eV and a half-life of approximately 20 ms.[65] This state is also reached through electrical discharge, and hence is produced at the same time as the triplet state with proportions of $2^3S : 2^1S$ of about 10:1. The lifetime of this state is long enough so that the 2^1S will also reach the sample in our experimental arrangement if allowed. This would result in two possible energy values along with the triplet state, when the metastables de-excite, and would thus produce a convoluted electron energy spectrum from the target. In addition, as this state must contain a spin-up and a spin-down electron, it cannot be spin polarised. For these reasons, all reasonable efforts are

made to prevent these singlets reaching the target. This is mainly done through collimation of the triplet state using laser cooling to reduce the proportion of singlets in the beam.

2.3 De-excitation Channels

When a metastable atom collides with a target, a transition to the ground state occurs where the released energy liberates an electron either from the target or from the incident atom itself such that:

$$M + G^* \rightarrow M^+ + G + e^-. \tag{2.1}$$

In fact, there are several different competing processes responsible for this reaction and eventual electron release. Which process occurs depends on the electronic properties of the target material. The probability of reflection of the metastables by the surface through any de-excitation mechanism is very low ($\sim 10^{-6}$ for RI+AN and $\sim 10^{-3}$ for AD).[67,65] The electron yield depends on the process and surface involved, but varies between approximately 0.3 - 0.95 ejected electrons per incident metastable atom.[64]

2.3.1 Penning Ionisation

Perhaps the most basic de-excitation process is Penning ionisation. This occurs between a metastable atom and another ground state target atom or molecule. A collision will ionise the target atom and produce a free electron as in equation 2.1.

As a metastable helium atom approaches a target atom, initially, at large distances, a Van der Waals attraction dominates; and as the atoms get closer, a Coulomb repulsive term becomes increasingly significant, resulting in a Lennard-Jones potential. At a particular distance, the wave-functions of the outer orbital electrons will start to overlap with those of the target atom or molecule. An electron from the target will then tunnel into the $1s$ vacancy thus creating an ion. Any energy released by this transition will transfer to the $2s$ He electron and liberate it from the He atom. The transition rate of this process varies approximately with the exponential of the separation distance.[35]

2.3.2 Auger De-excitation

A form of de-excitation which is very similar to Penning ionisation is Auger de-excitation. This occurs between a metastable atom and a surface, where a broadening of the individual electronic states occurs, creating a band structure and subtly altering the process from Penning ionisation. Auger de-excitation dominates when the Fermi level of the target surface is at a higher energy than the excitation energy of the metastable, i.e. when the surface has a relatively small work-function as shown in figure 2.3 or has a large band gap. For this reason Auger de-excitation is the primary de-excitation mechanism that occurs for insulators where no empty states exist at the energy of the excited He electron and so the electron cannot tunnel into the surface. Spectra resulting from Auger de-excitation tend to have sharp features; however, a limited amount of energy broadening is inherent in the Auger process.[68] The bands in these spectra are directly comparable to those in UPS.

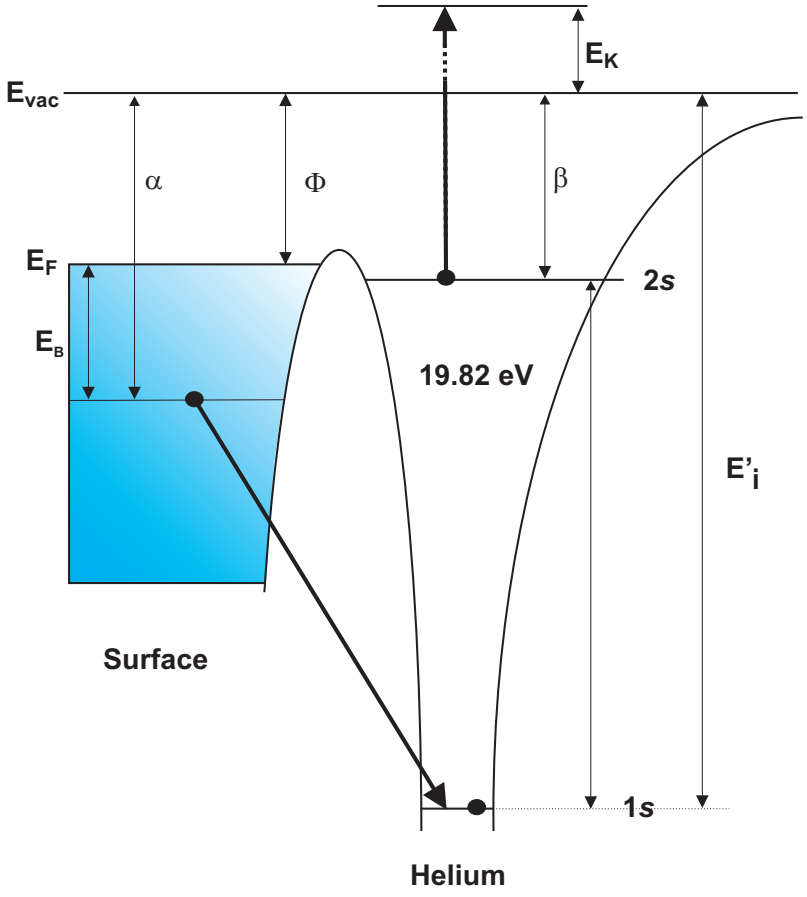

Figure 2.3: Auger De-excitation with 2^3S He. An electron from the surface tunnels into the ground state of the He, causing the $2s$ electron to be liberated.

As with Penning ionisation, a vacancy is available in the He $1s$ level. An electron from the surface then tunnels into this vacancy. The $2s$ electron in the He is now liberated by

the energy released from the tunnelled electron. If this energy is sufficient, the electron will be ejected into the vacuum with a kinetic energy, E_K, where:

$$E_K = E_i' - \alpha - \beta, \tag{2.2}$$

as shown in figure 2.3. E_i' is the effective ionisation potential of the ground state He atom. This is a quasi one-electron process as the initial energy of the emitted electron is constant. The only variable is the energy released by the electron tunnelling from the surface to the $1s$ state. Therefore, from E_K, the initial binding energy, E_B of the tunnelling electron can be calculated as:

$$\begin{aligned} \alpha &= E_B + \phi, & (2.3)\\ E_i' - \beta &\approx 19.82\ eV, & (2.4)\\ E_i' &= E_K + \beta + \alpha, & (2.5)\\ E_B &\approx 19.82 - \phi - E_K; & (2.6) \end{aligned}$$

where ϕ is the work-function of the surface. This is the dominant de-excitation in most insulators and also in rare-earth metals, where the work-functions are unusually small. The probability of Auger de-excitation is highest in the region of 3-5 Å from the surface (the 2^3S atomic radius is estimated at 2.9 Å).[43,31]

2.3.3 Resonance Ionisation and Auger Neutralisation

When the Fermi level of a surface is energetically below the $2s$ level of the He metastable, then resonance ionisation followed by Auger neutralisation (RI+AN) will be the dominant channel of de-excitation. This two-part process is illustrated in figure 2.4.

As there are only empty states in the surface at the energy of the $2s$ electron, the electron may tunnel across into the surface. This occurs at distances of around 9 Å and leaves a positive He^+ ion which continues to approach the surface.[69] This part of the process is termed resonance ionisation.

At some point (typically at a distance of approximately 5 Å),[43] an electron from the surface will tunnel into the $1s$ vacancy, and in doing so will form a ground state helium atom. The energy released by this process, $E_i' - \alpha$, will transfer to another electron in the solid such that no energy is lost as radiation. If this energy is sufficient, the electron will be ejected from the surface with energy E_K, where E_K is given by equation 2.2 as

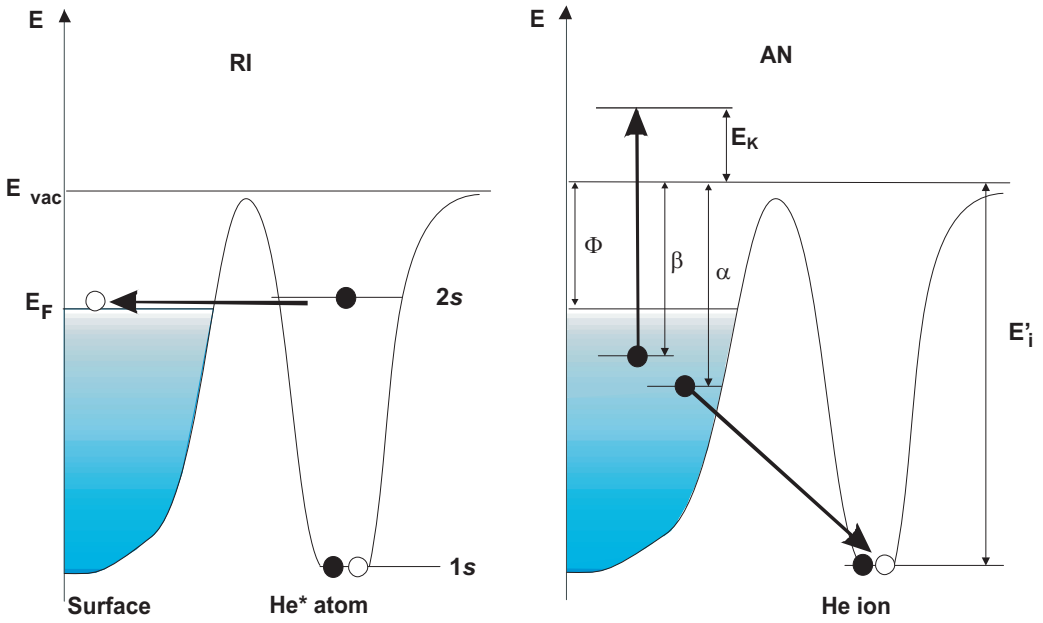

Figure 2.4: Resonance ionisation followed by Auger neutralisation in the case of 2^3S He. Initially an electron tunnels from the $2s$ state of the He into the surface. An electron from the surface then tunnels into the $1s$ state, simultaneously liberating a surface electron in the process.

before. E_i' will, however, vary due to the image potential. This process is termed Auger neutralisation and the electrons involved in this transition can come from any energy in the filled band of the surface. The two electrons involved in the transition are, however, likely to arise from the same physical locality, and the probability of an ejected electron arising from a particular location varies as an exponential with distance from the de-excitation electron.[70] The maximum possible kinetic energy available to the liberated electron will arise when both the electrons involved in the Auger neutralisation process are initially at the Fermi energy, i.e. when $\alpha = \beta = \phi$. If this is the case then:

$$E_{K,max} = E_i' - 2\phi. \tag{2.7}$$

The minimum kinetic energy of the escaping electron occurs when both the electrons arise from the highest possible binding energy accessible in the valence band.

If, as mentioned previously, there is no unoccupied state in the surface for the excited electron to tunnel into, then Auger de-excitation will occur.[31]

As neither of the Auger electrons originate from a set energy, two variables exist such that the initial energy level of the emitted electron cannot be directly calculated from its kinetic energy. This leads to a self-convoluted energy spectrum, where any features due to the energy levels of the surface will be broadened in a self-convolution given by the

self-folded integral:

$$F(\varepsilon) \propto \int_{-\varepsilon}^{\varepsilon} |H_{fi}|^2 \, N(\varepsilon - \Delta\varepsilon) \, N(\varepsilon + \Delta\varepsilon) \, d(\Delta\varepsilon), \tag{2.8}$$

where $F(\varepsilon)$ is the transition probability (related to the intensity of the spectrum), H_{fi} is the Auger matrix element and $N(\varepsilon)$ is the local density of states.

It should be noted that Dunning *et al.* proposed that both de-excitation processes may occur on a surface which would normally be assumed to de-excite by RI+AN, where some metastables get close enough to the surface to undergo direct Auger de-excitation.[71] It is suggested that the likelihood of resonance ionisation increases exponentially with decreasing surface-metastable distance to a certain point, where saturation occurs, and thus allows some metastables to encroach to the 3 - 4 Å needed for Auger de-excitation.

2.3.4 Image Potential

From $E_{K,max}$ it is possible to estimate the surface work-function if E_i' is known. However, in the case of Auger neutralisation, E_i' is actually a function of separation from the surface due to the image force. In the case of He^+, E_i' has a gas phase value of 24.6 eV. This is reduced by the interaction with the solid surface through the image force by the relationship:

$$\Delta E_i = \frac{-3.6}{(R-d)/\text{Å}} \, eV, \tag{2.9}$$

where ΔE_i is the change in ionisation potential from the gas phase, *R* is the distance between the ion centre and the edge of the metal surface and *d* is a corrective distance to account for the image force (estimated at 0.6 Å).[72]

As the energy of the liberated electron is dependent on the energy of the 1*s* level in the He^+ which varies with the image force, it will have a greater energy if Auger neutralisation occurs at a greater distance from the surface.[73]

2.3.5 Other De-excitation Channels

In the case of an ion approaching the surface of a solid, if E_F is higher than the now empty excited state of the ion, then resonance neutralisation may occur. This process is illustrated

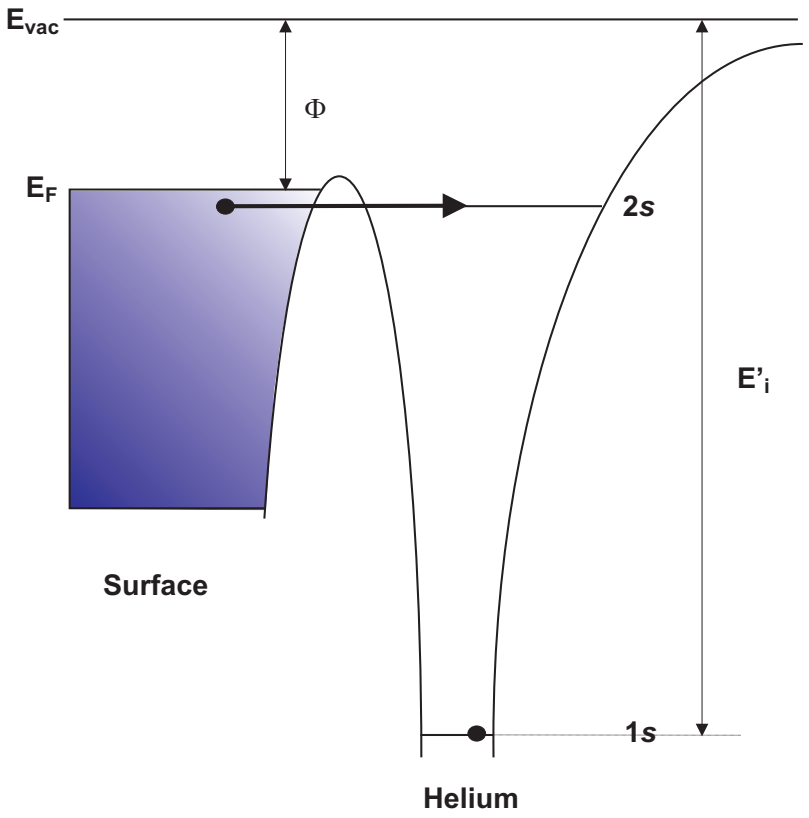

Figure 2.5: Resonance neutralisation in the case of 2^3S He. An electron tunnels from the surface into the $2s$ state in the He^+ ion.

in figure 2.5. Auger neutralisation is also a possible competing process, for such an ion, but is less likely due to the low surface work-function.

This leaves a metastable atom which may then undergo Auger de-excitation. Such a process is unlikely to play an important role in most systems as the lifetime of the initial state is 10^6 longer than either of the Auger processes.

2.4 Collimating, Focusing and Polarising

To maximise the signal of the spectrum, we require the yield of metastable helium reaching the target to be as high as possible. Under normal conditions, the beam's intensity reduces by a factor of $1/r^2$ travelling along the beam line. This reduction is prevented by collimating the beam using optical pumping. Such a collimation has recently been achieved within the Surface Physics Group at York by Pratt *et al.*[39] Here, atom optics have been used to increase the metastable helium intensity by collimating the helium beam and

then focusing it by exploiting laser cooling and the spontaneous force. This has also lead to an improved purity of 2^3S He at the sample.

2.4.1 Optical Pumping

2^3S He can be excited into the 2^3P_2 state by illuminating it with light of the resonant frequency to the transition (in this case, with a wavelength of approximately 1083 nm). This transition has an associated energy of 1.147 eV (as shown in figure 2.2).

This 2^3P_2 state has a very short half-life of 98.8 ns and so quickly decays back into the 2^3S state re-radiating this energy in a random direction. If a helium atom undergoes several of these events with the incident photons originating from the same direction, then the atom will experience a net momentum away from the direction of illumination. This illumination is applied with a laser and the resulting force is referred to as the spontaneous force. Each photon will deliver a unit of momentum:

$$\Delta p = \hbar k = \frac{h}{\lambda}, \tag{2.10}$$

$$\Delta p = m\Delta v, \tag{2.11}$$

which leads to a recoil velocity,

$$\Delta v = \frac{h}{m\lambda}. \tag{2.12}$$

Therefore, every absorption event imparts a velocity of 9.2 cms^{-1} on the helium atom. When an atom has a velocity component along the wave vector of the laser, it is subject to a Doppler shift, altering the wavelength of the transition and hence the force that is exerted by the laser. This force varies as a Lorentzian with the velocity of the atom, and so will only have a significant effect on atoms within a certain velocity range and will vary within that range. By detuning the laser frequency, this velocity range can be altered, so that atoms with a velocity other than zero feel the maximum force. When two counter-propagating laser beams are used transverse to the beam-line, any deviating atoms will feel a force towards the beam-line. By using two laser beams at right angles to each other and perpendicular to the beam-line, the He beam may be controlled in two dimensions. To increase the number of transitions taking place, four mirrors are located along the beam-line, so that the 2 laser beams are reflected multiple times. These mirrors bend so that the lasers cross the beam line with a larger and larger angle until they are practically perpendicular to the mirrors. This interaction angle alters with the changing Doppler shift

of the atoms and results in a well collimated beam. An illustration of such an arrangement for two dimensions is given in figure 2.6.

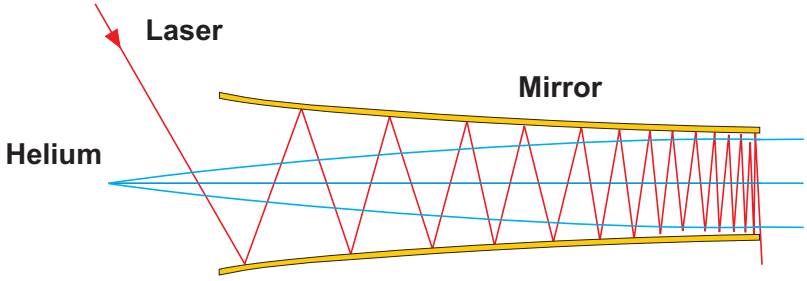

Figure 2.6: Helium collimation via optical pumping in two dimensions. The angle at which the laser beam interacts with the He 2^3S beam changes with the curve of the mirrors.

2.4.2 Selection of the 2^3P_2 Level

We use the transition from the 2^3S to the 2^3P_2 level to aid optical pumping. As polarised light is used to pump the atoms, for σ_+ polarised light, the magnetic sub-level of an atom must alter by $\Delta m_s = +1$ and vice versa. This means that for an atom in the 2^3S state with $m_s = +1$, a transition is only possible to a higher state with an $m_s = +2$ sub-level. This is only available in the 2^3P state where $J = 2$, i.e. the 2^3P_2 state which has sub-levels from -2 to +2. This is illustrated in figure 2.7. De-excitations from this level must follow the rule $\Delta m_s = 0, \pm 1$. Therefore, the atom must de-excite back into the $m_s = +1$ sub-level of the 2^3S state forming a closed transition cycle as no other de-excitation routes are available. If a transition to either the 2^3P_1 or 2^3P_0 state was selected, the efficiency of optical pumping would be reduced dramatically as excitation to some sub-levels would not be possible.

2.4.3 Focusing

To achieve a maximum intensity of helium bombarding the sample, the beam may be focused after the collimation stage. This is performed using the spontaneous force in a device called a magneto optical lens. Laser light of the transition frequency is polarised and used to illuminate the beam on its transverse axes so that light propagating in opposite directions has opposite polarisations, as shown in figure 2.8. A magnetic quadrupole field is created transverse to the helium beam-line, so that at the centre of the beam, the field is zero. The magnetic field causes the degeneracy of the magnetic sub-levels to lift, but this

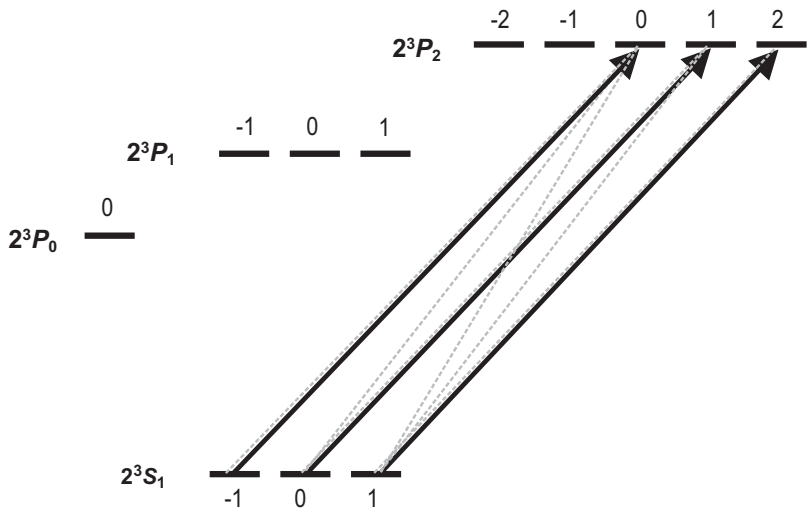

Figure 2.7: Helium excitation (black lines) / de-excitation (grey lines) transitions between different sub-levels. Only transitions to the 2^3P_2 sub-levels are shown for σ_+ polarised light.

field and hence the energies of the sub-levels is position dependent.

The helium in the beam will experience a force that depends on its position from the centre of the beam-line and acts towards the centre of the beam-line. Transitions are induced by the polarised laser light so that atoms away from the beam-line axis become more resonant to one beam than the other due to the shifted energies of the sub-levels. The atom will therefore experience a greater force from one polarisation beam than the other, so will be directed towards the central axis where the field and Zeeman shift are zero.

Although the ability to perform focusing is available on our experimental system, it has not been used when conducting the set of experiments reported in this thesis, as even small thermal drifts in laser frequency result in large changes in the intensity of metastable beam and hence the electron intensity in the MDS spectrum, thus making any quantitive measurements troublesome.

2.4.4 Polarisation

In the helium beam, atoms with both spin-up and both spin-down electron configurations will be present in equal numbers. To perform SPMDS, the helium beam must be polarised so that all the helium exists in the same quantum state, i.e. all spin up ($S = +1$) or all spin down ($S = -1$). This is done by optically pumping the helium with polarised light (σ_+ for the $S = 1$ state or σ_- for the $S = -1$ state) tuned to the 2^3S - 2^3P_2 transition frequency

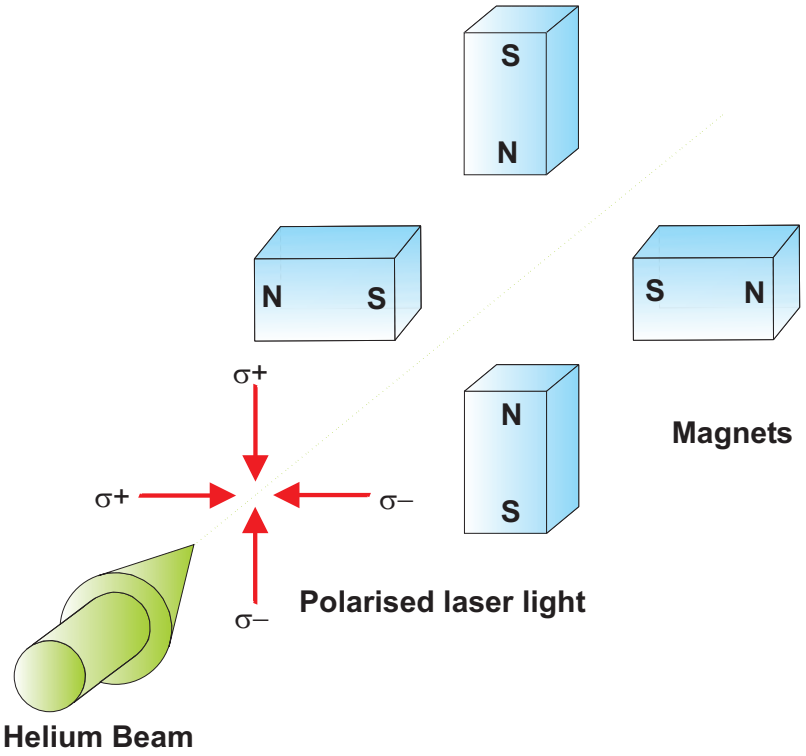

Figure 2.8: Focusing the He 2^3S beam using a magneto optical lens. 2^3S atoms experience a force towards the centre of the lens.

to raise or lower all the helium into the same spin state. Depending on the initial state of the helium, this might take several absorption emission cycles. A weak magnetic field is then applied transverse to the beam-line to provide an axis of alignment for the spins.

2.4.5 SPMDS

In some materials, the spin resolved density of states is asymmetric, i.e. the number of electrons in each spin state is not equal at a particular energy. This leads to majority and minority spin states at different energies. Such an asymmetry exists in magnetised ferromagnetic materials. As these materials tend to be metallic, in most cases they de-excite through the two-stage process of RI+AN.

Initially, in the resonance ionisation process, an electron tunnels into the surface above the Fermi energy, then in Auger neutralisation, an electron tunnels from the surface into the 1s state of the helium and an electron is ejected from the surface. This Auger electron that transfers from the surface to the He^+ ion must have an opposite spin to the electron already residing in the 1s level to abide by the Pauli exclusion principle, and so must originate from a spin state in the surface opposite to that of the helium. This process is

dependent on that spin state existing in the surface. It is illustrated in figure 2.9.

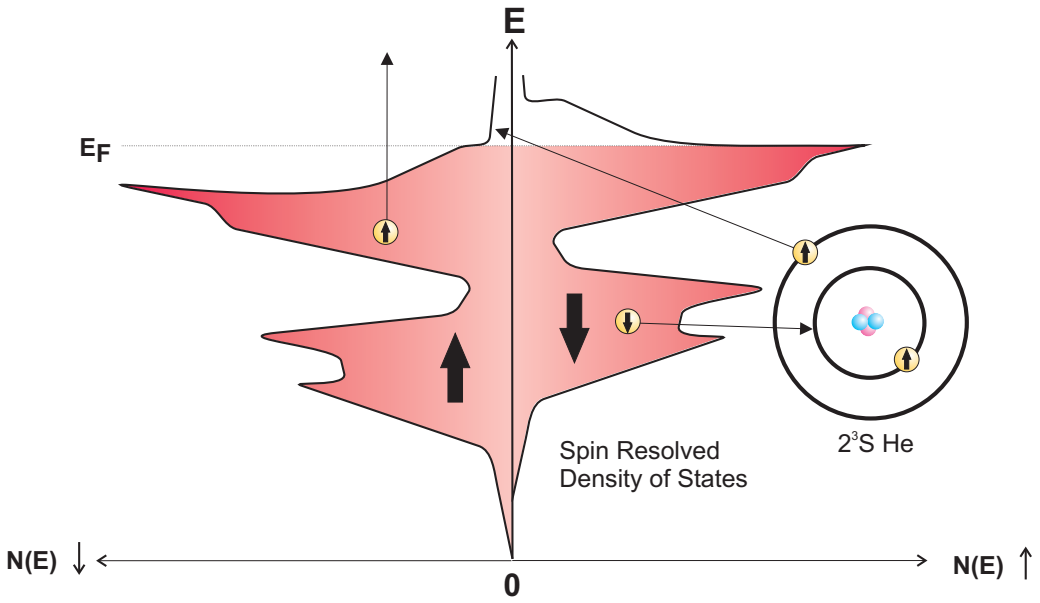

Figure 2.9: Resonance ionisation and Auger neutralisation for a magnetised surface. The ejected electron is shown as originating from the opposing spin state to the neutralising electron.

The emitted electron may arise from either of the two spin states present, however, it has previously been observed that the neutralising electron and emitted electron tend to have anti-parallel spins.[71] Two mechanisms have been proposed to explain this: either Auger de-excitation still plays a role even when RI+AN would be expected, as mentioned in section 1.2.3; or a two-hole singlet state in the surface is preferred. If the latter is the case, it is suggested that this couplet effect is most pronounced when both electron originate close to E_F and is consistent with the Pauli exclusion principle.[74,75] The probability of either electron coming from a particular energy will depend on the spin resolved density of states for that particular spin state. For this reason, subjecting a surface to one particular metastable spin state does not only probe one spin state of the DOS; a contribution will arise from the other spin state. More recent theoretical work suggests a combination of both these processes along with secondary electrons is responsible for the polarisation of the emitted electron.[69] Using the Cu(001) surface as an example, it was shown that only 2% of the ejected electrons are thought to be due to Auger de-excitation. However AD is the major contributor to the increasing polarisation in the high-energy range.

Let us consider the case where the neutralising electron and emitted electron both originate from the same spin state: The spectrum that would result is now a self-convolution of the DOS for just this spin state. In the case where they originate from opposite spin

states, the resulting spectrum would be a convolution between both spin states in the DOS and so would not provide us with any information on the asymmetry in the spin resolved DOS. In practice we will have a convolution of both these cases, and so some information will be retained on whether or not an asymmetry exists, but without an estimate of the proportion of electrons involved in Auger neutralisation coming from the same and opposite spin states, which depends on the surface under investigation and the energy, the asymmetry parameter we derive will be less than that for the actual spin resolved DOS. It has also been suggested that the He^+ ion can lead to a local spin perturbation in the electronic structure of the surface that would essentially magnetise the local surface, thus further influencing the measure of surface asymmetry.[76]

Some magnetic materials are insulating and as such, the dominant interaction with the metastable is Auger de-excitation as shown in figure 2.10.

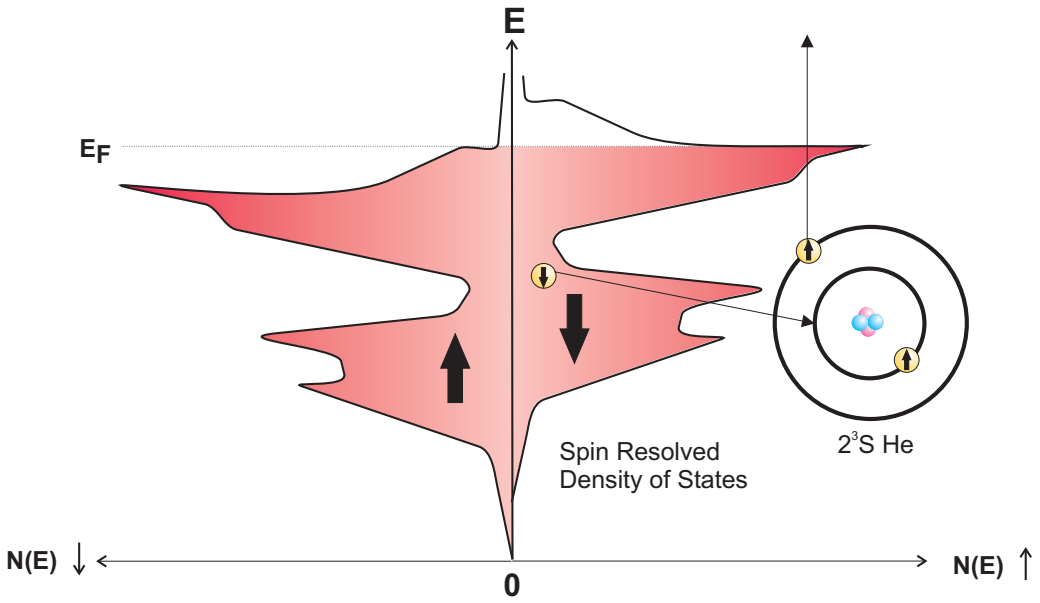

Figure 2.10: Auger de-excitation for a magnetised surface. The electron that tunnels from the surface into the $1s$ state must have opposing spin to the emitted electron.

By bombarding such a surface with metastable atoms of one spin state alone, as long as their axis of orientation is aligned to the magnetisation of the sample, then just that state within the sample will be probed. Therefore, if the majority spin state of the surface at a particular energy is opposite to that of the He, there should be a greater electron yield than if the spins were the same. This can be compared to the data collected using the other spin state and so an impression of the asymmetry of the spins can be obtained for different energies. This is more representative of the spin asymmetry in the DOS than for the two-stage process, since the emitted electron arises from the metastable itself, for one

particular polarisation of the He, only one particular spin of electron should be released. However, in reality this is not the case due to the production of secondary electrons from the surface.[75] This will lead to a slight deviation between the measured asymmetry and the actual asymmetry in the spin resolved DOS.

For both de-excitation processes, the Asymmetry parameter, A, is a measure of the proportion of spin-down states to spin-up states and is given by:

$$A = \frac{1}{|P_z|}\frac{N(E)\uparrow - N(E)\downarrow}{N(E)\uparrow + N(E)\downarrow}, \tag{2.13}$$

where P_z is the polarisation and is given by:

$$P_{z\pm} = \frac{R\uparrow \mp R\downarrow}{R\uparrow + R_0 + R\downarrow}. \tag{2.14}$$

$N(E)\uparrow$ and $N(E)\downarrow$ are the numbers of electrons collected in the analyser when using the spin-up polarisation and spin-down polarisation helium beam respectively. $R\uparrow$ and $R\downarrow$ are the helium atom count rates for the spin up polarisation and spin down polarisation respectively. R_0 is the count rate for unpolarised He atoms (2^1S).

Chapter 3

Method

3.1 Introduction

This chapter sets out to describe the experimental equipment used in MDS much of which is unique to our particular laboratory. Normal operating conditions are also outlined.

Details of modifications that have been made to the system as a part of this project are provided such as the design and construction of an *in situ* MOKE for which preliminary results are provided. The addition of a Stern Gerlach analyser is detailed for the purpose of characterising the polarisation of the He beam. The results of this characterisation are presented. A sample preparation chamber has also been added to the experimental arrangement as part of this work which is further detailed within the chapter. A method of deconvoluting the spectra achieved when the de-excitation process is RI+AN is outlined, with the purpose of retrieving the effective DOS.

3.2 Metastable Production and Beam Operation

A schematic of the beam-line used in this experiment is presented in figure 3.1. A description of the components are given in the following sections.

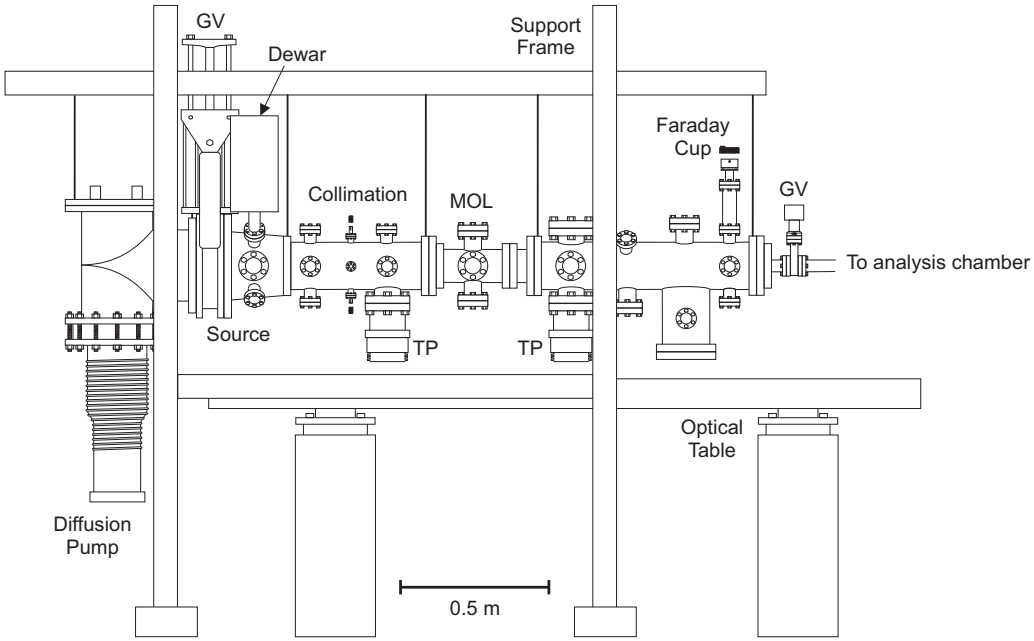

Figure 3.1: Schematic diagram of the beam-line adapted from reference 77. A detailed description of the components is provided in the text.

3.2.1 Metastable He 2^3S Source

He of 99.999 % purity is injected from a regulated 50 L BOC cylinder through a stainless steel gas line to a leak-valve which feeds into the metastable He 2^3S source illustrated in figure 3.2.

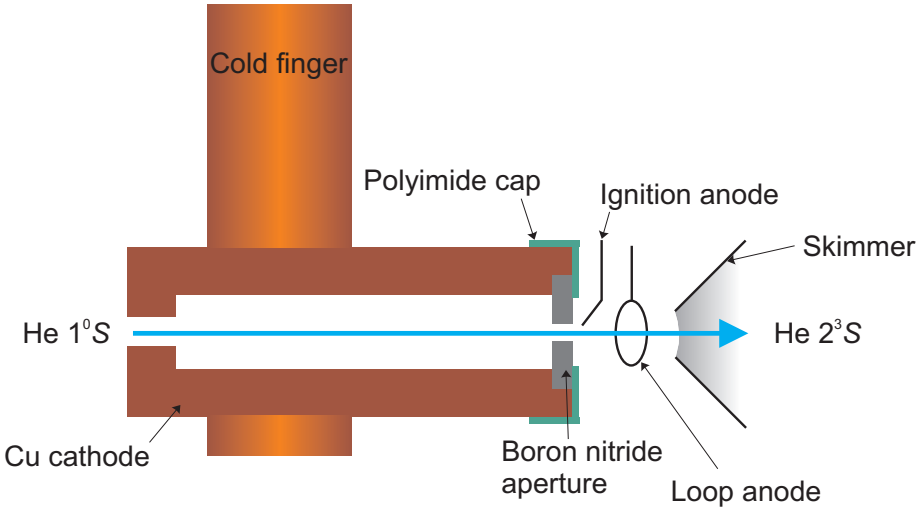

Figure 3.2: The cooled hollow Cu cathode He 2^3S source. Ground state He is injected into the source at the rear through a leak-valve.

The source, which resides inside the beam-line, consists of a hollow Cu tube cooled by an attached Cu rod which is connected to an LN_2 dewar on the outside of the beam-line.

At the front of the tube is a 0.3 mm circular aperture constructed of Boron nitride which has a long lifetime when suffering from electron bombardment as well as a high thermal conductivity. A polyimide cap is placed on the end of the cathode to provide insulation from the anodes. The first anode is used to ignite the initial discharge between it and the Cu cathode with an applied potential of 5.0 kV, once the discharge is operating, this is current limited to 3 mA. The second, the ring anode, maintains a stable discharge once the discharge has been initiated. This is set to a potential of 1.2 kV. In front of the anodes is a skimmer, used to reduce the profile of the discharge. The skimmer has a potential of -500 V applied to it.

Initially a pressure of approximately 65 mbar is required for the discharge to occur. However, as soon as this happens, the driving pressure may be reduced with the leak-valve to 11 mbar as measured on a capacitance manometer.

The relationship between driving pressure and metastable flux follows a log-normal distribution with the peak flux occurring at a pressure of approximately 11 mbar. At too low a pressure, the discharge cannot sustain itself for long periods. At high pressures, collisions occur between the metastables which result in de-excitation before they reach the Faraday cup, resulting in a low flux.

When the source discharge is initiated, the pressure inside it is quite high. This results in more photons being produced in the discharge. For this reason, once potentials have been applied and breakdown has occurred, the source is left for at least 10 mins so that a pressure equilibrium can be maintained before experiments are conducted to ensure beam stability. A detailed characterisation of this source can be found in reference 77.

As the gas load in the chamber is quite high, and a low pressure is needed to enable the source to operate efficiently and to ensure the maximum amount of 2^3S He can reach the sample chamber without being de-excited by collisions with other gas atoms or molecules, a high pumping capacity is required. A Varian NRC diffusion pump with a nominal pumping capacity of 4000 ls^{-1} is mounted behind the source which helps maintain a pressure in the beam-line of $\sim 10^{-5}$ mbar when the He is admitted to the chamber. When the He leak-valve is closed, the diffusion pump is closed off from the beam-line with a pneumatic gate-valve to minimise the amount of diffusion oil that enters the beam-line. The diffusion pump is backed by a single-stage Edwards M40 rotary pump. An Edwards EXT250 and a modified Leybold Turbovac 360CSV turbomolecular pump of nominal pumping capac-

ities of 240 ls^{-1} and 345 ls^{-1} respectively are used to pump the beam-line. When there is no He throughput, a pressure of approximately 2×10^{-8} mbar is maintained. Both turbomolecular pumps are backed by a single, two-stage, Edwards M40 rotary pump.

3.2.2 Laser Collimation

To collimate the metastable beam in our experimental arrangement, we employ laser cooling by targeting two perpendicular laser beams onto perpendicular mirrors within the beam-line as previously outlined in section 2.4.1 and figure 2.6.

A solid-state Topica Photonics DL100 laser diode is used to generate the initial laser beam as it has been designed specifically for laser cooling applications, is stable, is suited to the wavelength we require (1083 nm), is tunable over a 7 nm range, has a very narrow linewidth due to its external cavity diode ($\sim$ 1 MHz) and has a reasonable power output (40 mW maximum). The laser beam is initially passed through an optical isolator to prevent back-reflection into the laser cavity. As the diode output is elliptical, this must be transformed to a circular beam to prevent losses when interacting with other optical components. This is done with an anamorphic prism pair which outputs a vertically polarised beam of approximately 3 mm diameter.

The power output of this diode is not sufficient to fulfil our requirements for both collimation and spin polarisation. Because of this, the beam generated by the diode is fed into a fibre-optic connected to a IPG Laser GmbH YAM-1-1083 Yb doped fibre amplifier. This provides an output of up to approximately 0.4 W at 1083 nm which is sufficient for our needs.

From the amplifier, the beam passes along the optical table through another optical isolator, and various lenses in place to combat divergence. The beam is then split using an anti-reflection (AR) coated beam-splitter to provide one beam for the polarisation section and one for the collimation. The collimation beam is further split to provide two separate beams which are targeted using adjustable mirrors onto AR-coated windows and onto the collimation mirrors within the beam-line. These mirrors measure 300 mm in length and are made of float glass with a Cr adhesion layer and an Au reflective layer to achieve high reflectivity ($>$95%).[77] The curvature of the mirrors has been set so that the reflection angle is reduced after every single reflection event in a way to ensure the optimum collimation.

The laser wavelength is then tuned using the laser controller to provide the maximum collimation. The metastable flux is measured with a Faraday cup. The metastable He flows through a hollow cylinder held at 32 V mounted in front of a 20 mm diameter stainless steel disc grounded through a picoammeter. As metastables hit the disc, electrons are liberated from it by de-excitation which produces a current proportional to the metastable intensity. The hollow cylinder acts to draw away the ejected electrons.

Efforts are made to minimise the presence of photons and singlet metastable He atoms that are produced alongside triplet state within the source. Collimation is only resonant for the triplet state, so that the singlet He continues to diverge to such an extent that its presence in the beam at the sample is negligible. The photons are blocked by inserting a small disc of diameter 5 mm in the centre of the beam. This does however reduce the intensity of the triplet state too.

3.2.3 Polarisation

The linearly polarised laser beam intended for He polarisation is initially passed through a quarter-wave plate to circularly polarise the beam. This may be rotated by 90° to reverse the polarisation. The beam is then passed through two lenses to expand the spot size to greater than the diameter of the metastable beam, to ensure total interaction with the entire beam. The circularly polarised laser beam is then directed into the beam-line through AR coated windows, perpendicular to the He flow direction. From here, the laser beam passes out of a window on the other side and onto another mirror which reflects it back through the beam-line in the opposite direction to ensure the maximum possible interaction with the He. Helmholtz coils are placed around the windows on either side of the beam-line to provide an axis of magnetisation. A current of 1 A is used which produces a fairly uniform field of 0.8 Oe perpendicular to the He flow.

3.2.4 Interlock System

An electronic interlock system has been created to protect the beam-line from various kinds of malfunction. Flow meters have been fitted to cooling pipes so that either the turbomolecular or diffusion pumps will power down in the event of a reduced flow of the cooling water. When any of the pumps shut down for whatever reason, two pneumatic

gate-valves between the analysis chamber, beam-line and diffusion pump close to protect the other components of the system. These pumps will also shut down if the backing pressure rises too high. An automatic venting feature admits air into the system when the Edwards turbomolecular pump spins down to half of its normal operating speed. Faults within the turbomolecular pumps themselves will ensure that both turbomolecular pumps will shut down if a fault is detected in either of them and that the backing lines will shut automatically. Over-rides on the interlock allow operation of the system under non-standard operating conditions.

3.3 Analysis Chamber

The analysis chamber is located at the end of the beam-line so that the metastable atoms impinge upon a sample at the centre of the chamber. A 5 mm diameter, circular aperture is placed inside the gate-valve between the beam-line and the analysis chamber to limit the pressure increase when the gate-valve is opened. The layout of the chamber is illustrated in figure 3.3.

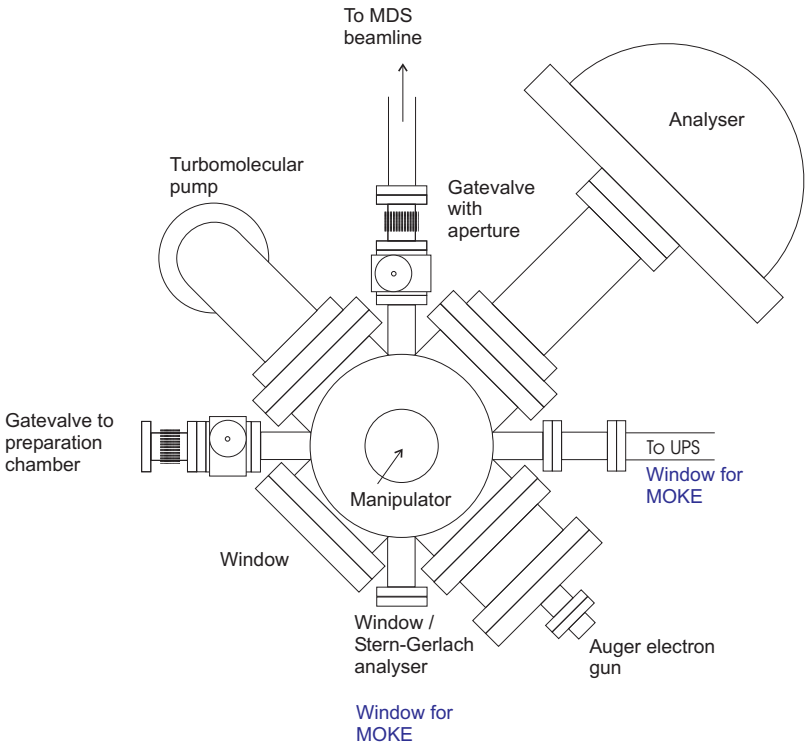

Figure 3.3: Schematic of the analysis chamber. Text in blue describes components on the lower level of the chamber, whilst text in black refers to components on the upper level.

To reduce the base pressure in the system a Mullard triode ion pump has been added underneath the chamber which is used in conjunction with an Edwards EXT250 turbo-molecular pump with nominal pumping speed of 250 ls^{-1}. As the ion pump had previously been used for an extended period on other systems and had been left at atmosphere for several years, testing revealed that the pressures it was capable of achieving were higher than those required. For this reason, the electrodes were removed, disassembled and cleaned by bead-blasting to expose unreacted Ti. The addition of this pump to the analysis chamber has reduced the base pressure from approximately 1×10^{-9} mbar to 4×10^{-10} mbar. The magnet strengths were also checked and found to be within normal operating parameters. A Ti sublimation pump (TSP) is situated above the ion pump and is timed to fire every four hours when experiments aren't in progress.

3.3.1 Energy Analyser

An Omicron ESA 125 hemispherical analyser is mounted at 45° to the beam-line and the UPS source and at 90° to the electron gun. It is this analyser that is used to collect MDS, UPS and AES spectra.

As the electrons emitted from the sample enter the analyser, they initially pass through a lens column whereby the initial lens selects the analysis area on the sample and the angular acceptance. Under normal operating conditions, a high magnification setting is selected which has a $\pm\ 8°$ acceptance angle from the normal and an analysis area of < 1.5 mm diameter. The second lens retards or accelerates the electrons by an amount, *R*, determined by the lens voltages. Electrons within a certain bandwidth of the pass energy, E_P, are admitted into the detector where they are detected and amplified by one of seven electron multipliers. These measure the kinetic energies of the electrons, E_{K_m}, as:

$$E_{K_m} = R + E_P + \phi_a, \tag{3.1}$$

where ϕ_a is the work-function of the analyser measured to be 4.25 eV. This measured kinetic energy is equal to the true kinetic energy of the electron, E_K, plus the sample work-function, ϕ_s such that:

$$E_{K_m} = E_K + \phi_s. \tag{3.2}$$

As such, when converting the energy spectrum scale from the measured kinetic energy, E_{K_m} to the actual kinetic energy, E_K, it is necessary to know the sample work-function, ϕ_s. The analyser has a minimum 10 meV energy resolution ensuring highly precise spectra.

3.3.2 Auger Electron Gun

The electron source used for AES is a York Electron Optics 04 Schottky field emission gun. This provides a finely focused, high-current beam with an energy variable between 1 keV and 10 keV. A sharp tip held at a negative potential to a nearby electrode causes a sufficient electric field gradient for electrons to be extracted from the tip. When conducting AES, the gun is set to produce electrons of 3 keV energy using a filament current of 2.44 A. The analyser is set to a constant retard ratio mode whereby electrons entering the analyser are retarded by a constant proportion of their kinetic energy by altering the analyser pass energy. This mode has a variable energy resolution.

3.3.3 Ultraviolet Photoelectron Spectroscopy

The ultraviolet photo-electron spectroscopy (UPS) source is an Omicron VUV HIS 13 designed to operate with various discharge gasses, however, under our experimental arrangement it is only used with He. The discharge gas is leaked into a differentially pumped capillary to a pressure of $\sim$1 mbar and a potential of 1000 V is applied to cause breakdown. Once this has occurred, the voltage reduces to approximately 650 V which is current limited to 80 mA. This produces a He I α discharge of energy $h\nu = 21.22$ eV.

When conducting UPS, the analyser is set to a constant pass energy mode whereby the analyser pass energy is held constant at 10 eV and the retarding voltage is altered during the scan. This mode has a fixed resolution.

The background pressure in the analysis chamber during UPS operation is generally $\sim 5 \times 10^{-8}$ mbar depending on the inlet He pressure.

3.3.4 Manipulation

The analysis chamber is equipped with an Thermo VG five-axis manipulator capable of cooling to LN_2 temperatures as well as dc and PBN sample heating.

3.4 Magneto-optic Kerr Effect

3.4.1 Design

The addition of an *in situ* magneto-optic Kerr effect magnetometer (MOKE) to our experimental arrangement provides the ability to determine a sample's bulk magnetic properties and allows a comparison with the surface magnetic properties measured with SPMDS.

The design chosen was loosely based on an *in situ*, dc MOKE at the *Max Planck Institute for Microstructure Physics*. Our arrangement is illustrated in figure 3.4.

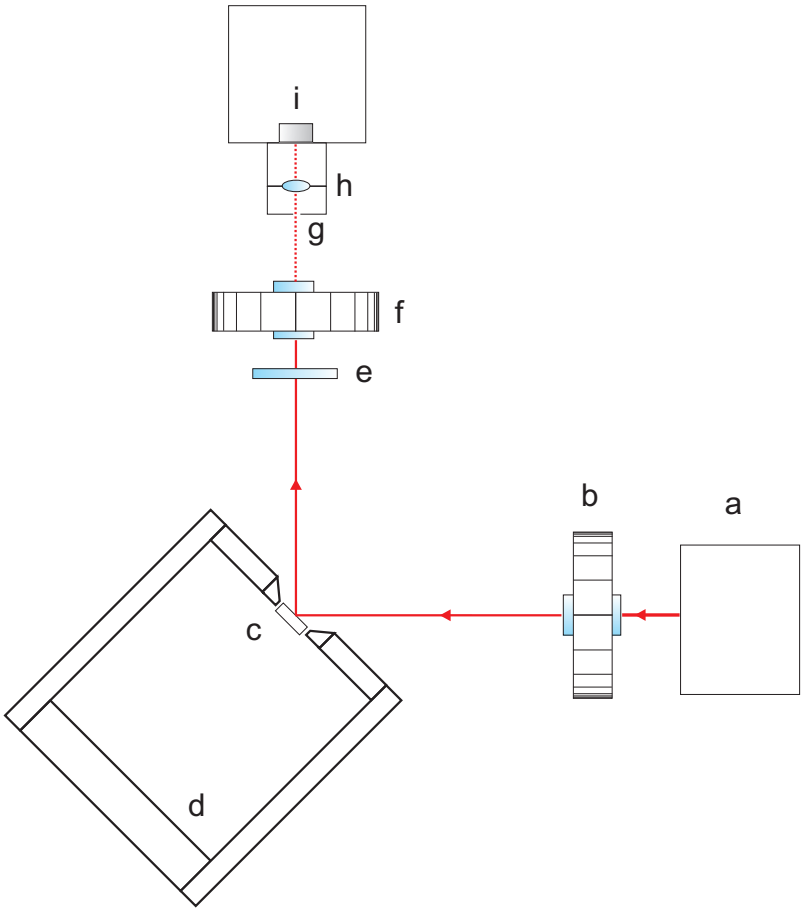

Figure 3.4: MOKE arrangement consisting of: a) 670 nm, 3.5 mW laser, b) Glan-Taylor polariser on rotating mount, c) sample, d) electromagnet, e) quarter wave plate f) Glan-Taylor analyser on rotating mount, g) 0.5 mm aperture, h) planoconvex lens (focal length 25 mm), i) photodiode with integrated pre-amplifier.

A Schäfter and Kirchoff GmbH laser with 3.5 mW, 670 nm solid state laser diode was chosen as our light source for its ability to produce an extremely stable intensity beam of constant power. This beam initially passes through a Glan-Taylor polariser to linearly

polarise the beam. Glan-Taylor polarisers were selected over Glan-Thompson or sheet polarisers for their low extinction ratio (10^{-5}). These polarisers are anti-reflection (AR) coated for 670 nm light to prevent multiple reflections. The polarised beam then passes into the chamber through a DN40CF window and impinges onto the sample at 45°. The sample is situated at the centre of the chamber and is surrounded by an electromagnet constructed out of soft iron, chosen for its high magnetic susceptibility and low coercivity. All corners have been rounded and all screws inset to minimise flux leakage. 250 turns of polyimide coated copper wire of 0.8 mm diameter, wound around three sides of the magnet were used to maximise the field which was then characterised with a Hall probe. This wire was chosen for its ability to be baked to 150 °C without causing excessive outgassing. The poles of the magnet are tapered to give a high field at the tips and to allow the laser to illuminate the sample and reflect directly to the detector for the specified angles. At a current of 3.0 A (the maximum current for which outgassing is negligible) a field of (420 ± 10) Oe is produced at the central point between the pole pieces.

The reflected beam passes out of the chamber through another DN40CF window, through a quarter wave plate to produce a linear polarisation from the now elliptically polarised light, then into another Glan-Taylor polariser on a rotatable mount which acts as an analyser of the linear polarisation. The beam then passes through a lens and onto a Hammamatsu S8745 photodiode with integrated pre-amplifier. This photodiode was chosen for its spectral response, its very low dark noise and its relatively high cut-off frequency, allowing measurements to be acquired quickly. Electronic circuitry was designed to accommodate the photodiode. The analysing polariser is rotated until the photodiode is no longer saturated. This generally occurs at about 89.5° to the first polariser; i.e. when they are almost completely crossed.

A shroud was constructed for both the laser and detector to prevent stray light from entering the system and increasing the amount of noise. Supports have been built to attach the laser and polariser to DN40CF windows on the analysis chamber at right angles to one another. The photodiode is positioned upon an adjustable stage to assist with alignment.

The system has been interfaced using LabVIEW, and a virtual instrument has been designed and calibrated to automate the procedure of obtaining a hysteresis loop. The photodiode is interfaced with LabVIEW so that voltages across it are recorded. LabVIEW generates a signal which is fed into a power amplifier which, in turn, drives the electromagnet surrounding the sample to produce a slowly sweeping magnetic field.

3.4.2 Testing

The MOKE has been tested *ex situ* with a 100 nm permalloy ($Ni_{80}Fe_{20}$) sample grown on Si(111) in a separate sputtering rig. An example hysteresis loop for the sample obtained by this method is shown in figure 3.5. The magnetisation switches are clearly visible. An absolute calibration for the magnetisation is not possible as the actual voltage output from the photodiode depends on the alignment of the sample and the reflectivity of where the laser is incident on the sample, which alters every time the MOKE or sample is moved even small amounts. A comparison of the coercivity with a hysteresis loop obtained using a vibrating sample magnetometer indicates an accurate field calibration.

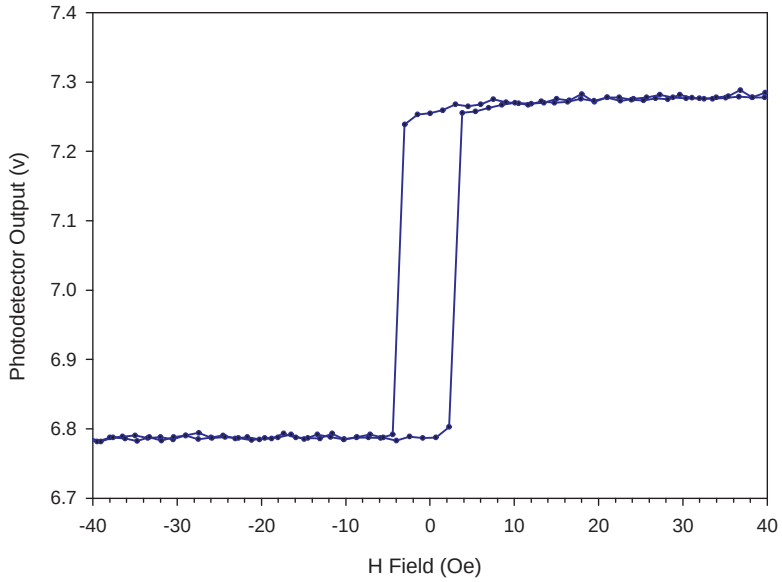

Figure 3.5: Hysteresis loop for 100 nm permalloy on Si(111) sample, averaged over 7 runs. A linear voltage drift has been corrected for.

3.5 Stern Gerlach Analysis

A Stern Gerlach analyser illustrated in figure 3.6 was added to the analysis chamber in direct line of site of the metastable source to quantitively assess the polarisation of the He beam. Alignment was conducted so that after the He beam has passed through the analysis chamber, it then continues through a rectangular aperture of length 2 mm and width (47 ± 9) μm. From here it enters into a flight tube of internal diameter 5 mm and length 300 mm where it is subjected to a uniform magnetic field gradient provided by

a horseshoe magnet with specially tailored, soft Fe pole pieces as illustrated in figure 3.6 b). This field gradient causes a splitting of the beam to occur along the axis of the field gradient. At the end of the flight tube is a collar pumped by a 50 ls^{-1} turbomolecular pump containing a micro-channel plate at a potential of between 2 and 3 kV as is illustrated in figure 3.6 a) and c).

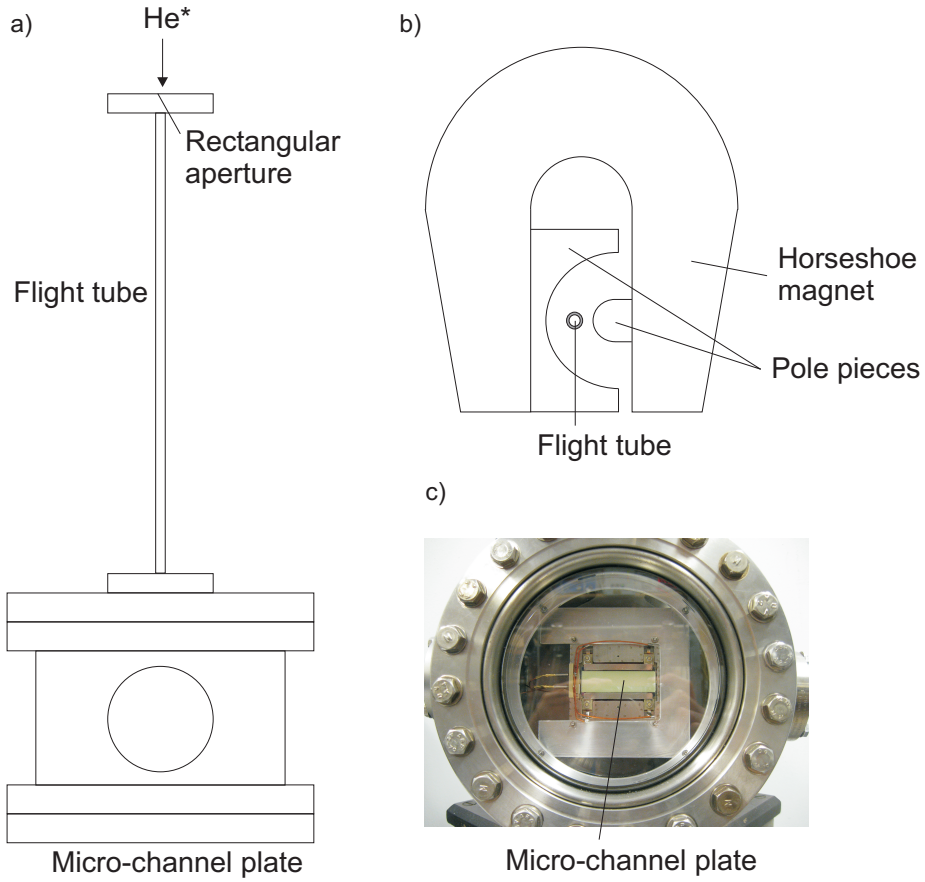

Figure 3.6: Stern-Gerlach equipment. Illustration a) shows a top view schematic of the Stern-Gerlach setup. b) is an illustration of the magnet used to produce the uniform field gradient. c) is an end-on photograph of the micro-channel plate inside the collar.

A computer interfaced CCD camera was mounted in front of the microchannel plate to capture the phosphorescence produced by the beam on the plate. As the polarisation of the He beam is reversed by reversing the circular polarisation of the laser beam in the polarisation section of the beam-line, a shift in the position of the intensity maximum on the screen can be observed.

To obtain reasonable images of the splitting, a pressure of $< 10^{-7}$ mbar is necessary in the collar. The potential on the microchannel plate was increased to just below its saturation point. An applied field of approximately 0.7 Oe was generated by the Helmholtz coils. This was shown to be sufficient to provide an axis of orientation for the He^*.

3.5.1 Extent of Polarisation

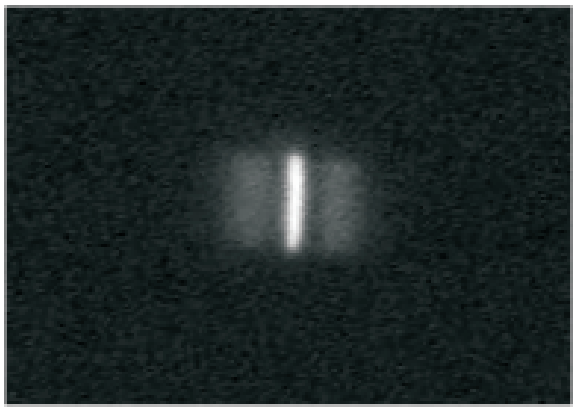

Figure 3.7: An image of the splitting of the unpolarised He beam into its constituent states. A current of 1.0 A was applied through the Helmholtz coils to provide an axis of magnetic orientation for the He.

Figure 3.7 is a photo of the splitting apparent on the microchannel plate when the He beam is not polarised, but the magnet is in place so that splitting between the sub-levels occurs. The central spot is much brighter than the two side spots (for which $m_s = \pm 1$). This is because as well as containing the $m_s = 0$ state, the beam will also contain photons as the plate is in line of site of the source. When the small disc in the beam-line is positioned to block photons, figure 3.8 results. An intensity profile of this image is also provided.

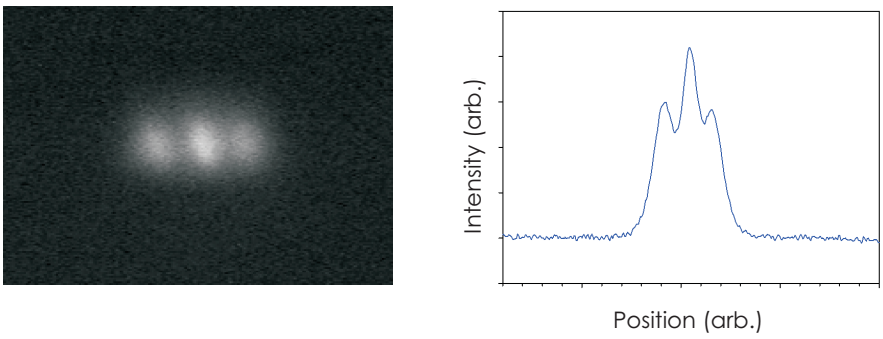

Figure 3.8: a) is an image of sub-level splitting with no beam polarisation. b) is an intensity profile for the image acquired using linescan software. The three separate states are clearly visible.

By fitting 3 normal distributions to the data for the 3 different values of m_s it is possible to estimate the different contributions from each. The best fit suggests a splitting of (36 ± 3) %, (34 ± 2) % and (30 ± 2) % for the m_s = -1, 0 and +1 states respectively which is close to the expected values of 33% for each. Any difference may be due to one of the

states hitting the side of the flight tube and de-exciting before reaching the microchannel plate.

When the He beam is polarised, one would expect all of the He to be entirely in either the m_s =-1 or +1 state. By applying normal distributions to the linescans of the polarised images, it is possible to estimate the polarisation of the He beam. Such normal fits to the data for a polarised beam are provided in figure 3.9. Reallignment of the magnets and source relative to the Stern Gerlach analyser has taken place between figures 3.7, 3.8 and 3.9. This has lead to different intensities and shapes of the resulting beams.

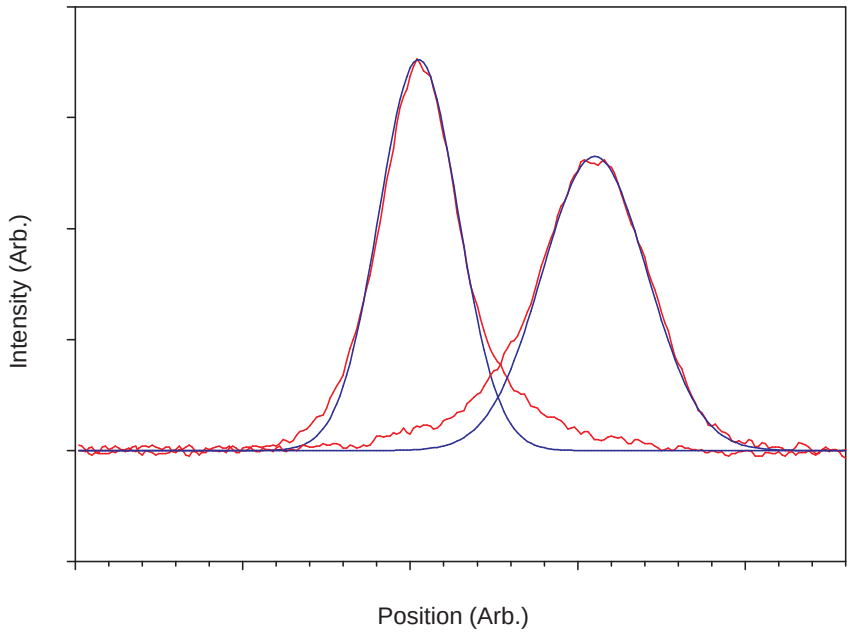

Figure 3.9: Estimate of He beam polarisation for $m_s = +1$ and $m_s = -1$. The blue curves show the fitted normal distributions to the experimental data (red).

The volumes under the normal distributions and the experimental distributions are calculated and the proportional difference is taken to be the extent of the polarisation. It is apparent that the data are not quite normally distributed even taking into account unpolarised states. This results in a slight underestimation of the polarisation in both cases. The left and right state polarisations are estimated at (90.1 ± 7.6) % and (90.3 ± 2.7) % respectively. A difference in the shape and width between the polarised distributions is thought to arise as a result of non-uniformities in the magnetic field gradient.

3.6 Preparation Chamber

The experimental arrangement has previously been limited by a lack of available flanges on the vacuum chamber. Also, by using evaporation sources in the same chamber as analysis is conducted, sample cleanliness is compromised as well as the absolute base pressure achievable. By introducing a separate chamber in which samples are prepared, contamination should be reduced and vacuum conditions should improve. This also allows further developments to the instrument such as the addition of *in situ* MOKE, as more flanges are made available. A schematic of the preparation chamber is presented in figure 3.10.

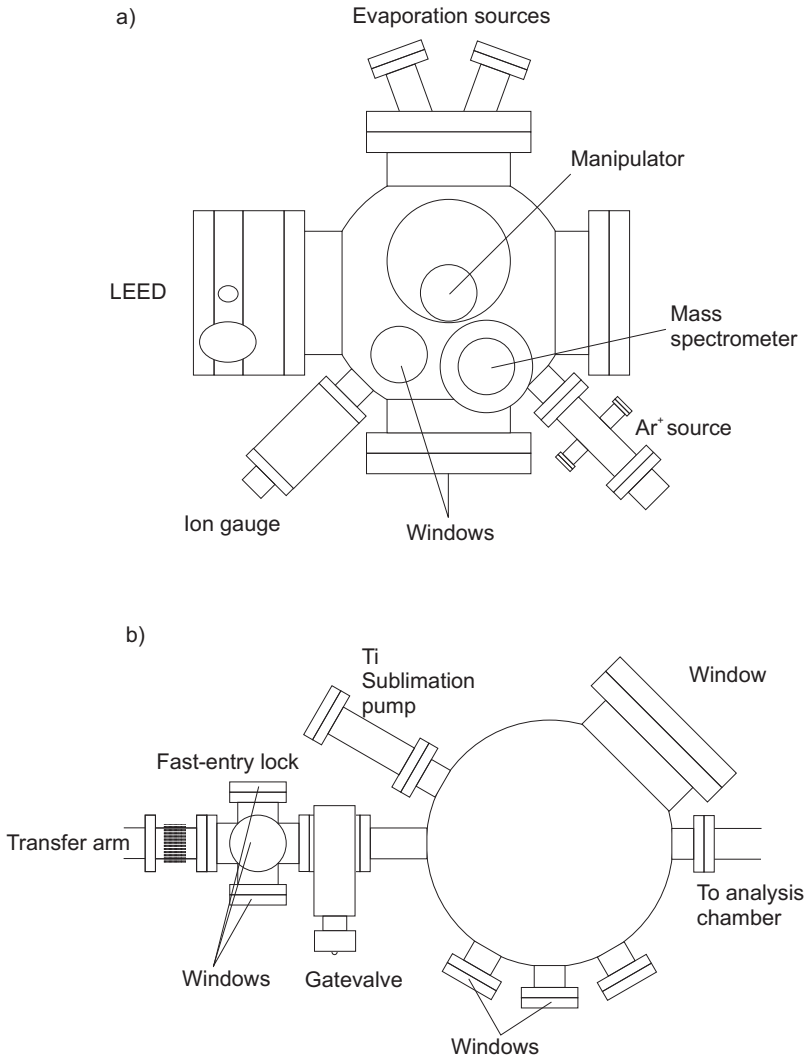

Figure 3.10: Schematic of the sample preparation chamber. a) and b) show the upper and lower levels respectively.

The chamber is pumped by an Edwards EXT 250 turbomolecular pump with a nominal pumping capacity of 250 ls^{-1} mounted at the chamber's base. A TSP is also present on

a DN40CF flange for which a controller was built to be triggered by an AML ion gauge controller.

As samples must be transferred from one chamber to another between growth and analysis, a transport mechanism was necessary. A magnetically coupled transfer arm with a spring-clip pincer on the end was used where the pincer accommodates the protrusion of the sample plate to prevent it from slipping. To grasp the sample plate, a small force needs to be applied initially to push the pincer jaws around the protrusion. To release the sample plate once it has been inserted into either manipulator, a slight twisting of the sample within the manipulator is required to open the jaws of the pincer. The two chambers are separated by a manually operated gate-valve.

The addition of the transfer arm between the chambers has also allowed a fast-entry lock to be added. This has been included so that substrates can be exchanged rapidly without having to take the entire preparation chamber up to atmospheric pressure and undergo a baking process every time a sample exchange takes place. A six-way cross has been attached between the transfer arm and the preparation chamber, with a manually operated gate valve located between the cross and the preparation chamber as is illustrated in figure 3.10. When the transfer arm is withdrawn from the preparation chamber and the gate-valve shut, the fast-entry lock and transfer arm may be vented so that a sample plate may be inserted into the pincer on the end of the transfer arm by opening the top flange on the six-way cross. Once this has been re-sealed, this part of the system is pumped down by a Edwards EXT75DX turbomolecular pump with a nominal pumping capacity of 61 ls^{-1}, backed by an Edwards RV3 rotary pump. This pumping system results in a base pressure in the fast-entry lock of 5×10^{-8} mbar without a bake. A power supply has been specially constructed for this turbomolecular pump. Once this section is pumped down sufficiently, the gate-valve may be opened and the sample transferred into the preparation chamber.

A four-source port has been attached to a DN160CF flange. Whereas previously, the combined preparation / analysis chamber only had space for one source at a time, the preparation chamber may have up to four, all pointing to the centre of the chamber. These may be used in unison which allows for the possibility of co-deposition in future work. An Omicron ISE10 Ar^+ ion gun is also attached to the system for sample cleaning.

A manipulator has been constructed for use on the preparation chamber. Although little horizontal (x-y) manipulation was necessary, the vertical, (z) range needed to be approx-

imately 240 mm to move the samples between the different levels in the chamber which was not practical using a regular edge-welded bellows arrangement. A full 360° θ rotation was also necessary. A 300 mm travel magnetically-coupled transfer arm mounted vertically onto a port-aligner was chosen and attached an Omicron sample stage with in-built quartz crystal and e-beam sample heating.

The residual gasses present in the chamber after bake-out have been monitored with a VG Gas Smart IQ+ residual gas analyser to ensure no significant contaminants were present within the new system. The results are presented in figure 3.11.

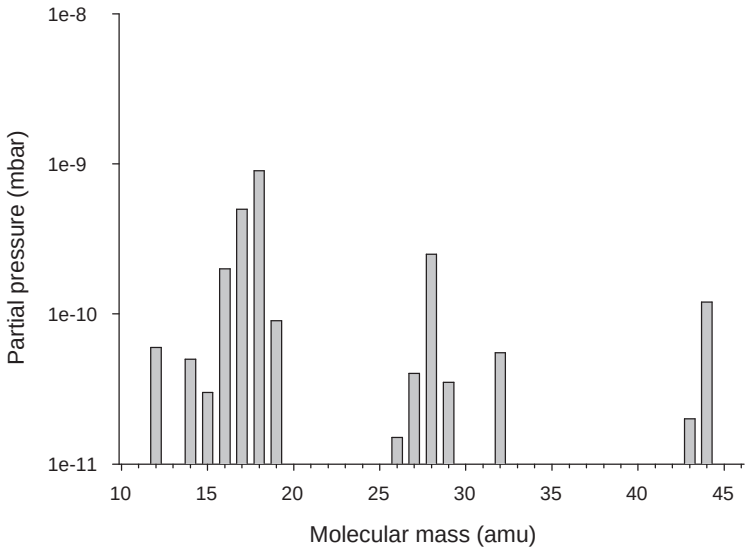

Figure 3.11: Mass spectrum of partial pressures within the preparation chamber. The main constituents arise from water, carbon monoxide and carbon dioxide.

It is evident from the figure that the main contaminants within the chamber are water, which contributes to masses 17 and 18, and carbon monoxide and dioxide which contribute to peaks 28 and 44.

3.7 Deconvolution

In the Auger neutralisation process, the initial binding energies of the neutralising and ejected electrons are not directly related, and they may both originate from any energy within the filled band of the surface. As the kinetic energy of the emitted electron is dependent on both its initial binding energy and the binding energy of the neutralising electron, the kinetic energy spectrum does not represent directly the filled bands within the

DOS, but is instead a self-convoluted (auto-convoluted) energy spectrum. Such spectra generally have broad features, so the exact energies of particular bands are difficult to locate. This is true for any surface which undergoes RI+AN.

It is possible to recover some of the information on the original DOS by deconvoluting these convoluted spectra. The predominant methods previously attempted to perform deconvolution are: the spline fitting and iterative solution approach,[43,78,53] a Fourier transform technique[52,54] and a step by step deconvolution.[51] Out of most recent work, the spline fitting and iterative solution approach has been preferred.[46]

Within this chapter however, a Fourier technique is demonstrated using inverse signalling. This is the simplest deconvolution technique to perform, as no iterative processes are involved and no noise filtering or smoothing need be applied to the spectrum before it undergoes the deconvolution process. However one must be aware of potential problems with the technique and other deconvolution techniques may yield better results.

Structures present in the deconvolution should also be present in the first derivative of the experimental spectrum,[51] as although both are based on completely different mathematical procedures, the same structures should occur in the same energy positions. However, where the deconvolution should preserve the relative magnitude of the peaks from the deconvolution, the differentiated spectrum may not. A discussion of how the differential of the convolution relates to the DOS is provided in reference 43.

Unlike a real DOS the deconvolution can go negative. This is due to the loss of absolute magnitude information during the deconvolution process and does not represent a real effect.

3.7.1 Method of Deconvolution

Figure 3.12 shows how the ejected energy spectrum, $X(E)$, is related to the excited electron distribution within a surface and $F(\varepsilon)$ and the transition density $U(\varepsilon)$ (related to the density of states).

The neutralisation electron has an initial energy of $(\varepsilon + \Delta\varepsilon)$ and the ejected electron has an initial energy of $(\varepsilon - \Delta\varepsilon)$.

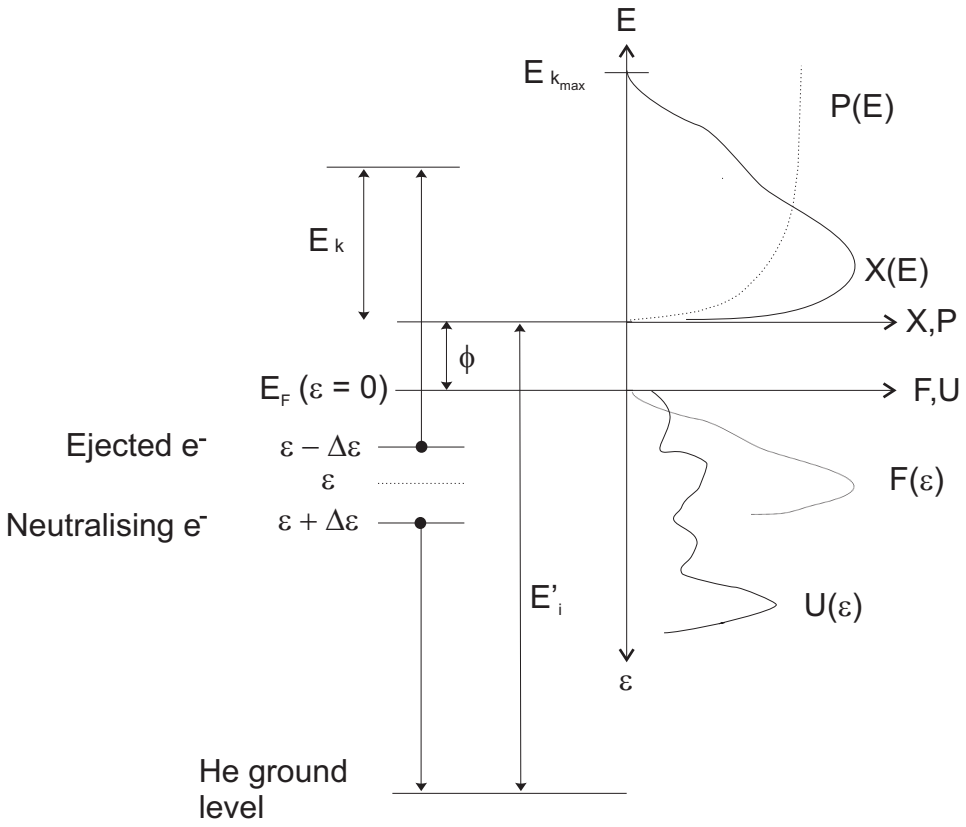

Figure 3.12: Diagram relating the electron distribution within a surface to the ejected electron spectrum.[51]

If *X(E)* is the electron kinetic energy distribution from the MDS spectrum, then:

$$F(E) = X(E)/P(E), \tag{3.3}$$

where *F(E)* is the broadened distribution of electrons inside the solid and *P(E)* is the electron escape probability. As the escape probability increases logarithmically with energy, this term can be neglected when considering only the high energy electrons that make up the surface states, as it is effectively constant over the relatively narrow widths of the valence band assuming a large enough E_i'.[79] This is especially true when looking at only the high energy surface states for which MDS is suited.

We can now change variables from E to ε, the electron binding energy within the DOS. From figure 3.12 we can see that by equating the energy released by the neutralisation electron to the energy gained by the ejected electron:

$$E_K + \phi + (\varepsilon - \Delta\varepsilon) = E_i' - \phi - (\varepsilon + \Delta\varepsilon), \tag{3.4}$$

where ε is the binding energy of the electrons involved in the transition relative to E_F, E_K is the kinetic energy of the detected electrons, E_i' is the effective ionisation potential of the

metastable He near to the surface, and ϕ is the surface work-function.[51] Therefore:

$$E_K = E_i' - 2(\varepsilon + \phi). \tag{3.5}$$

Now $F(\varepsilon)$, the transition probability is given by the self-folded integral:

$$F(\varepsilon) \propto \int_{-\varepsilon}^{\varepsilon} |H_{fi}|^2 \, N(\varepsilon - \Delta\varepsilon) \, N(\varepsilon + \Delta\varepsilon) \, d(\Delta\varepsilon), \tag{3.6}$$

where $N(\epsilon)$ is the surface density of states and H_{fi} is the Auger matrix element and is dependent on the features of surface charge density, where:

$$|H_{fi}|^2 = H_1(\varepsilon - \Delta\varepsilon)H_2(\varepsilon + \Delta\varepsilon). \tag{3.7}$$

If we assume that both the matrix elements are equal,[51,43] such that:

$$H_1 = H_2 = H, \tag{3.8}$$

these matrix elements may then be combined with N(ε) such that:

$$U(\varepsilon) = H(\varepsilon)N(\varepsilon), \tag{3.9}$$

where $U(\varepsilon)$ is the transition density for an electron in the surface i.e. the LDOS modified by the transition matrix elements. Now:

$$F(\varepsilon) \propto \int_{-\varepsilon}^{\varepsilon} U(\varepsilon - \Delta\varepsilon) \, U(\varepsilon + \Delta\varepsilon) \, d(\Delta\varepsilon). \tag{3.10}$$

In reality, H_1 and H_2 do differ from one another, which leads to $U_1(\varepsilon - \Delta\varepsilon)$ and $U_2(\varepsilon - \Delta\varepsilon)$, but this is impossible to solve by self-deconvolution. The ramifications of this are detailed in reference 43.

To adapt the equation into the form of a convolution, we change the variables so that:

$$x = 2\varepsilon, \;\; y = \varepsilon + \Delta\varepsilon. \tag{3.11}$$

Now:

$$F(\varepsilon) \propto \int_{-\infty}^{\infty} U(y) \, U(x - y) \, dy. \tag{3.12}$$

This equation is now in the form of a convolution.

The limits are increased to $-\infty$ to $+\infty$ to form a continuous distribution, which is a condition of the convolution function. In reality this makes no difference to our spectra as outside of the range $-\varepsilon$ to $+\varepsilon$, the intensity should be zero.

$$\mathscr{F}\{F(\varepsilon)\} \propto \int_{-\infty}^{\infty} exp(-ikx)dx \int_{-\infty}^{\infty} U(y)\, U(x-y)\, dy, \tag{3.13}$$

where $\mathscr{F}\{F(\varepsilon)\}$ is the Fourier transform of $F(\varepsilon)$. As $F(\varepsilon)$ is only proportional to the density of states anyway, any normalisation factors arising from the Fourier transform have been adopted by the proportionality.

$$\mathscr{F}\{F(\varepsilon)\} \propto \int_{-\infty}^{\infty} U(y)\, dy \int_{-\infty}^{\infty} U(x-y)\, exp(-ikx)\, dx. \tag{3.14}$$

We now define:

$$z = x - y, \tag{3.15}$$

$$\mathscr{F}\{F(\varepsilon)\} \propto \int_{-\infty}^{\infty} U(y)\, exp(-iky)\, dy \int_{-\infty}^{\infty} U(z)\, exp(-ikz)\, dz \tag{3.16}$$

$$\propto \mathscr{F}\{U(y)\}\mathscr{F}\{U(z)\}, \tag{3.17}$$

and so:

$$\mathscr{F}\{F(\varepsilon)\} \propto \mathscr{F}\{U(\varepsilon+\Delta\varepsilon)\}\mathscr{F}\{U(\varepsilon-\Delta\varepsilon)\}. \tag{3.18}$$

However, the Fourier transform of a function is independent of its variable so that:

$$\mathscr{F}\{F(\varepsilon)\} \propto \mathscr{F}\{U(\varepsilon)\}\mathscr{F}\{U(\varepsilon)\}, \tag{3.19}$$

$$\propto [\mathscr{F}\{U(\varepsilon)\}]^2, \tag{3.20}$$

and hence:

$$U(\varepsilon) \propto inv\mathscr{F}(\sqrt{\mathscr{F}\{F(\varepsilon)\}}). \tag{3.21}$$

This calculation is achieved using a simple programme written in LabVIEW taking the convoluted spectrum and returning the deconvoluted spectrum. The Fourier transform

used considers both real and imaginary components so that phase information on the spectrum is not lost.

Complete recovery of the deconvoluted signal is not possible as other signals will be convoluted with our initial signal. These arise from sources such as instrument noise, where the parameters are not known. There is also an energy broadening inherent in the Auger process.[68] In reality, this leaves us with $U^*(\varepsilon)$, the effective deconvoluted signal.

3.7.2 Results

To illustrate the effectiveness of the deconvolution technique and to ensure that it works correctly, a deconvoluted MDS spectrum has been compared to a differentiated MDS spectrum to ensure features occur at the same energies, as Fourier transform deconvolutions can lead to spurious peaks not present in the DOS and also possible energy shifts in the peak locations. It is essential that this procedure is conducted whenever a spectrum is deconvoluted in this method.[51]

This comparison has been conducted for a coverage of 2 ML of $HoSi_{2-x}$ on Si(111) and is presented in figure 3.13.

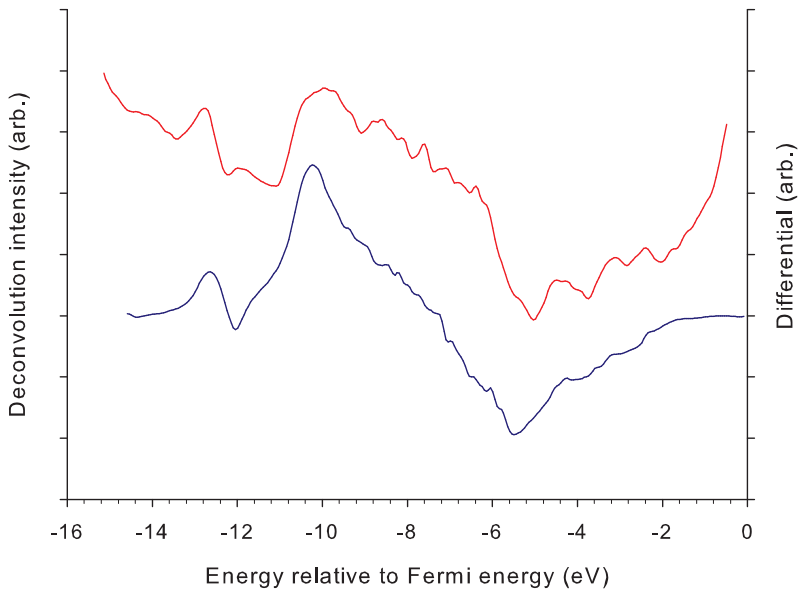

Figure 3.13: A comparison of the deconvoluted and differentiated MDS spectrum for 2 ML $HoSi_{2-x}$ on Si(111). The red line shows the deconvolution whilst the blue line shows the differential

Both the deconvolution and differentiated spectra are of a very similar shape with main features occurring at the same energies. The only regions where features arise in the deconvolution, but not in the differentiated spectrum is in the low energy tail, where count rates are low and secondary electrons dominate. The deconvolution also deviates significantly at very high energy where count rates are very low. The 3 features between approximately 7 eV and 3 eV are present in both plotted lines, but are much more intense in the deconvoluted spectrum. Differences in intensities are expected, as the differentiated spectrum is not a true representation of the DOS.

Hagstrum suggests that in some scenarios the deconvolution can be replaced by the differential to obtain the energies of states within the DOS as a less labour intensive process, however this may not always be the case.[51]

To demonstrate how much of the original signal is retrieved by the differentiation method, a UPS spectrum for the Si(111) 7×7 surface has been convoluted (again using a programme written in LabVIEW) and then differentiated. The original UPS spectrum and the differentiation of the convoluted spectrum are all shown in figure 3.14.

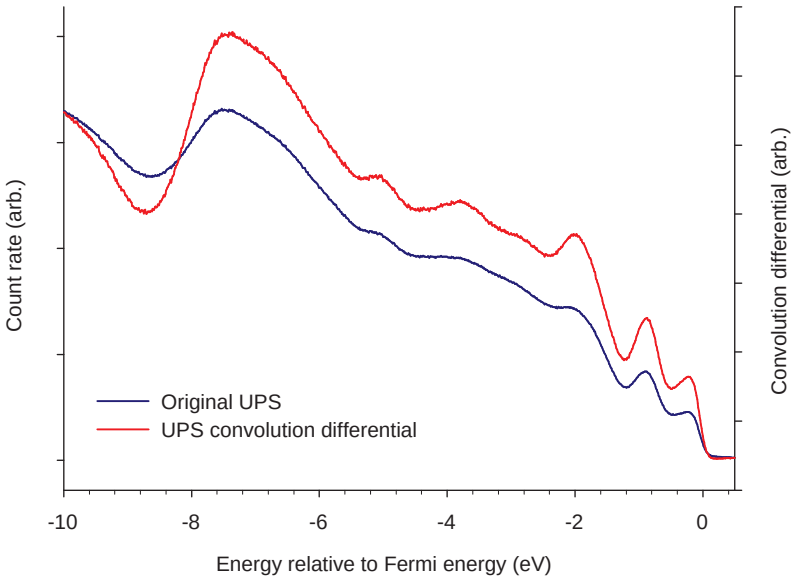

Figure 3.14: UPS spectrum for Si(111) 7×7 spectrum alongside the differentiation of the convolution of the UPS spectrum.

While the features are all still present in the differentiation at the same energies as the original spectrum, they have been slightly exaggerated and the noise level has increased. This does, however demonstrate the effectiveness of the differentiation in determining the

energies of states from a convoluted spectrum.

Chapter 4

Rare Earth Silicide on Si(001)

4.1 Introduction

4.1.1 Background

Metal-semiconductor interfaces are one of the fundamental components in modern electronics, with novel systems continuously being developed to meet new demands and more tailored applications. Such a metal-semiconductor system of future technological potential is the rare earth (RE) silicon system. In extensive studies initiated by IBM, it has been found that when trivalent RE metals (such as Er, Ho and Dy) are deposited on Si(001) and Si(111) substrates elevated to temperatures as low as 300 °C, a reaction occurs, and a RE silicide forms.[15] These silicides have extremely low Schottky barrier heights (0.3-0.4 eV)[80] on *n*-type Si substrates; lower than any other silicide. This, coupled with their high thermal and electrical conductivity ($2.9 \times 10^4 (\Omega\ \mathrm{cm})^{-1}$ for $ErSi_2$) make them of potential use for future electronic devices.[14,81]

Rare earth silicides on the more open Si(001) substrate are of particular interest due to the fact that the silicide lattice mismatch to the substrate is low in some directions leading to epitaxial growth, but high in others, restraining growth. Such a lattice mismatch is illustrated in figure 4.1. This mismatch difference leads to the formation of nanowires (NWs)[21] under certain conditions and RE silicide islands under others. Such NWs can grow to be up to several microns in length and are generally between 1.5 and 10 nm wide depending on the mismatch, which depends on the RE metal used, and local conditions such as deposition temperature and coverage.

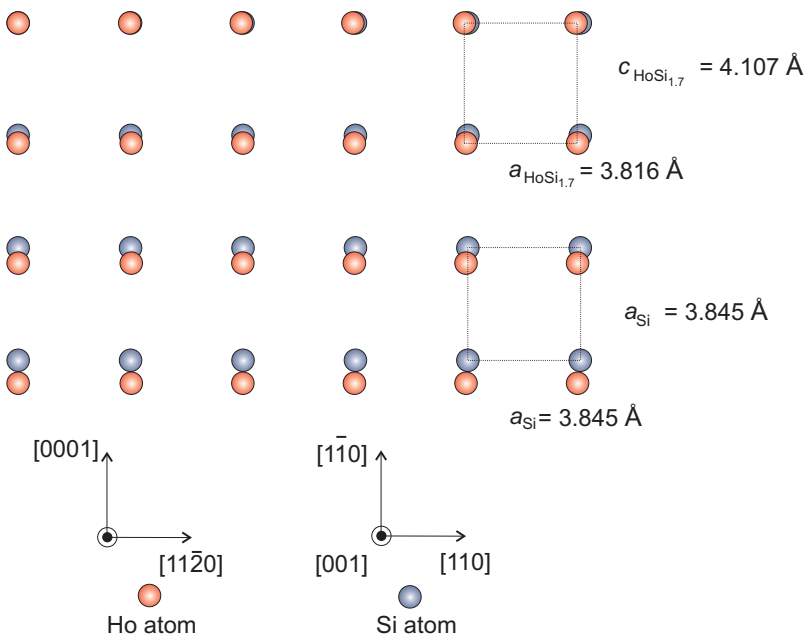

Figure 4.1: Illustration of the lattice mismatch between Si(001) and $HoSi_{2-x}$. The lattice mismatch of the silicide is much lower in the $[110]$ direction compared to the $[1\bar{1}0]$ direction of the Si substrate.

Nanowires are of fundamental interest as quasi-1D systems. The electronic properties of such systems can be very different from 2D and 3D ones and have been shown to exhibit unusual quantum effects.[82,83] Technologically, they have potential use as nanointerconnects between components,[84] since self-assembled NW widths are less than those currently achievable through nanolithographic techniques and tend to be constructed of single crystals and so can handle high current densities.[85] They also have potential as switches,[86] memory storage devices[87] and as elements in logic circuits.[88] Nanowires on Si substrates are of particular importance as they may be integrated simply with existing technology. Self-assembled NWs, which form spontaneously, are of particular importance due to the lack of intervention required during growth. RE silicide growth on Si(001) is one such example of a system that forms self assembled NWs.

Rare earth silicides have already been suggested for potential technological applications specific to their electronic properties such as tunable IR detectors,[89] ohmic contacts[84] and multilayer devices.[90] Scanning tunnelling spectroscopy (STS) has shown that RE silicide NWs are metallic,[91] which adapts them to many of the future possibilities for NWs mentioned earlier. Applications have however, so far not been developed, mainly due to the readiness of the surfaces to react with O_2, and the difficulties of mass manufacturing, as currently these silicides have historically been prepared epitaxially under UHV conditions.

Some triumphs have been made with other, more industrial scale techniques such as rapid annealing and co-deposition methods.[92,93,94] Progress is also being made in controlling the length and growth direction of the NWs.[95,96]

4.1.2 Growth

The clean Si(001) surface forms a 2×1 unit cell after flashing followed by a slow cool to room temperature whereby neighbouring Si atoms form dimers to reduce the number of dangling bonds on the surface as shown in figure 4.2. These dimers tilt to further reduce the degeneracy of the dangling bonds which oscillate at room temperature. When the surface is cooled to low temperatures (approximately 200 K),[97] these dimers assume alternate tilts along the dimer rows and therefore form a $c(2 \times 4)$ reconstruction.[98]

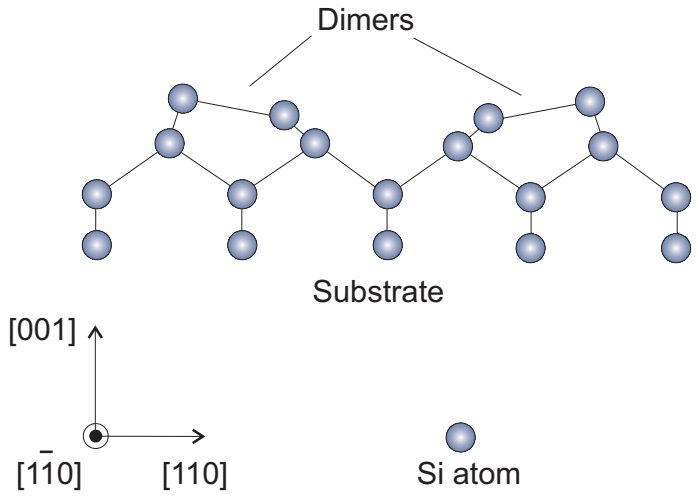

Figure 4.2: A model of the Si(001) 2×1 dimered surface illustrating the alternating tilts of the dimers which occurs at low temperature.

Initially, when a RE metal is deposited on a hot Si(001) substrate, a 2D silicide forms with Stranski-Krastanov growth due to the lattice mismatch.[91] Other areas of the substrate may be left exposed, or may contain 3D silicide structures even at very low RE coverages. For higher coverages (> 1 ML), Volmer-Weber growth may also occur. In the silicide regions, the reconstruction depends on the particular rare earth metal used and local conditions. For example, Er forms 2×3, 5×2 and $c(5 \times 4)$ reconstructions and Gd, Dy and Ho form 2×4 and 2×7 reconstructions.[23]

Ohbuchi and Nogami,[99] in one of the few articles that investigates in detail the reconstructions between the NWs have shown that on $HoSi_{2-x}$ on Si(001), this 2×4 phase

dominates at low coverages with NWs also present on the surface and some contribution of 2×1 from unreacted Si dimers. When the coverage of Ho is increased, the 2×7 phase becomes apparent, coexisting with the 2×4 reconstruction. At greater coverages still ($\gtrsim$0.6 ML), when 3D islands become more dominant, the proportion of the surface dominated by the 2×4 decreases again, with a resurgence of unreacted substrate. This suggests the energetic preference of the 3D islands to either the 2D reconstructions or NWs. As coverages of RE increase, these 3D NW or island structures which have a $c(2 \times 2)$ surface reconstruction become more prevalent alongside the silicide covering much of the rest of the surface. The bulk of evidence now suggests that these NWs assume a hexagonal defect AlB_2 crystal structure as shown in figure 4.3.[81,100] The structure of the nanoislands however is more contentious, with both hexagonal AlB_2 and tetragonal $ThSi_2$ structures being suggested.[101,102]

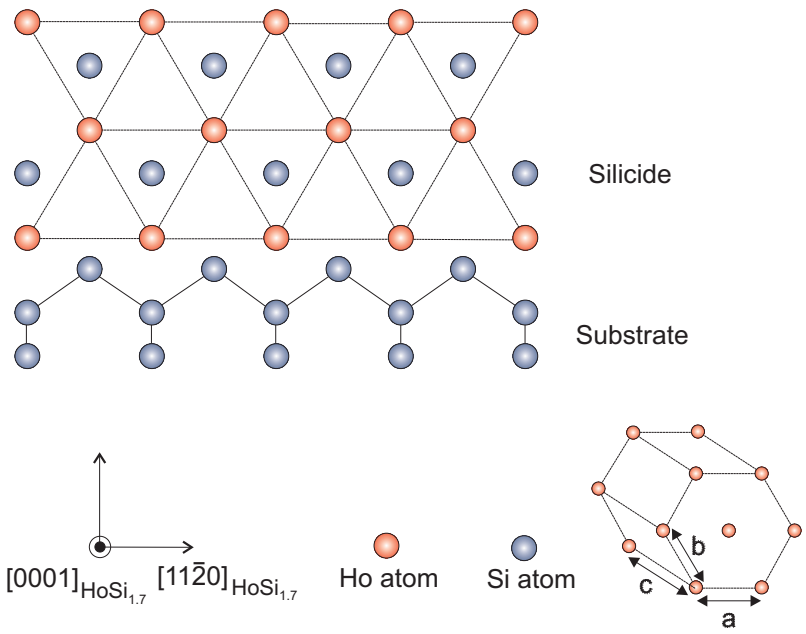

Figure 4.3: Cross-sectional view of the AlB_2 crystal structure of $HoSi_{2-x}$ on Si(001). Si vacancies are not shown. A 3D drawing of an hexagonal crystal is also shown for reference.

For the hexagonal AlB_2 structure, growth occurs such that the *c* axis is parallel to the surface of the Si(001). The minimum mismatch is between the $[11\bar{2}0]$ direction in the RE silicide and the [110] direction of the Si. Nanowire growth occurs in this direction due to the effects of this strain. The mismatch is greatest between the [0001] direction in the RE silicide and the $[1\bar{1}0]$ axis of the Si. This restricts growth. When the mismatch is also relatively large between the $[11\bar{2}0]$ and [110] direction ($\gtrsim 2\%$), the strain energy can be minimised by the silicide forming islands instead of NWs;[103] however, NW growth may be

encouraged by growth with solid phase epitaxy.[104] It is such a mismatch that determines the dimensions of the nanowire and is illustrated between the $HoSi_{2-x}$ and Si(001) unit cell in figure 4.1. Lattice mismatches between Si(001) and some RE silicides are provided in table 4.1 below.

RE silicide	Mismatch [110]	Mismatch $[1\bar{1}0]$	Nanowires
Er[81,105]	-1.3%	+6.5%	Yes
Dy[95]	-0.1%	+7.6%	Yes
Sm[95]	+1.6%	+9.8%	Yes
Ho[105]	-0.8%	+6.8%	Yes
Nd[106]	+7.3%	+16.0%	No

Table 4.1: Epitaxial mismatch for various RE silicides with Si(001) and whether NWs form. Where NWs do not form, islands will.

For some RE silicides such as Dy, Ho and Er,[105] vacancies may exist within the NW to relieve strain. This modifies the stoichiometry from $RESi_2$ to $RESi_{2-x}$ where $0 \leq x \leq 0.3$. For Ho, x = 0.3.

The vast majority of previous studies have been aimed specifically at characterising the nanostructures, with very little work dedicated to the regions of the surface in between them, despite the reconstruction's importance to nanostructure formation, as it is here where RE atoms used in the nanostructure growth may be sourced from. For this reason, the work presented in this chapter has been conducted. Holmium has been used as the RE metal in this study because of its low lattice mismatch in the preferable direction of growth, its known trivalency and for the reason that very few other studies have been conducted on $HoSi_{2-x}$ on Si(001).

4.1.3 Relevance of MDS to the $RESi_{2-x}$ System

As MDS is sensitive only to the outermost orbitals of the surface, there is no significant contribution to the spectrum from the more tightly bound 4*f* electrons in the RE that do not contribute to the silicide formation. This differs from UPS, which probes deeper into the surface and suffers a significant contribution from these electrons. As such, MDS only detects the bands involved in the RE-Si bonding (the *s-p* states in the valence band) along with the hybridised *s-d* states from the RE.[107] This applies to the 2×4 and 2×7 surface as well as the NWs and allows any differences in the surface electronic structure between them to be investigated.

Previous MDS investigations of $RESi_{2-x}$ on Si(001) have been limited to 1 ML coverage of RE metal and greater, with no investigations of the sub-ML regime where the reconstructions dominate.[107,108] STM investigations have been conducted on the reconstructed areas, however, the technique is incapable of identifying particular surface atoms. This study investigates these low coverages with the intention of determining the initial formation conditions of $HoSi_{2-x}$ NWs on the Si(001) surface, as well as providing evidence as to the identification of atoms in the reconstructions through the combined techniques of STM, MDS and LEED.

4.2 Experiment

Experiments were conducted either in the MDS analysis chamber detailed in Chapter 3 or within an Omicron Nanotechnology GmbH STM which is equipped with LEED and a sample preparation chamber. This system has an operating pressure of $\sim 2 \times 10^{-10}$ mbar. In both cases, samples were prepared *in situ*. Initially, fresh n-type, high-ρ Si(001) substrates were flashed several times with dc heating for 1 min at 1200 °C which was then reduced to 900 °C for 10 mins followed by a slow cool (reduced at < 100 °C min^{-1}) to room temperature. All temperatures were measured using an infrared pyrometer. The LEED pattern was then checked to ensure a sharp 2×1 pattern to indicate a clean, well-reconstructed surface. The substrate temperature was then raised to between 500 and 650 °C while Ho was deposited. This is the temperature range that has previously been shown to promote surface order.[108] Holmium deposition was achieved by dc heating of a Ta boat containing a Ho ingot inside a Cu shroud with water cooling. Deposition rates were calibrated using a quartz crystal oscillator and were maintained at less that 0.1 ML per minute.

In the STM, coverages of 0.3 - 0.5 ML of Ho were investigated, whilst in the MDS chamber, coverages of 0.1 - 1.0 ML of Ho were investigated (where all coverages quoted are nominal). In all cases, the samples were allowed to cool down to room temperature before LEED, STM or MDS were conducted.

4.3 Results

The LEED patterns obtained in the MDS system, as the Ho coverage increases are provided for reference in figure 4.4.

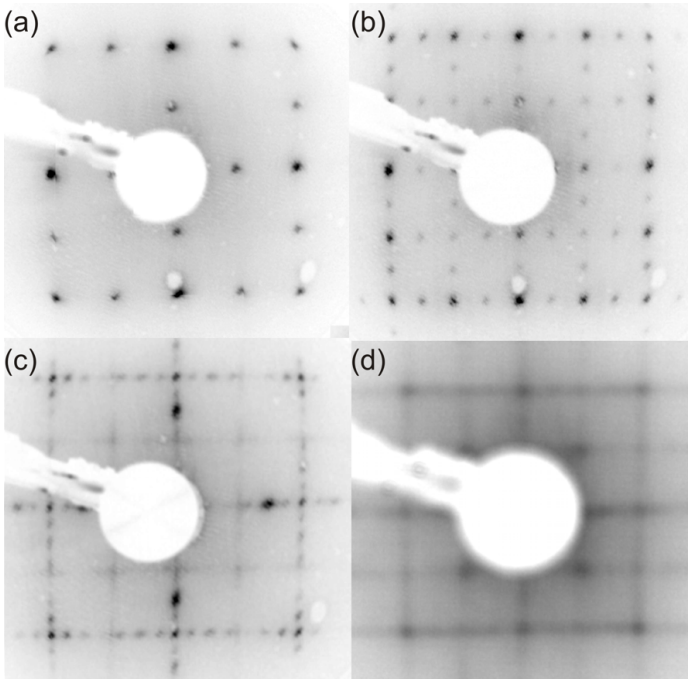

Figure 4.4: LEED images for various surface reconstructions acquired in the MDS chamber. (a) 2×1 Si(001) surface, (b) 2×4 after 0.3 ML Ho deposition, (c) 2×7 with a small trace of 2×4 after 0.5 ML Ho and (d) diffuse pattern with a trace of $c(2 \times 2)$.

Figure 4.5 is an STM image of the clean Si(001) 2×1 surface.[109] Terraces are visible on the surface and the step edges that bound them are fairly uniform. The dimer rows are noticeable, alternating their orientation on adjacent terraces. Defects within the dimer rows are apparent. Analysis over a large area revealed that the average distance between adjacent steps was ~ 30 nm.

The STM image in figure 4.6 is of a 0.3 ML coverage of Ho deposited onto Si(001) at 530 °C. Nanowires of two different, perpendicular orientations are apparent. Although NWs only grow along a single crystal direction, steps exist on the substrate surface which are visible in the figure. These steps are generally one Si atom high, and the orientation of each surface plane is perpendicular to the one below, as can be seen from the dimer orientation in figure 4.5. This leads to NWs forming perpendicularly to one another on alternate steps. Ragan *et al.* have shown that it is possible to use vicinal Si(001) off-cut by 2.5° towards the [110] direction, so that only double steps occur, which results in NW

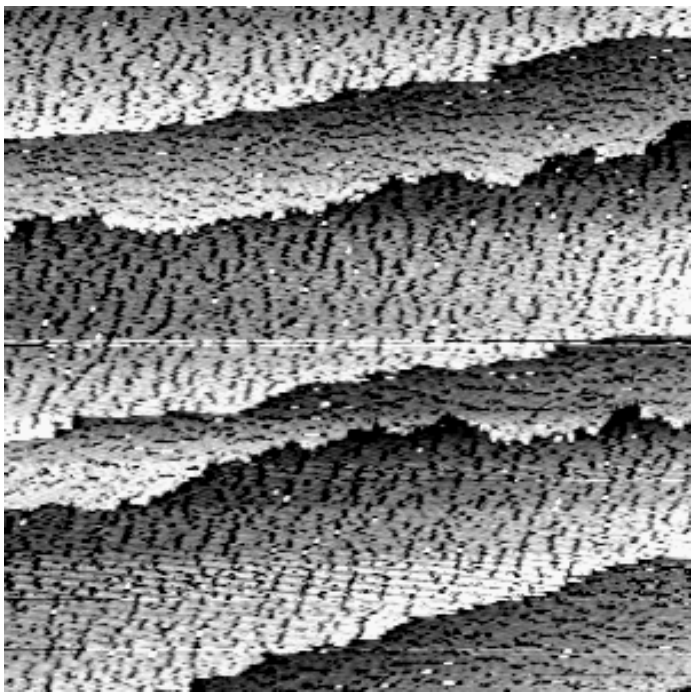

Figure 4.5: STM image of a stepped Si(001) 2×1 surface prepared by flashing. Dimer rows are visible across the surface (150×150 nm^2, -2.0 V and 2.0 nA).

growth in one direction only.[95]

It is apparent that the NWs originate at the top edge of a terrace, where the terrace edge seems to extend around the NW, forming a promontory onto the step below. It has previously been suggested that it is more favourable for a deposited RE atom to react with Si from step edges which have a lower number of Si-Si bonds, than those in the centre of a reconstruction.[81,110] This results in the terraces receding to provide Si for NW growth, leaving outcrops around the already initiated NW.[81] It appears that NW termination occurs either when a perpendicular NW is intersected, or, to a lesser extent, when reaching a terrace which is too high to dissociate. The average length of the NWs is determined by the density of NWs and the number of steps present on the surface.

The surface unit mesh of the Si substrate is 3.845 Å and the most common width of the NWs in figure 4.6 is 5.3 nm. This equates to approximately 14 Ho atoms across, which corroborates closely with the lattice mismatch perpendicular to the NW length of 6.8 %, which prevents the NW growing wider (slightly less than 50 % of the lattice constant in either direction).

Figure 4.7 shows the NWs in more detail. The reconstruction between the NW is also visible. These NW seem to grow in pairs, and a profile of such a pair is provided in the

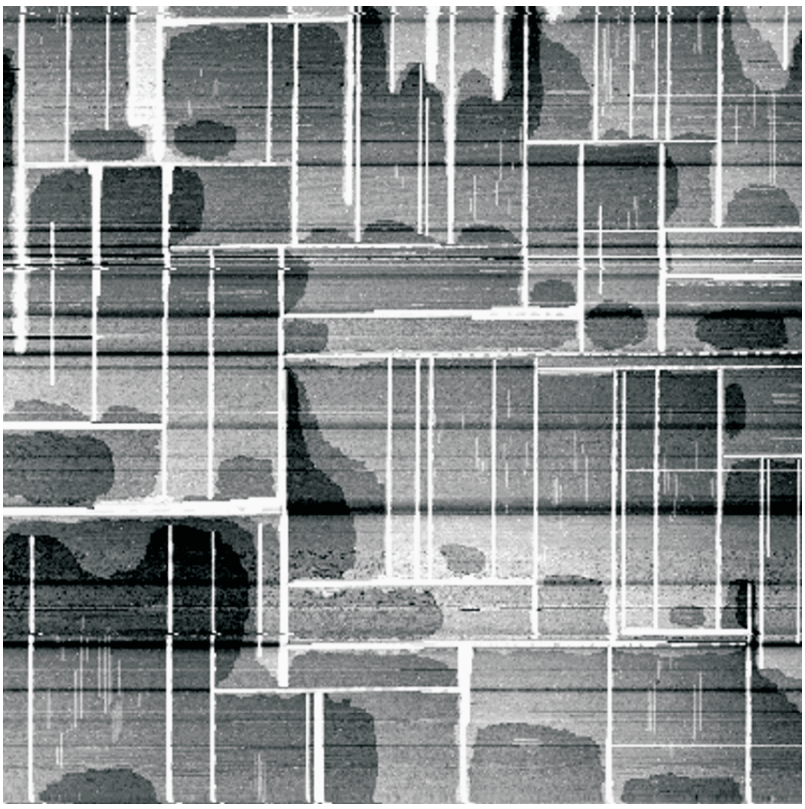

Figure 4.6: STM image of $HoSi_{2-x}$ NWs on Si(001) over a large area of the surface. 0.3 ML of Ho was deposited on Si(001) held at 530 °C (700 × 700 nm^2, 2.0 V and 2 nA).

inset. NW bundles have previously been reported, where a gap exists between the NW to relieve stress.[110] The profile also suggests that another layer of growth has occurred on top of the original NW. LEED images suggest a predominantly 2×4 reconstruction. A detailed view of this reconstruction in between the NWs in figure 4.7 is presented in figure 4.8.

Silicon dimers rows (which grow along the $[1\bar{1}0]$ direction, perpendicular to the NWs, are apparent as the bright features on a large proportion of the surface amongst the reconstructed areas. According to Liu and Nogami,[111] there are in fact two different sub-units that contribute to the 2×4 reconstruction. The models proposed are illustrated in figure 4.9.

Both sub-units generally occur alternately along the surface in the direction of the dimer rows and are separated by a Si dimer vacancy, although occasionally this vacancy may be absent. In the case of the type I sub-unit, there are two bright maxima surrounding a dimmer one; and in the case of the type II sub-unit, two dim features surround a brighter one, both of which are highlighted in figure 4.8. There is no necessary alternation between

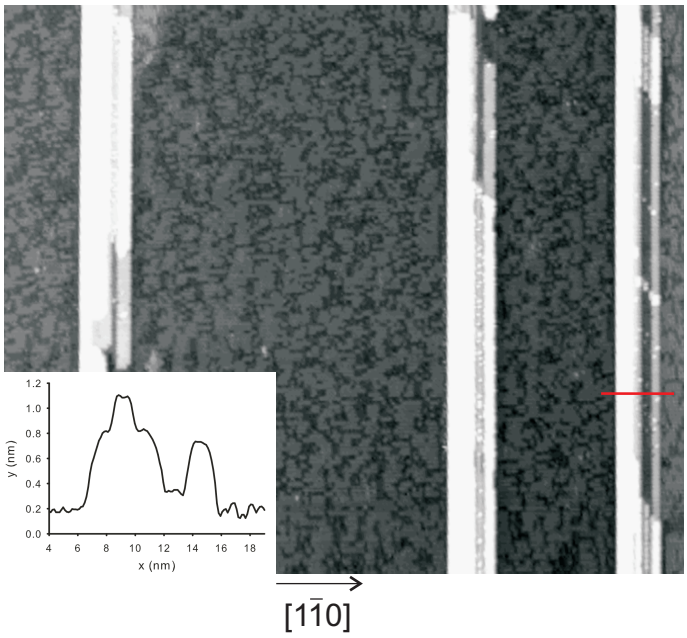

Figure 4.7: A more detailed STM image of the NWs and the reconstruction that exists alongside them. This surface formed after 0.3 ML of Ho deposition on Si(001) held at 610 °C (75×75 nm^2, -2.0 V, 2.0 nA). The inset shows a height profile of the NW at the line marked in red on the STM image.

the sub-units perpendicular to the dimer direction, however, this does seem preferable. Any such alternation would register as a translation by $4a$, as illustrated in the dimer column at the top of figure 4.9. Liu has hypothesised that vacancies within the silicide might induce vertical shifts in the surface atomic positions and cause buckling in a similar way to $RESi_{2-x}$ on Si(111). Such a buckling could result in the alternating STM intensities witnessed.[111]

If the reconstruction was perfect and no dimers remained, this surface would have a 2×8 periodicity, however, because the alternation in sub-units is not strictly adhered to, only a 2×4 LEED pattern is witnessed. This reconstruction is referred to as 2×4 in previous literature, and this nomenclature will be adhered to throughout this thesis to limit confusion. Both types of sub-units are visible on the reconstructed $HoSi_{2-x}$ substrate.

The formation of surface reconstructions as opposed to NW growth can be encouraged to form on the surface by reducing the substrate temperature from 600 °C, the optimum temperature for NW formation. This limits the mobility of the Ho atoms, thus preventing them from moving to areas of NW expansion. Reducing the temperature to 550 °C has yielded the surface imaged in figure 4.10. Again, 0.3 ML of Ho has been deposited onto the surface.

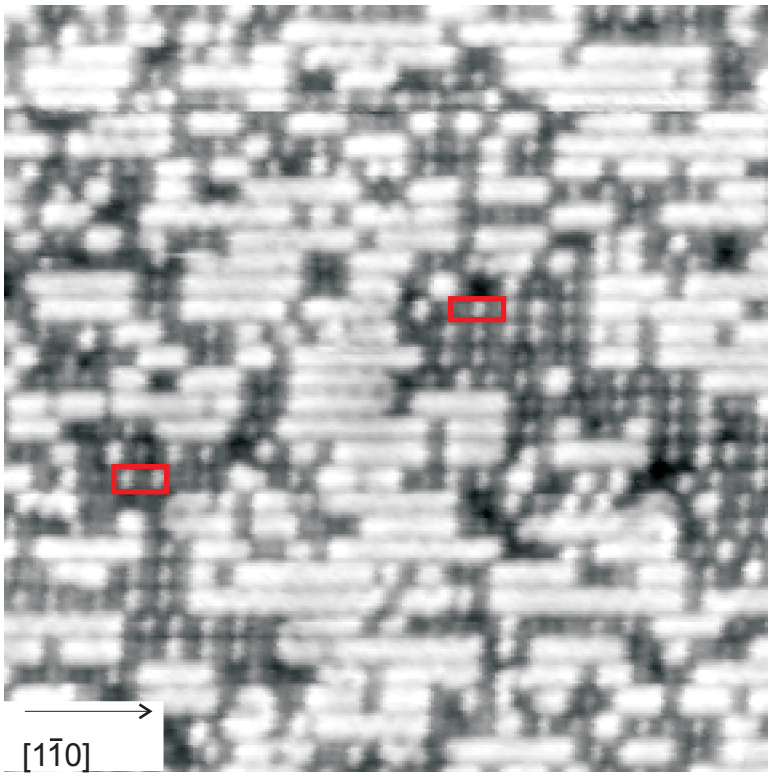

Figure 4.8: STM image for deposition at 610 °C showing a region of intermixed 2 × 4 silicide reconstruction and Si dimers. The 2 × 4 type I and type II features are indicated (32 × 32 nm^2, 2.0 V, 2.0 nA).

The part of the surface imaged in figure 4.10 contains no NWs and is heavily stepped. The bright lines across the entire surface are indicative of the 2 × 7 reconstruction, not previously recorded below coverages of 0.4 ML.[99] A more detailed image of this reconstruction for both the filled and empty states is presented in figure 4.11.

These particular images are of a step edge, with a NW on either side. In the filled state image, a repeating pattern of wide, bright maxima are apparent surrounding three, less intense features of which the central one is slightly brighter. This corresponds to the type I feature of the 2×4. A small shift in the unit cell by $1a$ is also apparent in some cases. This is also indicated on the filled state image, along with the 2 × 7 unit cell. The translation in the unit cell by $1a$ introduces antiphase disorder in the LEED pattern as can by seen in figure 4.4. The less intense features in the filled state image appear to be the brighter ones in the empty state image.

Ohbuchi and Nogami have previously proposed a model from STM empty and filled state observations which incorporates the shift in the unit cell.[99] This is illustrated in figure 4.12. It is suggested that the wider features observed in our STM image consist of two

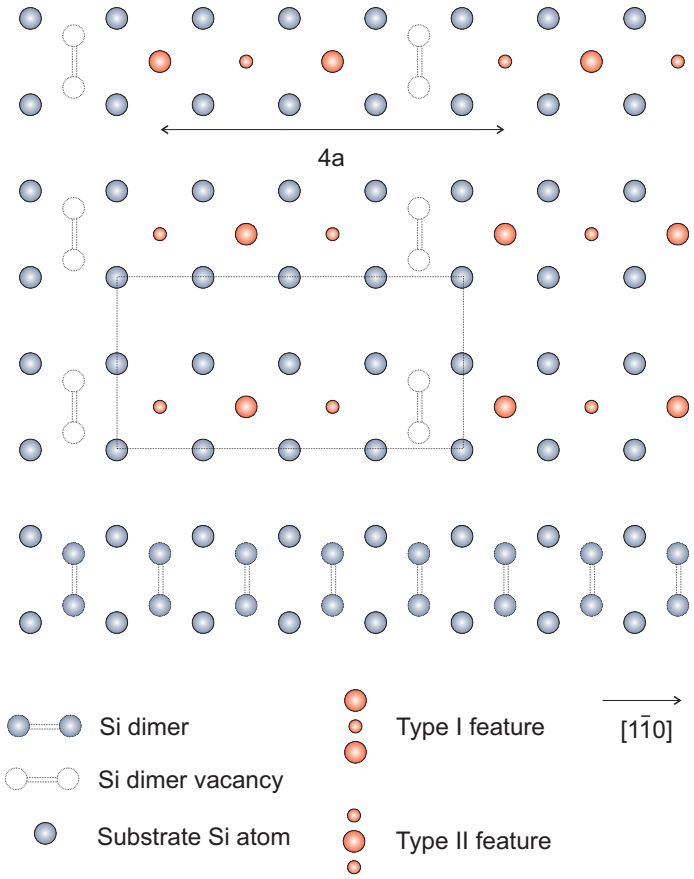

Figure 4.9: The features that constitute the 2 × 4 reconstruction.[111] A 2 × 4 unit cell is indicated. The top dimer vacancy row has been shifted by $4a$. A dimer row has been included to provide a reference guide.

separate atoms. A complete atomic structure has not been proposed, as evidence as to which atoms correspond to which features is lacking.

4.3.1 UPS

Figure 4.13 shows the He I UPS spectra for several coverages of Ho on the Si(001) surface obtained at normal emission. UPS was conducted in the same chamber as MDS, prior to performing MDS on the samples. The spectra shown are averaged over five scans.

The clean Si(001) spectrum demonstrates a peak at approximately 0.7 eV which can be attributed to the Si surface dimer state.[107] The main peak located around 6 eV is due to emission from the bulk $3p$ states. After 0.5 ML of Ho had been deposited and the sample annealed to form the silicide, there is no evidence of the surface state, which suggests that the majority of the dimers have been dissociated. The main peak remains at a very similar energy to the clean surface, but is now more intense, possibly due to a contribution from

Figure 4.10: STM image of terraces of the Ho 2×7 reconstruction on Si(001). Deposition of 0.3 ML of Ho was conducted at 550 °C. (50×20 nm^2, -2.0 V, 2.0 nA).

4*f* electrons. The emission of these states from the RE atoms extends over a wide energy range of the valence band thought to be between 5 and 10 eV for $ErSi_2$.[107] A small shoulder is evident at approximately 1.5 eV. This is at an energy where we might expect emission from the Ho 6*s*5*d* band, but since this feature does not occur for higher Ho coverages, it might be a feature of the particular reconstruction. Even for the very high coverages of Ho, very little changes in the spectrum, and no high energy surface features become apparent.

4.3.2 MDS

Samples were prepared *in situ* in the MDS experimental chamber under the same conditions as for STM. During Ho deposition, the substrate was held at 500 °C for all samples to encourage growth of the reconstructed surface as opposed to NW growth, before being allowed to cool down to room temperature. LEED was conducted prior to MDS to verify the quality of the surface. Each presented spectrum is averaged over sixteen scans.

The progression of the MDS spectra with increasing surface coverage is presented in figure 4.14. The spectrum from clean Si(001) is provided for comparison. The spectrum for Si(001) suggests from its smooth appearance with a lack of distinct features and gradual high energy cut-off that the de-excitation process for the 2^3S He atoms is RI+AN. This is where an electron from the He 2*s* level tunnels into an empty state in the surface. The ion that remains continues to approach the surface until at some point, an electron from the surface tunnels into the vacancy in the 1*s* state, simultaneously liberating an electron from the surface DOS. This is the de-excitation process that is characteristic of a narrow band-gap semiconductor. If AD was dominant on the surface, we would expect a sharp,

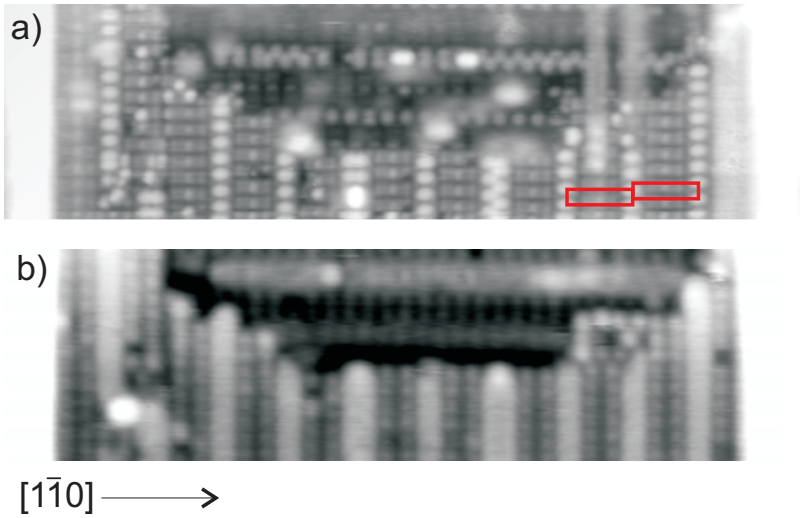

Figure 4.11: STM images of the 2 × 7 reconstruction for a 0.3 ML deposition at 550 °C. a) shows the filled state image with the red rectangles indicating the 2 × 7 unit cells and the shift between the two. (-2.0 V, 2.0 nA) b) shows the empty state image (2.0 V, 2.0 nA). Both images show the same area measuring 29 × 12 nm.

high-energy feature to arise from the Si dimer dangling bonds similar to that observed in UPS. With RI+AN, this feature would merge in with the bulk states which would explain the featureless appearance of the spectrum. A previous MDS study of Si(001) by Masuda *et al.* has concluded that the de-excitation mechanism for this surface is RI+AN.[45] They witnessed a high energy cut-off of 13.0 eV; this is comparable to our measured value of (13.1 ± 0.1) eV. If we take the work-function of the surface to be 4.87 eV,[112] this suggests a value for E_i' of approximately 22.9 eV compared to the gas phase value of 24.6 eV. This reduction is caused by the interaction with the surface through the image force.

The main peak labelled *A*, at approximately 8.7 eV for the Si(001) surface is thought

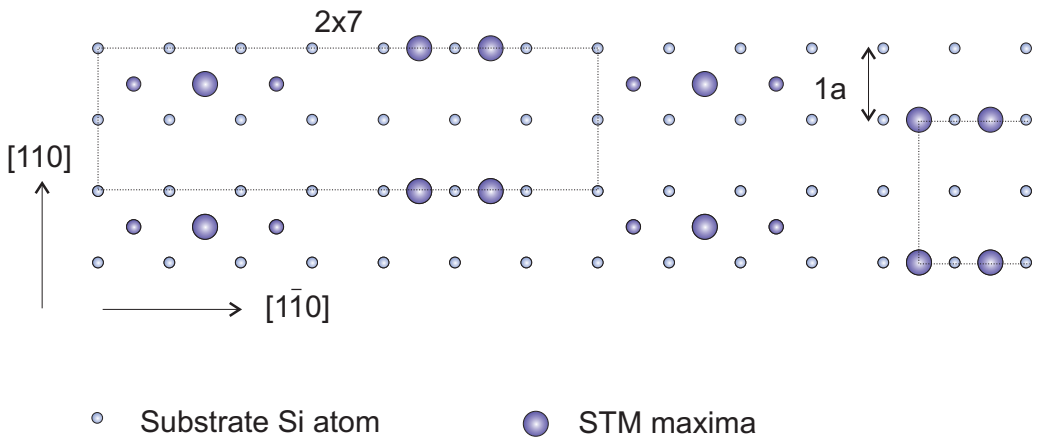

Figure 4.12: The 2 × 7 reconstruction of $HoSi_{2-x}$ on Si(001).[99,23] The unit cell and the $1a$ antiphase shift is marked.

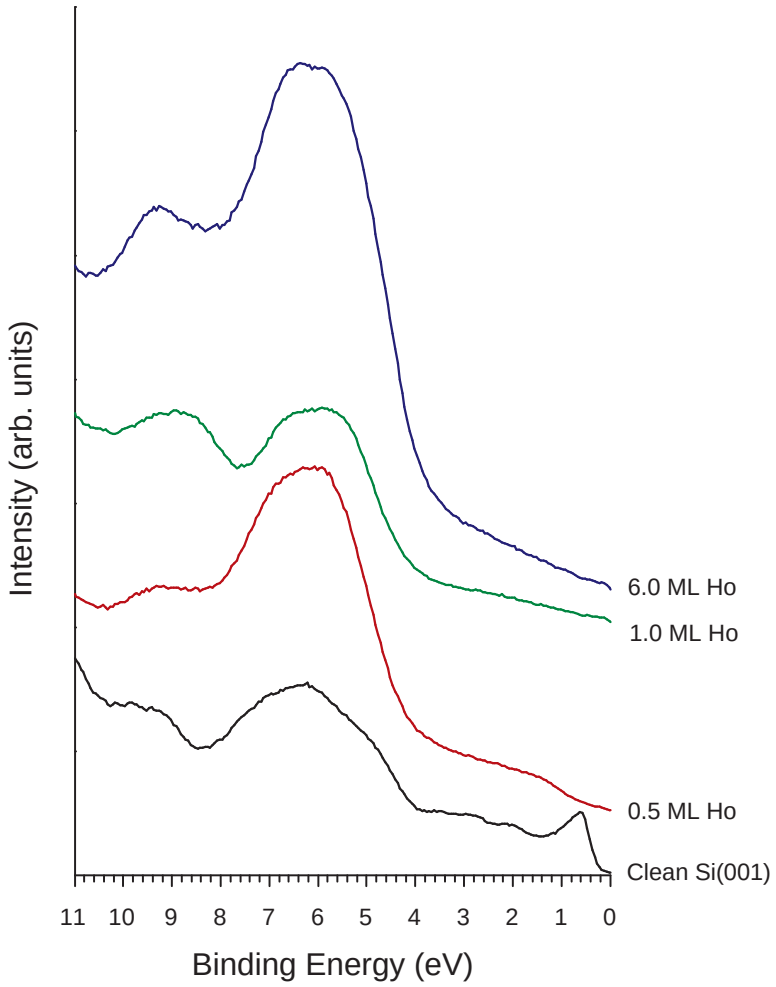

Figure 4.13: He I UPS spectra at the Γ point for various coverages of Ho on Si(001). Spectra have been offset for clarity.

to arise from the 3*p* states of Si. These arise both in the bulk and in the surface and are also observed in the Si(111) spectrum (see Chapter 5).[70] At energies below peak *A*, secondary electrons start to dominate the spectrum.

For the 0.1 ML spectrum, the 3*p* peak has shifted very slightly from the clean Si(001) position, and is also much narrower. There is now a distinct high energy cut-off superimposed on the gradual decline in intensity. This suggests that either some significant AD is occurring on the surface, or that this is from UV photoemission from the small number of photons remaining in the beam. As the coverage is still very low, we must assume that much of the Si(001) 2 $\times$ 1 surface remains as the STM images suggest, and so RI+AN will still be significant. Any change in the de-excitation mechanism is indicative of a modification to the surface work-function. Between 12 and 14 eV a small shoulder is starting

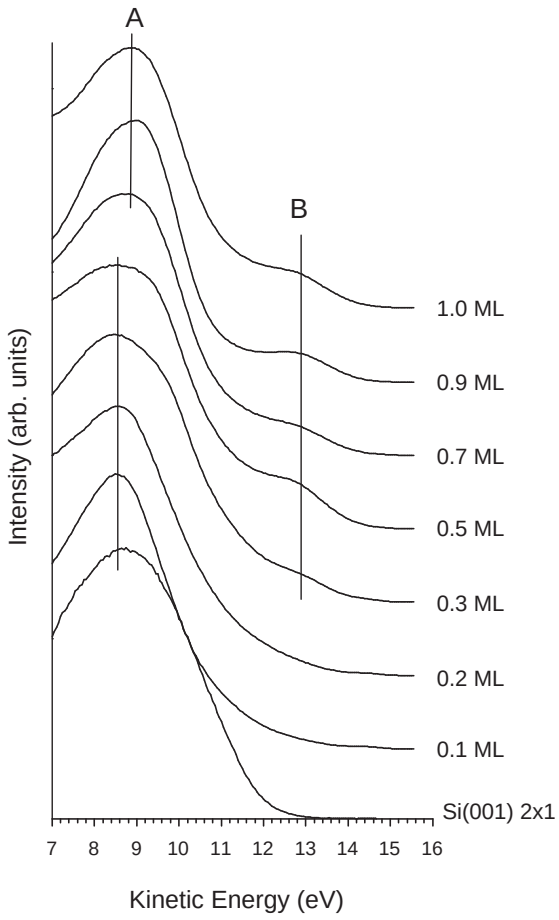

Figure 4.14: A comparison of MDS spectra for various Ho coverages deposited on Si(001) held at 500 °C. Particular features of the spectra are indicated and discussed in the text. Spectra have been offset for clarity.

to form.

The 0.2 ML spectrum is very similar to the previous one, however now, the LEED pattern is a combination of 2 $\times$ 1 from the Si(001) surface and 2 $\times$ 4 from the Ho induced reconstructed surface. As the coverage increases to 0.3 ML, the LEED pattern is predominantly 2 $\times$ 4. A shoulder starts to appear on the main peak at approximately 9.7 eV. Emission has also increased between 12 and 14 eV. This indicates that the surface is continuing to develop with the deposition of Ho. Emission at high energies continues to increase, indicating that AD is becoming more prevalent.

As the coverage is increased yet further, the peak at *A* increases in energy as the LEED pattern evolves from predominantly 2 $\times$ 4 to predominantly 2 $\times$ 7. This could well be due to a modification of the surface 3*p* states. A Si core-level shift has previously been

observed of the 3*p* states in the valence band through photoemission when 0.6 ML of Er was deposited onto Si(001).[100] This altered the band position by 0.3 eV, which is similar to the shift observed in figure 4.14.

The feature labelled *B* increases in magnitude. This is thought to arise from the hybridised Si 3*s*3*p* states and hybridised Ho 6*s*5*d* states in the silicide.[100,113] Previous studies have shown how this evolves with >1 ML coverage.[108]

At 1 ML coverage, the LEED pattern is unclear but suggests some presence of $c(2 \times 2)$, indicating that NWs are now contributing significantly to the surface reconstruction.

It is now possible to estimate a value of E_i' for the He 2^3S 2*s* level, as AD is now the dominant de-excitation channel. The kinetic energy maximum for the 0.5 ML spectrum is 15.25 eV. Combined with the sample work-function, this gives a value for E_i' of 19.70 eV, compared to the gas phase value of 19.82 eV, which shows that the image force is much less significant than in AN which produces a relatively large deviation in values of E_i'.[70]

4.3.3 Substrate Temperature Effects

A sample of 0.7 ML Ho coverage was prepared holding the substrate initially at 500 °C during deposition before being allowed to cool to room temperature before LEED and MDS were conducted. The sample was then annealed to 550 °C and subsequently 600 °C for 5 mins and allowed to cool. MDS and LEED were again conducted after each anneal and cool so that the effects of temperature on the spectrum could be investigated. The resulting MDS spectra are provided in figure 4.15.

The LEED pattern for the 500 °C spectrum indicates a 2 $\times$ 7 reconstruction as would be expected at this coverage. The MDS spectrum demonstrates a large shoulder at *B*. When the substrate is annealed at 550 °C, the feature labelled *B* decreases slightly in intensity and the LEED pattern demonstrates mainly 2 $\times$ 4 periodicity which suggests a modification to the reconstruction of the surface. After annealing at 600 °C, the feature located at *B* is no longer apparent, and the LEED indicates a reversal back to a 2 $\times$ 1 surface reconstruction, however the MDS peak at *A* remains much narrower than for the previous Si(001) 2 $\times$ 1 surface. Emission at high kinetic energy is reduced, and it is thought that RI+AN is again the dominant de-excitation mechanism. Further investigations of lower coverages suggest that the 2 $\times$ 1 reconstruction may always be recovered as the Si substrate is re-exposed as

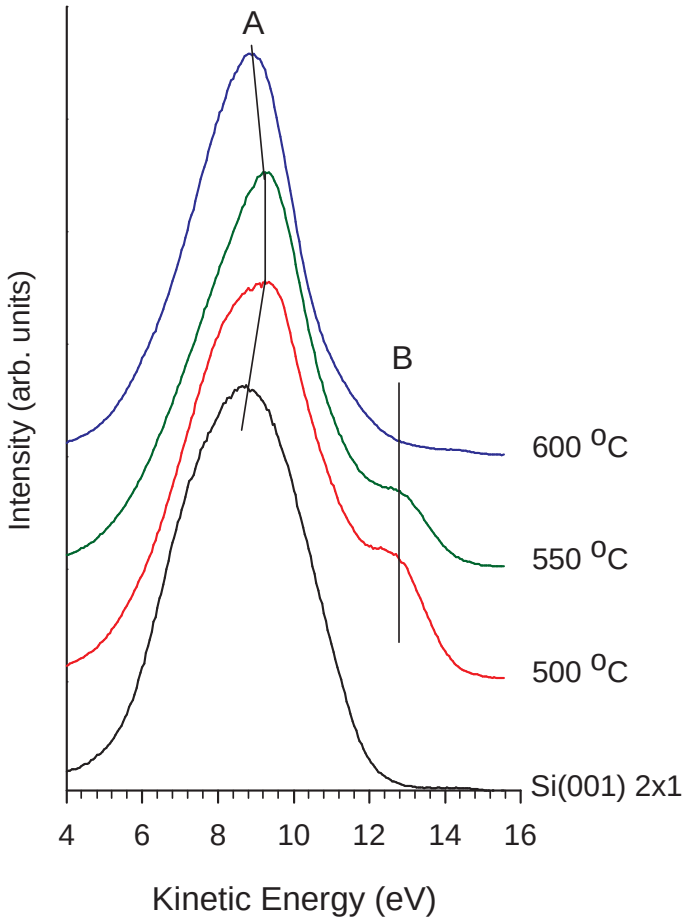

Figure 4.15: Evolution of MDS spectra for 0.7 ML Ho with increasing temperature. Spectra have been normalised for direct comparison and offset for clarity. The Si(001) spectrum has been provided for reference.

nanostructures form, and for lower coverages, the anneal time required for the recovery is reduced.

4.4 Discussion

A combination of STM, MDS and LEED suggests that at the lowest coverages of Ho (<0.3 ML), some of the Si(001) 2 × 1 dimerised surface is still exposed alongside the 2 × 4 reconstruction and as such the de-excitation mechanism for MDS is RI+AN. Between 0.3 and 0.5 ML, little 2 × 1 remains, with the majority of the surface assuming a 2 × 4 or 2 × 7 reconstruction (which one is prevalent depends on a combination of substrate

temperature during deposition and the amount of RE deposited). Here the work-function has decreased to the extent that AD is now the dominant de-excitation channel in MDS. As the coverage of RE is increased, the hybridised Si 3*s*3*p* and Ho 6*s*5*d* play an increasing role in the surface electronic structure. At even greater coverages, the contribution by NW to the surface reconstruction increases, competing with the remaining 2×7 reconstruction. Even approaching 1 ML of Ho deposition, some 2×7 is evident in the LEED image. Again, the density of NWs present on the surface is dependent on both the Ho coverage and the sample temperature, which alters the Ho mobility. Thus a higher temperature promotes NW formation and increases the coverage at which the 2×7 reconstruction starts to dominate over the 2×4. Figure 4.15 suggests that as the temperature is increased and the Ho atoms gain greater mobility, they may achieve sufficient energy to relocate from the 2×4 and 2×7 reconstructions to form nanostructures.

For the 2×4 reconstruction, it has previously been suggested that the maxima observed with STM are due to single RE atoms that have replaced the Si dimers.[111] In this case, as there are 3 maxima per 2×4 unit cell, the RE coverage would be 3/8 or 0.375 ML, which broadly agrees with the nominal coverage where the reconstruction is most complete. For the 2×7 reconstruction, if again each of the maxima in the STM image are the result of a RE atom, the optimum, nominal RE coverage would be 0.357 ML, which again agrees with observations.[23] Ohbuchi and Nogami, in a study of Ho on Si(001), have suggested that for the 2×4 reconstruction, only one type of the two maxima are caused by a Ho atom.[99] This would lead to an average Ho content of 1.5 atoms per unit cell, or 0.188 ML nominal coverage. It is somewhat surprising that all the maxima in the 2×4 reconstruction are due to RE atoms, as the reconstruction occurs at lower Ho coverages than the 2×7, as it contains a greater number of RE atoms per unit cell making this model unlikely.

When 1 ML of Ho is deposited on the Si(111) 7×7 surface when held at an elevated temperature, due to the low lattice mismatch between the $HoSi_2$ and the substrate in both perpendicular lattice directions across the surface, a 2D silicide film forms with 1×1 periodicity (see Chapter 5). This consists of a reverse buckled Si bi-layer surmounting a sub-surface Ho layer.[114] Figure 4.16 shows for comparison an MDS spectrum from both a $HoSi_{2-x}$ on Si(111) and on Si(001).

The $HoSi_{2-x}$ on Si(111) spectrum is characteristic of RI+AN, consisting of a wide peak, with no other features apparent. Its shape is very different to the spectrum from

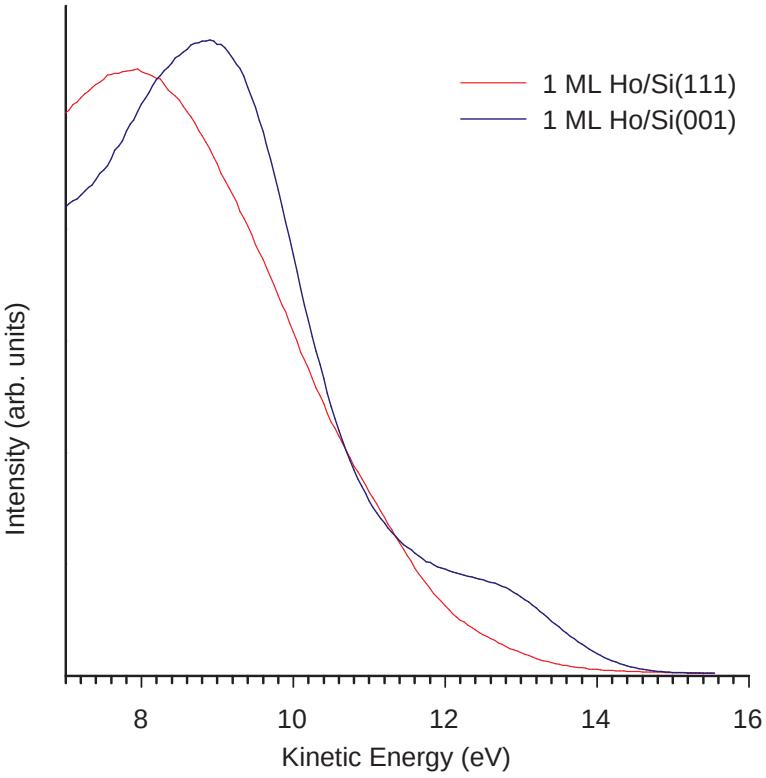

Figure 4.16: MDS spectrum comparison of 1 ML of Ho deposited onto Si(100) and Si(111) at 500 °C

the $HoSi_{2-x}$ on Si(001) spectrum, with its narrower peak, and high-energy shoulder. The differences between the spectra suggest that a Si bilayer does not form on the Si(001) sample as it does on the Si(111) sample. This implies that the contribution from pure Si states on the surface is minimal. This supports the models where at least some of the maxima in the STM image are due to RE atoms. It does not however, inform us as to whether any of the maxima are also due to Si atoms.

Figure 4.17 shows the MDS spectrum for 6 ML of Ho deposited onto Si(001) at room temperature compared to that of 0.3 ML of Ho at 500 °C.

The feature labelled *C* in the 6 ML spectrum, just below E_F has previously been attributed to Ho 6*s*5*d* states.[108] This indicates that the deposited Ho reaction with the substrate has been very limited. When the substrate has been heated during deposition, these 6*s*5*d* states bond to the Si 3*s*3*p* hybridised states by transferring charge from the Ho to the Si creating a surface dipole and resulting in the feature labelled *B*.[35] The dramatic difference between the two cases indicates that no significant amount of unreacted RE exists on

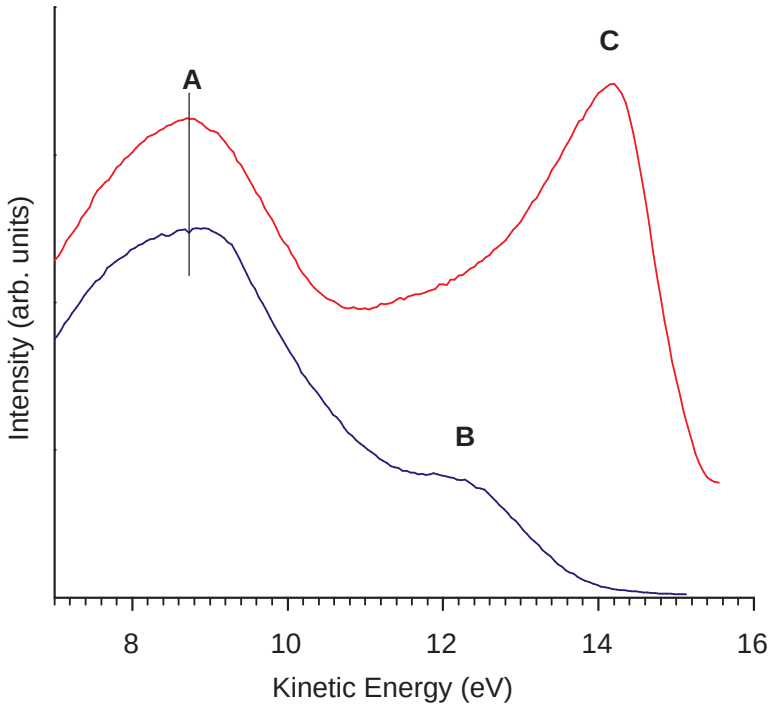

Figure 4.17: The MDS spectra for 6 ML Ho deposited onto Si(001) at room temperature (red line) and 0.3 ML Ho deposited on Si(001) at 500 °C (blue line). The spectra have been normalised and offset for clarity.

the surface, either as a nanostructure, in the reconstruction, or as any other feature.

The evolution of the MDS spectra with increasing Ho coverage illustrates the gradual development of the hybridised Ho 6*s*5*p* and Si 3*s*3*p* states in the sub-monolayer regime. These states have previously been observed for much higher RE coverages where nanostructures are dominant. Their presence in the reconstructed surface suggests that the reconstructions do form as a precursor to nanostructure growth.

The investigation of substrate temperature for a 0.3 ML coverage shows a preference for the 2×7 reconstruction at 500 °C which progresses to the 2×4 reconstruction at 550 °C and then reverts to the 2×1 reconstruction at 600 °C where the surface behaves in a similar way to the clean Si(001). This transition between reconstructions implies that the Ho atoms are mobile at these temperatures. The progression of the surface with increasing temperature from a 2×7, the reconstruction witnessed at higher coverages, to a 2×4, the reconstruction witnessed predominantly at lower coverages, indicates that heating reduces the Ho within the reconstruction and so the Ho must be relocating to the NWs.

Although other REs demonstrate the same reconstructions, the depositions that lead

to the maximum coverage of a particular reconstruction do vary between the RE metals suggesting that chemical identities do still play an important role.[23]

The STM images indicate that the sub-units in both the reconstructions consist of three alternating maxima along the $[1\bar{1}0]$ direction. However, the actual positions of these sub-units within the unit cell vary.

4.5 Conclusions

The structural and electronic properties of sub-monolayer coverages of Ho on Si(001) have been investigated for the first time using MDS. STM, LEED and UPS have also been conducted, and the combined techniques used to provide support for previously proposed models of the 2×4 and 2×7 reconstructions. Evidence indicates that the two reconstructions share some similar structural and electronic characteristics and that at least some of the STM maxima within the unit cells are due to Ho atoms, however it is not known if all are, and additional techniques or theoretical calculations would be needed to support any particular hypothesis further.

Studies of temperature and coverage suggest that Si atoms migrate from step edges to form the reconstructions, and increasing the temperature of the substrate during or after deposition increases the mobility of the Ho atoms, allowing them to relocate from the reconstructions to form nanostructures such as NWs. It has also been shown that the 2×4 reconstruction is preferable to the 2×7 at lower coverages ($\lesssim$0.3 ML), however, lower temperature annealing promotes growth of the 2×7 reconstruction.

A comparison of UPS and MDS spectra demonstrates how much more sensitive MDS is to surface states than UPS, with no contribution from the core-like 4*f* states.

Chapter 5

Rare Earth Silicide on Si(111)

5.1 Introduction

This chapter focuses on the electronic structure of Ho silicide on the Si(111) surface and that of the hydrogen terminated Ho silicide surface. An overview of the reactions that occur between RE metals and silicon that lead to the formation of RE silicides is provided in the introduction to Chapter 4.

5.1.1 The Ultra-thin Rare Earth Silicide

The Ho silicide on Si(111) system is particularly important, as it forms continuous films on Si(111) due to the low lattice mismatch across the surface. This results in a high quality continuous interface with future potential in electronics applications.

Much experimental research has been conducted on the RE silicides on Si(111) using a variety of techniques such as LEED,[115,116] medium energy ion scattering (MEIS),[17,117] STM,[118,119] and UPS.[19] These techniques have revealed that trivalent REs (such as Dy, Ho and Er) all form very similar RE silicides with common electronic properties. They have also lead to the development of detailed structural models as described later.

When 1 ML of trivalent RE is deposited on clean Si(111) and then annealed at a sufficient temperature, a 2D silicide forms with a stoichiometry of 2 Si atoms per RE to give $RESi_{2-x}$ where $x = 0$ where the RE layer exists below a buckled Si bilayer. These Ho atoms reside in the T_4 sites of the Si(111). The buckling of the top bilayer is reversed with respect to the bulk Si (known as B-type buckling); this results in the maximum number of

nearest neighbour atoms for each RE atom and so stabilises the structure. The structure of 2D RE silicide on Si(111) is illustrated in figure 5.1 (a).

When more than 1 ML of trivalent RE is deposited in the same manner as before, a 3D silicide forms where flat RE layers exist with flat Si layers in between with a stoichiometry of $RESi_{2-x}$ on Si(111) where x ≈ 0.3 as shown in figure 5.1 (b). This reduction in the proportion of Si compared with the 2D silicide arises from the presence of vacancies within the flat Si layers as an ordered array, where every one in six of the Si atoms is vacant. The existence of these vacancies acts to relieve strain from the rest of the structure and gives rise to a $(\sqrt{3} \times \sqrt{3})R30^\circ$ LEED pattern. As with the 2D silicide, a buckled bilayer exists above the top-most RE layer, however this may display B-type, A-type, or a combination of A-type (where the buckling direction of the bilayer is the same as the bulk terminated surface) and B-type buckling.[17] It is thought that differences within the vacancy network may contribute to which type of bilayer orientation forms.

STM studies have shown $(\sqrt{3} \times \sqrt{3})R30^\circ$ modulations in the surface bilayer of the 3D reconstruction which have been suggested to arise due to the underlying vacancies, although the details are disputed and vacancy periodicities in the c-axis direction of $1c$, $2c$ and $3c$ have all been reported.[18,120,121,122]

Of the trivalent RE's three valence band electrons that are available for bonding, two bond with the dangling bonds of the Si atoms directly above and below the RE atom which forms a saturated, closed shell structure.[123] The third electron goes towards partially compensating an outwards pointing dangling bond arising from the top Si layer. This leads to a relatively passive surface with $p(1\times1)$ periodicity. The dangling bonds of the RE silicide are now doubly occupied. This makes the surface ideal for MDS as when the 2^3S He approaches the surface, one electron from the dangling bond may be used to neutralise the He^+ ion, leaving the other electron in the dangling bond to be emitted by the Auger process ensuring that the dangling bonds are detected.

Several theoretical studies have also been conducted on the RE silicide on Si(111) system, the first of which was by Stauffer *et al.*[123] The band structure of 2D $ErSi_2$ on Si(111) was determined using a semi-empirical technique for a variety of top layer orientations and bonding sites. This technique indicated that the reverse-buckled top layer gives the band structure obtained experimentally from ARUPS. This work was developed by Rogero *et al.*[124] using DFT to show a generic electronic structure for all trivalent RE silicides.

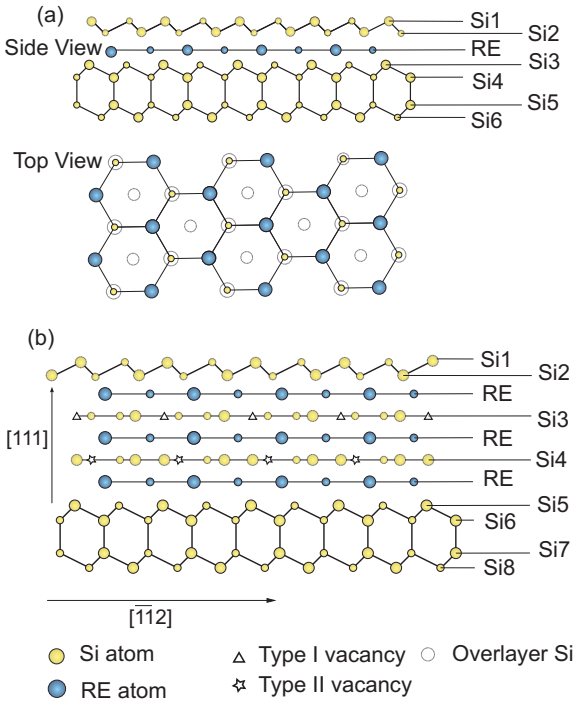

Figure 5.1: A structural model of B-type (a) buckled 2D and (b) 3D RE silicides. The individual layers within the structure are labelled.

A geometry optimised structure of the 2D YSi_2 on Si(111) calculated using DFT indicated that the structural parameters were comparable with those suggested by LEED. These parameters were then improved upon by Cocoletzi *et al.*[125] who also conducted the first simulations of a 3D silicide surface using DFT investigating possible vacancy locations within the graphitic Si layers.

Rogero *et al.* studied the effects of vacancies in the silicide on the buckled bi-layer and compared STM and simulated STM data to demonstrate that at least two different subsurface vacancy networks may exist in different domains within the same sample.[18]

The DFT calculations in this work focus on the Si bilayer; and although they have not been performed as a part of this thesis, they provide a necessary comparison to the deconvoluted MDS, allowing identification of individual features and more definitive conclusions.

5.1.2 Hydrogen Termination

Much research into the interactions between hydrogen and surfaces is currently being conducted due to the drive in developing hydrogen fuel cells and associated hydrogen

storage solutions for commercial use.[126,127] From a fundamental point of view, it is widely known that H also has significant effects on surface reconstructions. As such, it is of paramount importance to understand the reactions and dynamics involved.

Within this chapter, the effects of hydrogen termination on both the 2D and 3D $HoSi_{2-x}$ surface are studied, as drastic changes to the surface and electronic structure are thought to occur.

The most obvious question to ask upon H termination of a RE silicide is: where does the H bond to the structure? This was first addressed by Saintenoy *et al.* who suggested that for a 2D $ErSi_2$, one bonding site exists per unit cell on the buckled Si bilayer.[19] An additional site was thought to exist in the 3D $ErSi_{2-x}$ film where H is absorbed into the structure, and most likely passivates the internal dangling bond. It was also noted that the H could be desorbed at just 300 °C compared to 550 °C for the Si(111) 1×1 - H surface, and the clean silicide spectra could be recovered to some extent.

The following year, Angot *et al.* showed a transition from a semimetallic to a semiconducting state upon H termination of a 2D $ErSi_2$ and postulated that an individual H-Si bond could not entirely be responsible for this, and as such there must be an additional chemisorption site, however no direct evidence of this was provided.[128]

As the dangling bonds of the $RESi_2$ are already doubly occupied, it might seem strange that these react with monatomic H, as this would leave the dangling bond with an odd number of electrons. An additional H adsorption site would account for this as it provides an even number of valence electrons necessary under electron counting rules.[1,129]

Wetzel *et al.* provided evidence via high resolution electron energy loss spectroscopy (HREELS) and ARUPS of this second site as an H-Er bond and suggested it is most likely an interstitial site within the hexagonal Er monolayer.[129] Furthermore, it is suggested that occupation of both sites is concomitant rather than sequential as both sites are either occupied or empty for different doses of H on the $ErSi_2$ surface. Evidence presented also strongly suggests that the H that adheres to the surface bilayer bonds with the Si dangling bond.

In a subsequent paper, Wetzel *et al.* used Auger electron diffraction (AED) and LEED to demonstrate that upon H termination, the bilayer buckling reverses from B-type to A-type, and also that the spacing between the RE layer and buckled bilayer increases upon

termination by 0.32 Å.[20,130] This has subsequently been confirmed using LEED I/V,[131] and also appears to be the case on the Dy germanide on the Ge(111) surface.[132]

Figure 5.2 indicates the possible H-Si bond and the H-RE bond locations.

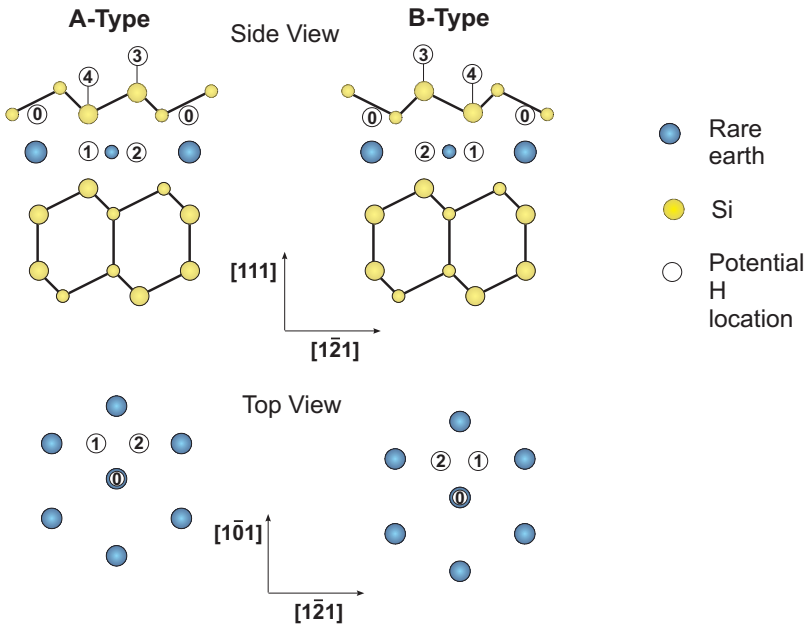

Figure 5.2: Possible chemisorption locations of H within the 2D RE silicide unit cell. Not all have been investigated within Sonnet's study.[133]

In line with experimental evidence, theoretical studies using the extended Hückel method have also suggested two chemisorption sites per unit cell for the 2D $ErSi_2$ are energetically favourable.[133] This again suggests that H bonds to an interstitial site within the RE layer. The calculations assume one H atom occupies the A_3 or B_3 site (where A or B refer to the termination type) and investigated sites A/B_{0-2}, which revealed that the A_2 site, as shown in figure 5.2, was the most energetically favourable one within the subsurface unit cell.

As it is known that the buckling direction switches on termination, and it has previously been suggested that occupation of the two sites is concomitant. Assuming that H always bonds to site 3 before and after termination seems to be at odds with evidence unless the H switches sites, for which no evidence is provided.[133] Also, this result may not prove entirely accurate as geometry optimisation was not performed on the structures which can lead to energy differences of up to 1 eV,[134] and only a limited number of possible hydrogenation sites were investigated.

Whilst much work has already been conducted on the H-termination of RE silicides,

it still remains unclear why buckling reversal occurs and what changes occur to the electronic and physical structure upon H-termination. Additionally, MDS has not previously been conducted on any H-terminated $RESi_{2-x}$ surface and the surface sensitivity of the technique should allow the delivery of valuable new information regarding the H bonding.

5.2 Experimental

5.2.1 The Clean $HoSi_{2-x}$ Surface

All preparation and measurements were conducted within the same analysis chamber prior to the addition of the sample preparation chamber. At the time, it was equipped with LEED, UPS and MDS and had a typical base pressure of approximately 3×10^{-10} mbar.

Si(111) samples were cut from a lightly-doped, *n*-type wafer. These were outgassed for approximately 8 hours at 400 °C and subsequently cleaned by dc heating to approximately 1200 °C for one minute, as measured on an infrared pyrometer, before being allowed to cool to approximately 900 °C. This process was repeated at least three times and was followed by a gradual cool (< 100 °C per minute) to room temperature. The LEED pattern was checked to ensure sharp spots indicating the 7×7 reconstruction.

Holmium deposition was achieved by dc heating of a Ta boat containing a Ho ingot, and deposition rates were calibrated using a quartz crystal oscillator. During deposition, the chamber pressure did not rise above 5×10^{-10} mbar. The sample was held at room temperature during deposition and was subsequently annealed for 10 mins at approximately 500 °C to achieve the silicide structure. The coverages quoted in this chapter are nominal, and in reality the local film thicknesses may differ from these values due to islanding in some regions of the surface.

After preparation, LEED patterns were checked for all samples to ensure that a good surface reconstruction had been achieved. The 2D silicide surface exhibited a bright, three-fold, $p(1 \times 1)$ LEED pattern as would be expected. The 3D silicide surfaces all gave a $(\sqrt{3} \times \sqrt{3})R30°$ LEED pattern with the less common three-fold (as opposed to six-fold) rotational symmetry. A three-fold pattern suggests that the surface is well ordered so that the bilayer buckling is either all A-type or all B-type. A six-fold pattern would indicate an equal presence of both domains of buckling over the surface. This may well indicate a

long range ordering of the vacancy network in the flat Si layers, however, it is not known what prompts vacancies into assuming particular periodicities. The LEED pattern for the 2 ML coverage exhibits weak $(\sqrt{3} \times \sqrt{3})R30^\circ$ spots indicating that the surface probably consists of a combination of 2D silicide and 3D islands. In our case, for the 3D silicide, the orientation of the LEED spots was the same as for the 2D silicide which indicates a B-type buckled surface. In this study, 1, 2, 4 and 6 ML films were grown and investigated. MDS and UPS experiments were then conducted on the clean silicide surfaces.

5.2.2 The H Terminated $HoSi_{2-x}$ Surface

Once an experiment had been conducted on the clean silicide surface, the samples were then passivated with H. This was done by introducing $\sim 3.5 \times 10^{-6}$ mbar of H_2 into the system for 15 minutes, which was cracked to form monatomic H using a tungsten filament at a distance from the sample of approximately 50 mm, exposing the sample at close to room temperature. The LEED pattern was checked to confirm reversal of the intensity of the three-fold spots which indicates complete H termination. MDS and UPS were then conducted.

5.3 Results and Discussion

5.3.1 The Clean $HoSi_{2-x}$ Surface

The UPS spectra for surfaces of Si(111) with different coverages of Ho are presented in figure 5.3. Marked changes appear with increasing coverage, particularly between the 1, 2 and 4 ML silicide surfaces. The spectrum for clean Si(111) 7×7 is provided for reference.

UPS Results

The clean Si spectrum shows peaks characteristic of the 7×7 reconstruction surface states at -0.2 eV and -0.9 eV from dangling bonds and at -2.0 eV from back-bond states.[135,136] These peaks are suppressed after Ho silicide formation, as would be expected when a new surface reconstruction arises and the states are passivated by the free valence electrons of the Ho atoms. The hybridised Si 3*sp* peak at approximately 7.5 eV is also apparent in the

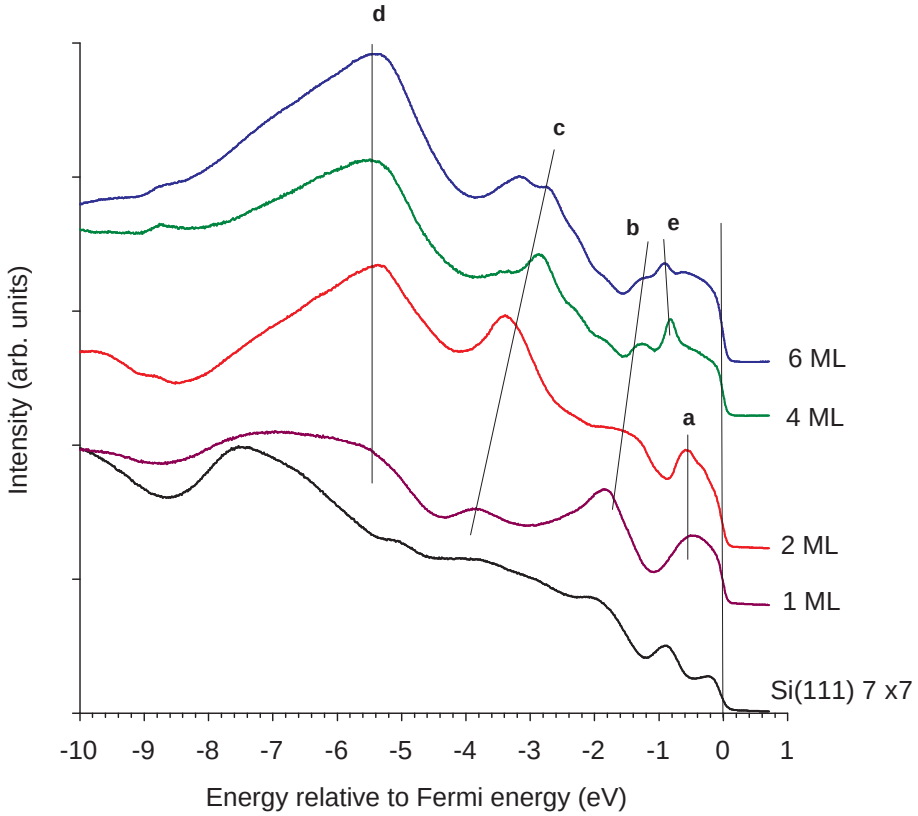

Figure 5.3: UPS spectra for various $HoSi_{2-x}$ coverages on Si(111). The Si(111) spectrum is provided for reference. The spectra are offset for clarity.

Si(111) 7×7 spectrum, which reduces slightly for 1 ML Ho coverage, and either reduces or shifts in energy for larger coverages.[137]

A previous UPS study has been conducted for 2D and 3D $ErSi_{2-x}$ which highlighted similar features to the ones presented in this chapter.[19] In the 1 ML spectrum, the peak labelled *a* is thought to be a superposition of two features: both a Si surface feature and a Ho feature. The surface feature previously noted by Saintenoy *et al.* at -0.1 eV relative to E_F has been explained as a Si surface state from p_z dangling bonds.[19] A large emission is also expected to arise from Ho 5*d* emission at E_F. The peak labelled *b* is thought to result from another surface state with p_z character derived from the dangling bonds of Si atoms.[123,20] It may also have some contribution from the Si back-bond state from any remaining, exposed Si(111). Feature *c* has been attributed to an electronic state from hybridised RE 5*d* and Si 3*p* electrons. With increased Ho coverage, this feature increases in intensity supporting this at least partial Ho origin. The much broader peak at *d* is due to the core-like RE 4*f* states and is not involved in the silicide bonding structure and would therefore not appear in the MDS spectrum.[19,20,138]

A slight change in the spectra for the 3D silicides is expected due to the presence of vacancies within the structure, slightly modifying the DOS. For the 3D silicides, some of the features, such as *c* and *d*, are similar to the 1 ML case, although some relocate slightly in energy as a result of changes in crystal potential. For the 2 ML coverage, the features are all at very similar energies to the 1 ML case. The feature labelled *b*, earlier attributed to a Si dangling bonds has decreased in intensity. As the coverage increases, the peak labelled *a* in the 2D case, splits into a shoulder and separate peak, labelled *e*, in the 3D case. The shoulder is likely due to the p_z electronic states mentioned previously. This peak at 0.9 eV is similar in energy to a feature noted by Saintenoy *et al.* resulting from $3p_z$ electrons in vacancies.[19] This would explain its absence from the 2D spectrum.

MDS Results

When MDS is performed on metallic, semi-metallic and narrow band-gap semiconducting surfaces such as the ones studied here, the de-excitation process that takes place is predominantly RI+AN. This is the case for the Si(111) surface. Initially, the 2^3S atoms are resonantly ionised, where the He 2*s* electrons tunnel into an empty surface state, thus leaving a He^+ ion which continues to approach the surface. Auger neutralisation follows, where a surface electron transfers into the He^+ ground state, simultaneously liberating another surface electron in an Auger-type transition. As RI+AN is a two-electron process, the bands in the SDOS are self-convoluted, and so the resulting spectra lack sharp features. For insulating surfaces and wide band-gap semiconductors, the de-excitation mechanism that occurs is AD. In this process, an electron tunnels from the surface to fill the 1*s* vacancy. The 2*s* electron is simultaneously liberated. In both these de-excitation processes, as the He 2^3S interacts with the orbitals furthest into the vacuum, the technique is extremely sensitive to the SDOS.

The MDS spectra acquired at room temperature are presented in figure 5.4 for the same coverages as for UPS. These spectra have been normalised to the maximum of the 4 ML spectrum so that relative intensities can be directly compared. As the maximum emission occurs at an energy where bulk states dominate, this should not unfairly bias the magnitude from the surface states.

The MDS spectrum for the clean Si(111) 7×7 surface displays three distinct features: a peak and two shoulders. The peak, centred at 8.5 eV is due to 3*p* electrons from the

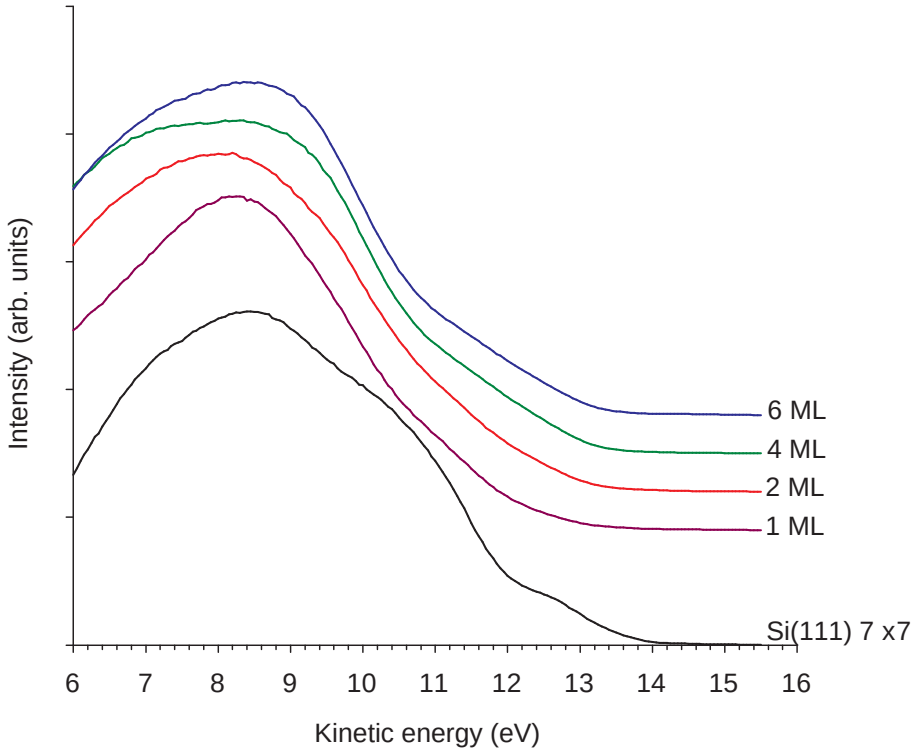

Figure 5.4: MDS spectra for various $HoSi_{2-x}$ coverages on Si(111). Spectra have been normalised and offset on the intensity axis for clarity. The Si(111) 7×7 spectrum has been included for reference.

bulk states.[70] The shoulder at around 10.3 eV has not previously been reported in MDS spectra, but a peak at approximately 3.0 eV below E_F in the SDOS has been predicted by tight-binding theory calculations arising from surface dimer states.[139] This corresponds to the energy at which the shoulder is observed in the MDS spectrum. The suggestion of the feature's origin is further supported by the fact that it disappears completely with even small coverages of Ho, indicating that it is indeed the result of a surface state of the 7×7 surface. The smaller shoulder at 12.7 eV has been much studied[45,70] and is due to the same surface state back bonds and dangling bonds as seen in the UPS spectrum; but with MDS they are convoluted into the same feature.

It may upon first consideration be somewhat surprising that the three surface states are more apparent in the UPS spectrum than in the MDS spectrum despite the MDS's surface sensitivity. Masuda states the reason for this is that the adatom dangling bond state is half filled, so that if an electron from this state neutralises the He^+ ion in the AN process, the liberated electron may not originate from this state and will instead arise from free atoms or neighbouring adatoms, and since these are fairly sparse (6.7 Å for nearest neighbour

adatoms[140]), this is unlikely as the transition rate decreases exponentially with distance between sites.[70]

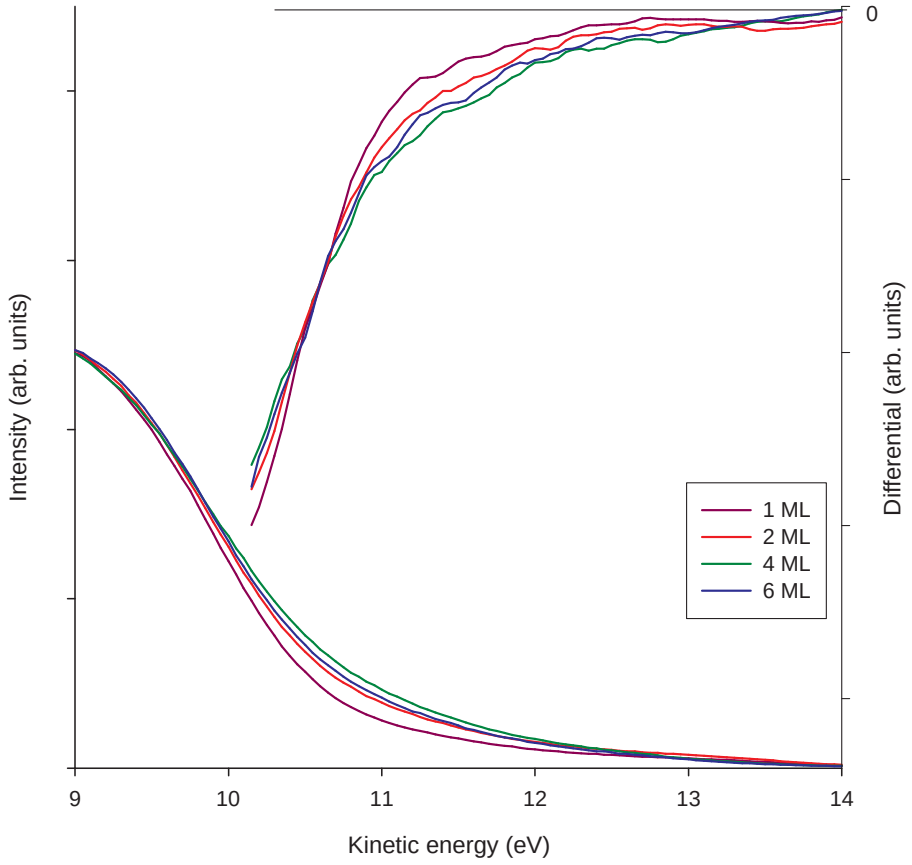

Figure 5.5: MDS spectra for various $HoSi_{2-x}$ coverages on Si(111). The right hand axis shows the first differentials of the spectra. Differentiated spectra have been 3-point smoothed.

The de-excitation process that occurs for the Ho silicide samples is also RI+AN, providing further evidence for its semimetallic properties.[123] The main peak in all the 2D and 3D Ho silicide spectra is due to Si 3*p* bulk states as in the case of Ho on Si(100) and the clean Si(111) 7×7 surface.[70,138] A slight difference is apparent between the 2D and 3D surfaces in the spectra's higher energy tails (approximately 11-14 eV), where emission due to surface states is expected. This region is shown in more detail in figure 5.5. To emphasise the subtle differences between the spectra, the differentiated spectra are also presented.

The energy range over which the differences occur correspond to the region with a high *p*-state contribution in the DFT predicted SDOS. As the He 2^3S de-excitation is sensitive only to the outermost orbitals of the surface, and this feature is at a relatively high energy,

this indicates a difference in the electronic structure of the top buckled Si layer.

5.3.2 The H Terminated $HoSi_{2-x}$ Surface

LEED Results

After H termination of the surface, the 2D silicide had a $p(1 \times 1)$ LEED pattern, although the three-fold symmetry was reversed compared to the clean silicide which indicates a switch in the surface buckling direction from B-type to A-type as expected.[131] For the 3D surface, the $(\sqrt{3} \times \sqrt{3})R30°$ LEED pattern remained after hydrogenation and the same switch in the three-fold symmetry was again observed. If the hydrogenated 2D surface was heated to around 400 °C, the H largely disassociated from the surface, evidenced by a re-reversal of the three-fold symmetry due to a flip of the top bilayer back to B-type. The symmetry reversal was not perfect and the LEED pattern showed strong hints of six-fold character suggesting not all of the H disassociated in this way. Other studies have also observed this process.[19]

UPS Results

Figure 5.6 shows the UPS spectra for all Ho coverages after H termination. The spectrum for Si(111) 1×1-H is provided for reference.

The surface and bulk density of states for Si(111) 1×1-H have previously been calculated by Pandey which show a large drawn out feature from the bulk between approximately -2 and -4 eV.[141] This same feature is visible in the UPS spectrum for Si(111) 1×1-H at the same energy range. A UPS peak at -6.5 eV corresponds to a small, local maximum in the SDOS.

On the H-terminated silicide surfaces, the feature labelled *a* in the spectra is at a similar energy to a feature observed previously for clean Ho silicide from Ho emission and p_z surface states. Feature *b* has previously been attributed in Er silicide to Er 5*d*-Si 3*p* hybridised surface resonances.[20,123] A feature at similar energy to that labelled *c* has been observed in H terminated 2D $ErSi_2$ and arises from H-RE and H-Si bonds similar to the Si(111) 1×1-H spectrum.[19] The energy of this peak clearly progresses with RE coverage.

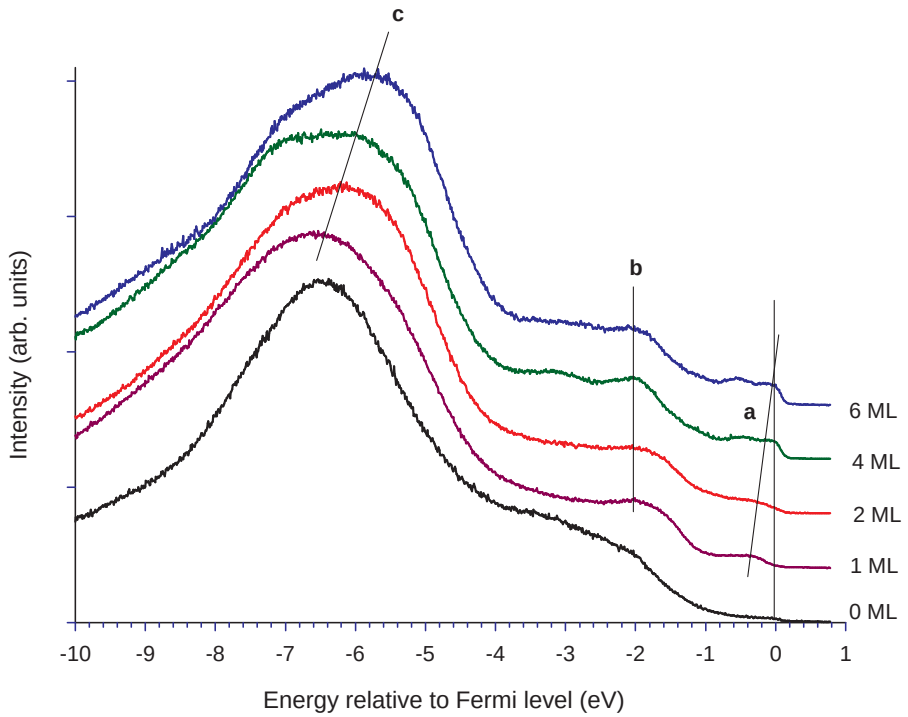

Figure 5.6: UPS spectra as a function of Ho coverage for H terminated Ho silicide surfaces. Spectra have been normalised and offset for clarity.

MDS Results

MDS spectra from the H terminated surfaces are presented in figure 5.7. The differentiated spectra and a view over a reduced energy range are presented in figure 5.8 to emphasise any differences between the spectra. When the Si(111) 7×7 reconstruction surface is terminated with hydrogen, it has previously been suggested that the work-function of the surface decreases, so the de-excitation process of the He 2^3S switches predominantly to AD.[48]

In the presented Si(111) 1×1-H spectrum, features are slightly more distinct than in the other MDS spectra. The spectrum also displays a high-energy tail, which does not appear in the H-terminated silicide spectra. Both of these characteristics are indicative of AD suggesting that the surface is either insulating or semiconducting with a wide band-gap.

In the Si(111) 1×1-H spectrum, the main peak at 8.7 eV occurs from Si 3*p* bulk states and also corresponds (when considering the energetics of the AD process) with feature *c* in the UPS spectra arising from H-Si bonds.[70]

A shoulder that occurs at 10.5 eV for the Si(111) 7×7 surface spectrum due to dimer

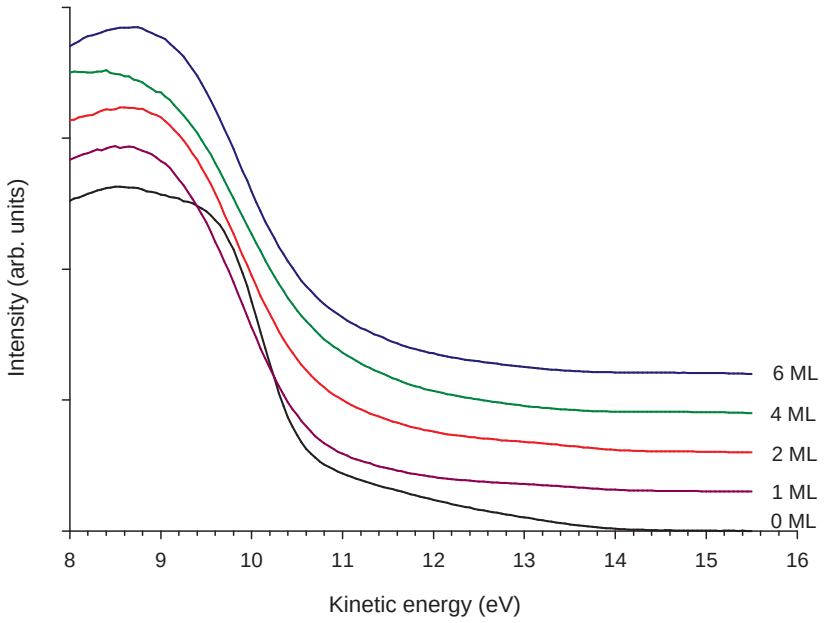

Figure 5.7: MDS spectra of various coverages of Ho silicide terminated with H. Spectra have been normalised and offset for clarity. Below 8 eV, secondary electrons begin to dominate the spectra.

states is not present which indicates that the surface is now completely H-terminated.

The spectra for the H-terminated silicide coverages are slightly different to the Si(111) 1×1-H spectrum in that distinct features are less apparent and the high energy cut-off occurs at a lower energy. This suggests that RI+AN has become the dominant de-excitation process. The change in de-excitation process indicates that the work-function has been increased compared to the Si(111) 1×1-H sample. It is expected that RI+AN would occur as Angot *et al.* previously noted that the H terminated 2D $ErSi_2$ is semiconducting.[128]

The surface states that previously resulted in emission for the clean silicide surfaces are substantially quenched by the H, and the spectra are dominated by the hydrogen bonds. The main peak for the Si(111) 1×1-H is at the same energy as for the H-terminated silicide, which suggests that for the silicide also, this is due to Si 3*p* bulk states and H-Si bonds, as in both cases the pre-hydrogenated surfaces are terminated purely by Si atoms.

The emission intensity of the Si(111) 1×1-H spectrum above approximately 10 eV is more than for the H-terminated silicide spectra. Emission in this range for the H-terminated Si could potentially be due to the Si backbond.

The spectra and their differentials indicate that there are very slight differences be-

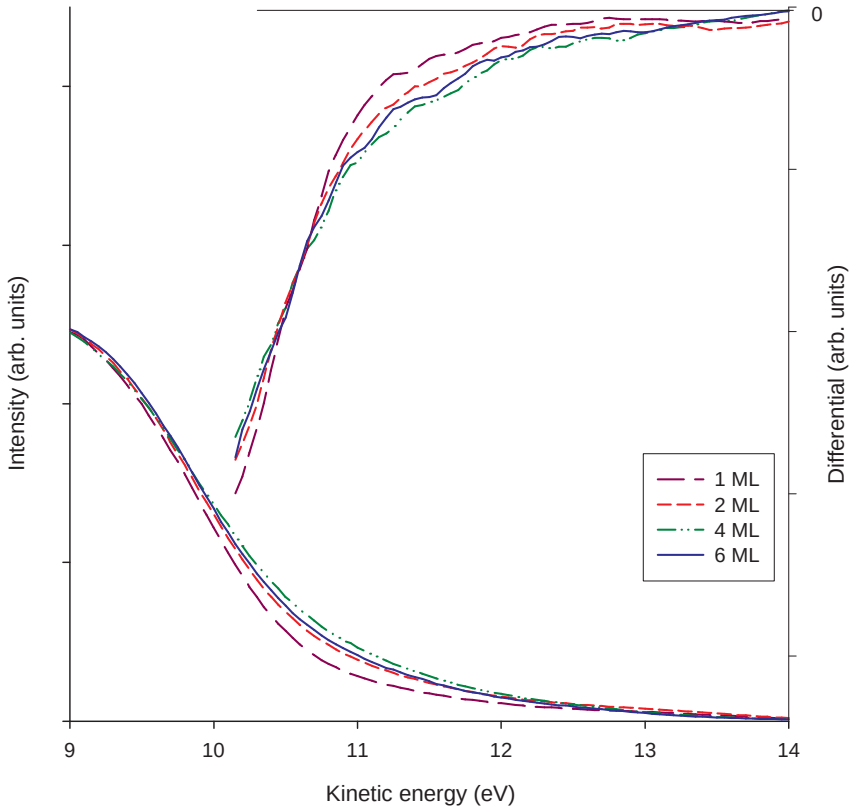

Figure 5.8: MDS spectra of various coverages of Ho silicide terminated with H. The right hand axis shows the differentiated spectra.

tween the 2D and 3D surfaces. These might be due to slight differences in the surface rumpling or small differences in where the H locates, as the 3D structure also contains vacancies within the flat Si layers into which H might absorb.[19]

As MDS spectra achieved through the RI+AN are self-convoluted, it is possible to deconvolute the spectra in order to achieve an estimate of the SDOS modified by the transition probability of the de-excitation process.[13] This has been conducted using a Fourier transform method mentioned previously. Results of this deconvolution are provided and compared to DFT in section 5.5.

5.4 Theoretical SDOS Calculations

5.4.1 Clean $HoSi_{2-x}$ surface

Electronic structure calculations and geometry optimisation for the $HoSi_2$ surface were performed by Dr. Chris Eames using the `CASTEP` code.[11] For the clean silicide surface, the calculations were run in parallel on a Beowulf cluster of 33 machines, each with dual Intel Pentium 4 Xeon processors running at 1.7 GHz in the Department of Physics at York. A typical geometry optimisation calculation where the structural energy is iteratively minimised used 18 processors and ran for approximately 200 hours.[114]

For more details of the calculations please refer to references 114 and 134.

5.4.2 The H-terminated $HoSi_{2-x}$ Surface

For the H-terminated surface, calculations were again performed by Dr. Chris Eames using the `CASTEP` code, but this time on the Sheffield node of the White Rose Grid. Typical geometry optimisation calculations took approximately 40 hours and required nine 2.4 GHz AMD Opteron processors.

A number of possible structures were investigated using this approach, including calculations for both one and two H atoms per unit cell. For one atom per unit cell, both A and B-type surface buckling were investigated for sites 0-4 (as illustrated in figure 5.2) i.e. A_i and B_i for $i = 0 - 4$. For the 2 atoms per unit cell calculations, both A_{ij} and B_{ij} were investigated for $i = 0 - 4$ and $j = 0 - 4$ where $i \neq j$ and either *i* or *j* must equal 3 or 4

to reduce the number of possible permutations and since it is accepted that at least one H atom must bond to one of these sites.

The total hydrogenation energies for each of these geometry optimised structures is presented in table 5.1.

Structure	Optimised Structure	E_H (eV) [DFT[134]]	E_H (eV) [Hückel model[133]]
A_0	-	-1.306	-
A_1	-	-2.153	-
A_2	-	-2.591	-
A_3	-	-2.547	-
A_4	B_3	-2.787	-
B_0	-	-1.400	-
B_1	-	-1.275	-
B_2	-	-2.154	-
B_3	-	-2.795	-
B_4	A_3	-2.554	-
A_{03}	-	-3.591	-5.862
A_{13}	-	-4.470	-6.687
A_{23}	-	-5.072	-10.982
A_{43}	-	-3.821	-
A_{04}	-	-2.571	-
A_{14}	-	-4.721	-
A_{24}	-	-4.590	-
B_{03}	-	-3.749	-6.021
B_{13}	-	-4.788	-9.466
B_{23}	-	-4.719	-8.225
B_{43}	-	-3.873	-
B_{04}	-	-2.694	-
B_{14}	A_{23}	-5.052	-
B_{24}	A_{13}	-4.379	-

Table 5.1: Total hydrogenation energies for 24 modelled structures from DFT. The bilayers of some structures spontaneously reversed during the optimisation process as indicated in the second column. The hydrogenation energies calculated by Sonnet *et al.* using the Hückel model are provided for reference.[133] DFT calculations have been provided courtesy of Dr. Chris Eames.

Of the one hydrogenation site structures, the B_3 is the most energetically favourable although the A_4 site is only slightly lower in energy, and when geometry optimised, the termination reverses so that the buckling alters to B-type and hence the H is now in site 3.

Almost all of the two site per unit cell structures are more energetically favourable than one site. Of these, the A_{23} has the largest hydrogenation energy; however, of all the

B-type structures, the B_{14} is favourable which optimises to the A_{23} structure.

If occupation of the sites occurs sequentially, one would expect the initial H atom to occupy the B_3 site. A second H atom would either allow the structure to remain B-type (B_{03}, B_{13}, B_{23} or B_{43}) or undergo spontaneous bilayer reversal to an A-type surface buckling for which site 3 becomes site 4 (A_{04}, A_{14}, A_{24} or A_{43}). As we know that upon H-termination, A-type buckling occurs, we can reject any B-type structures. The remaining A-type structures are all higher in energy than the A_{23} structure which must occur concomitantly.

5.5 Deconvoluted MDS Spectra Compared with DFT

5.5.1 Clean $HoSi_{2-x}$

As MDS gives an approximately self-convoluted spectrum, it is possible to deconvolute the spectrum in order to achieve an estimate of the SDOS modified by the transition probability of the de-excitation process.[13] $P(\varepsilon)$, the transition probability (effectively the self-convoluted MDS spectrum), is given by the self-folded integral:

$$P(\varepsilon) \propto \int_{-\varepsilon}^{\varepsilon} U(\varepsilon - \Delta\varepsilon)\, U(\varepsilon + \Delta\varepsilon)\, d(\Delta\varepsilon), \tag{5.1}$$

where $U(\varepsilon)$ is the transition density for an electron in the surface i.e. the local DOS modified by the transition probability[13] and ε is the mean binding energy of the electrons involved in the transition relative to E_F. This expression can be solved for $U(\varepsilon)$ providing us with an effective deconvoluted signal. This has been done for the $HoSi_{2-x}$ MDS spectrum. The DFT calculated SDOS is presented alongside deconvoluted experimental results to allow a direct comparison in figure 5.9.

With the self-convoluted spectrum, one cannot know from what binding energy an electron originates, but as the spectra are now deconvoluted, the energy scale can be converted to the binding energy of the electron.

The deconvolution of the 1 ML spectrum shows poor agreement with the theoretical prediction. However, it is known that a nominal 1 ML coverage does not form a uniform 2D coverage,[142] as can be seen in figure 5.10. Gaps in the 2D silicide are apparent revealing unexposed Si underneath. A few 3D islands are also visible. The 2 ML nominal

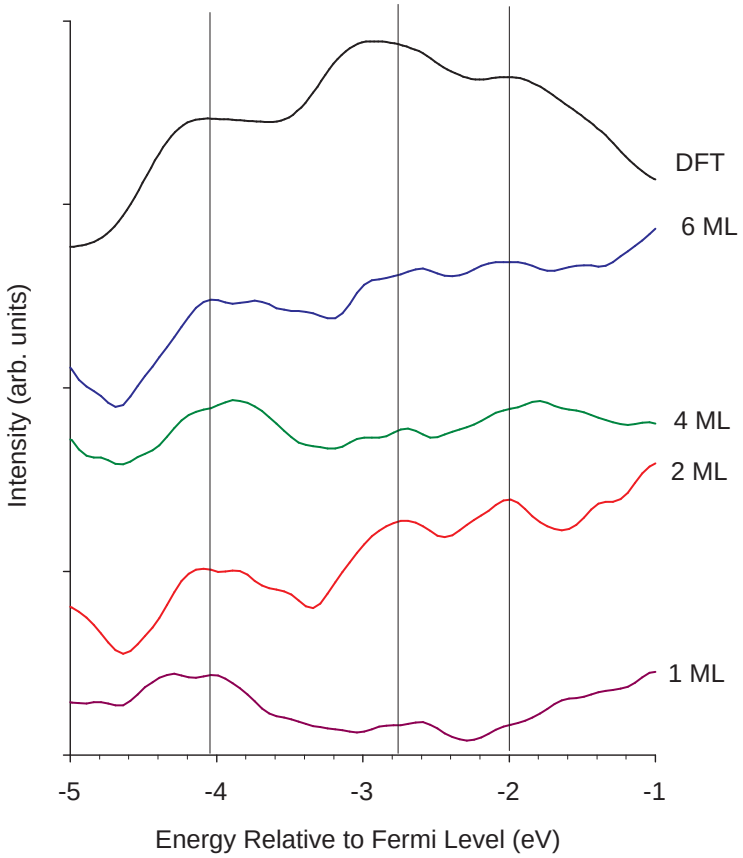

Figure 5.9: Deconvolution of MDS spectra for various Ho silicide coverages on Si(111) compared to DOS calculated by DFT for the 2D $HoSi_2$ surface. Deconvoluted spectra have been smoothed and offset for clarity.

coverage film seems to have a much more uniform 2D coverage with some 3D islands evident on top of this. These islands are all of very similar height at (5.3 ± 0.5) Å and have an average full width half maximum diameter of (12 ± 3) nm.

The 2 ML deconvolution shows the best agreement to the DFT, again supporting the view that the 2 ML coverage exhibits predominantly 2D behaviour. This growth pattern has been observed extensively within the group using STM when growing 2 ML films in this fashion. For thicker coverages, the 4 ML and 6 ML also have reasonable agreement to the DFT for the complete unit cell model which includes the buckled bi-layer, the Ho layer and down to the Si8 layer. The three features from the DFT are still apparent, but are less intense than for the 2 ML surface. This suggests that the SDOS is slightly altered between the 2D and the 3D surfaces. This may be an effect of a change in the rumpling amplitude or could result from a modification in the spacing between the Si2 layer and Ho layer.[17,143]

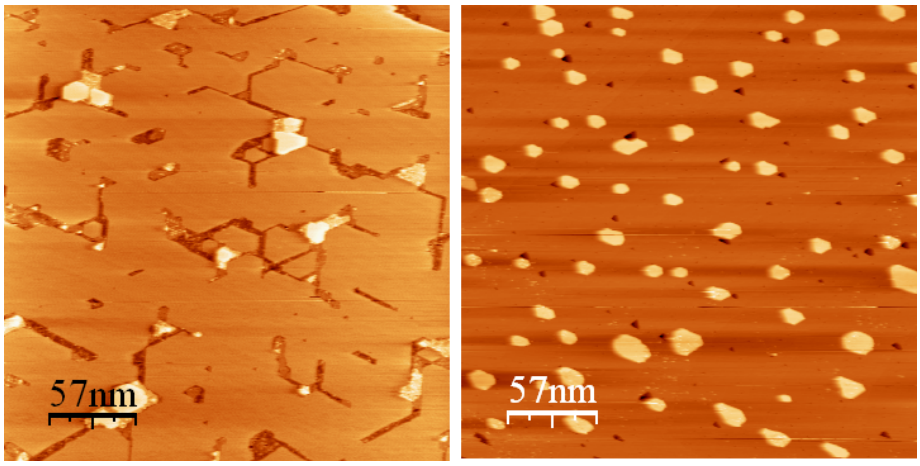

Figure 5.10: STM image showing incomplete silicide coverage in a 1 ML film of $HoSi_{2-x}$ on Si(111) (left). At higher coverages, as 3D silicide islands start to form, the silicide layer is complete (right). Reproduced with permission of Dr. Chris Eames.

Figure 5.11 shows the 2 ML MDS data and the DOS calculated by DFT for three different structures using parameters obtained by MEIS, LEED and the geometry optimised DFT structure.

Whilst all the DFT predicted SDOS using the different structural parameters all exhibit the same three maxima over this energy range, the deconvoluted MDS spectrum shows the best agreement with the SDOS where structural parameters have been derived from experimental techniques. This is most likely due to the fact that DFT is a zero Kelvin approach and does not take into account the realities of finite temperature on a system. Previous studies have indicated that the bilayer undergoes temperature induced vibrations and that temperature plays an important role in determining layer separations.[144]

The partial DOS of the individual layers has been calculated by DFT using the structural parameters derived from MEIS to determine the origins of the individual peaks. This analysis is presented in figure 5.12.

The Si1 and Si2 layers seem to contribute significantly to the peak at -2.0 eV, suggesting that this is a predominantly surface state arising from the bilayer. The peak at -2.7 eV, while having a large contribution from the bilayer, may also have a contribution from deeper into the structure. However, the peak at -4.1 eV seems to originate from much deeper into the structure - in the Si bulk layers themselves down to at least the Si7 layer, to account for the peak position. There is no apparent contribution from the buckled bilayer or the Ho layer. Although these are not themselves surface states, they may still protrude

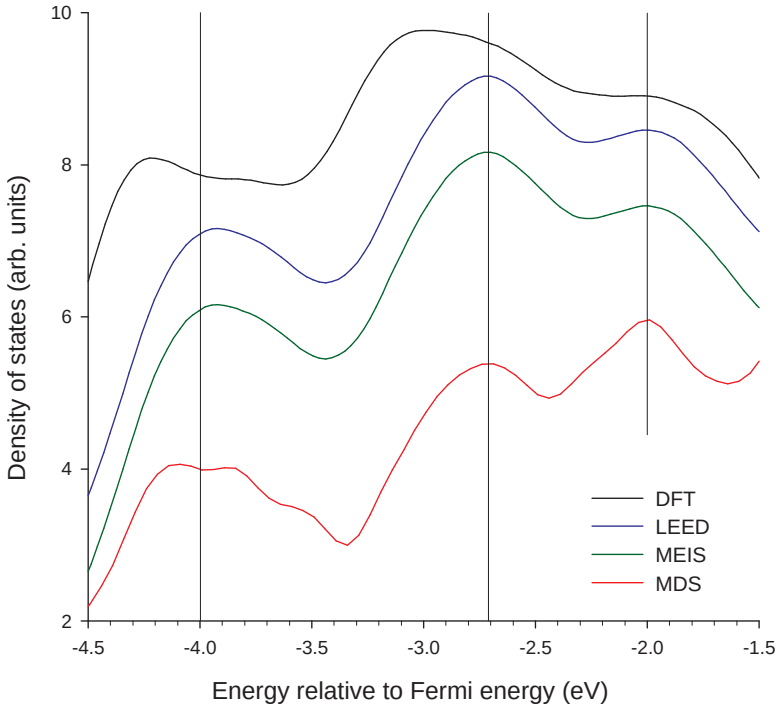

Figure 5.11: Deconvoluted MDS data for a continuous layer of 2D $HoSi_2$ on Si(111) compared to the DOS calculated for three different structures suggested by MEIS, LEED and zero Kelvin DFT. Data have been offset for clarity.

beyond the sample surface and will hence be detected by MDS.

As it is the two higher energy peaks that seem to alter between the 2D and 3D silicide, this suggests a change in the electronic structure of the Si bilayer itself. The low energy peak due to the substrate remains fairly constant for all coverages as the substrate states should not be affected by the formation of the silicide. Such a modification to the bilayer could arise from a slight change in rumpling amplitude, or a change in spacing between the RE layer and the bilayer.

5.5.2 H-terminated SDOS

As with the clean silicide surface, the H-terminated MDS spectrum for the 2 ML coverage has been deconvoluted and compared with the DFT predicted SDOS for several different H location models as shown in figure 5.13. The best fit to the experimental data seems to be with the A_{23} model, the one that has previously been shown as having the lowest energy structure. There are however slight differences in the energies of the peaks. This

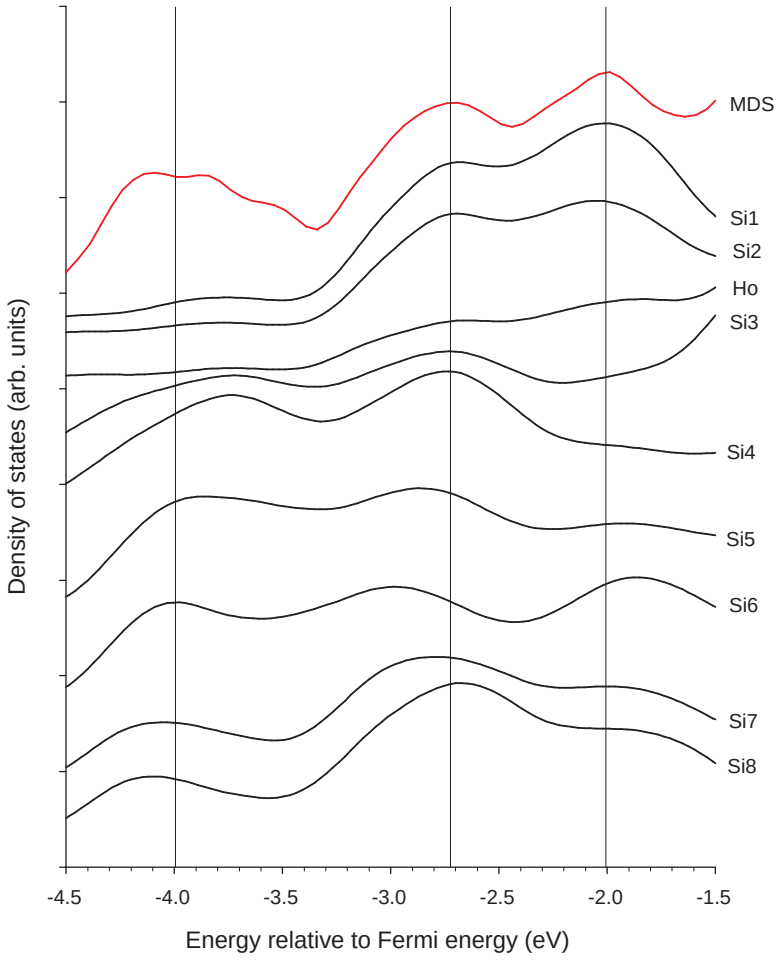

Figure 5.12: Layer by layer DOS produced with DFT for the $HoSi_2$ structure calculated using parameters obtained from MEIS. This is compared to the deconvoluted 2 ML MDS spectrum.

may well be due to defects within the surface and also the fact that the DFT model does not take into account finite temperature, which has previously been seen to have an impact on peak positions in the clean RE silicide due to thermal expansions.[114] Therefore, the experimental evidence also seems to suggest that the H locates in the A_{23} sites in the unit cell.

The layer resolved SDOS in figure 5.14 indicates that the peak at approximately -2.5 eV arises predominantly from the bulk structure, whereas the peak at approximately -4.0 eV comes from the bilayer itself.

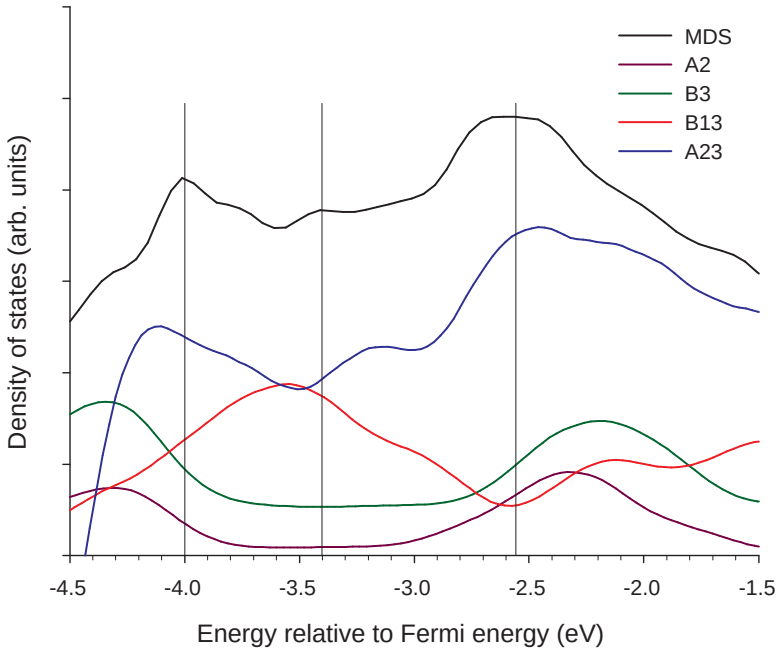

Figure 5.13: A comparison of the deconvoluted MDS of H-terminated $HoSi_2$ on Si(111) compared to SDOS predicted by DFT for several different H location models with both one and two H sites per unit cell.

5.6 Conclusions

Using a combination of MDS and UPS, the surface electronic structures of 2D $HoSi_2$ and 3D $HoSi_{2-x}$ on Si(111) have been compared, and found to differ subtly.

Features in both the MDS and UPS spectra for the clean and H-terminated Si(111) and Ho silicide spectra have been compared and assigned to bonds where possible.

Deconvolution of the MDS spectra has been conducted to retrieve the effective surface density of states which has then been compared with the DOS calculated using DFT to reveal a good agreement between the two for an unbroken 2D film. These deconvoluted experimental spectra again reveal a subtle difference between the density of states of the 2D and 3D silicide surface.

A comparison of the DOS achieved from DFT and deconvoluted MDS spectra has been conducted and over the energy range where surface features are expected, agreement in the location of maxima is very good, especially for the 2 ML Ho coverage which is thought to be the best approximation to a complete silicide coverage. For thicker layers, agreement is

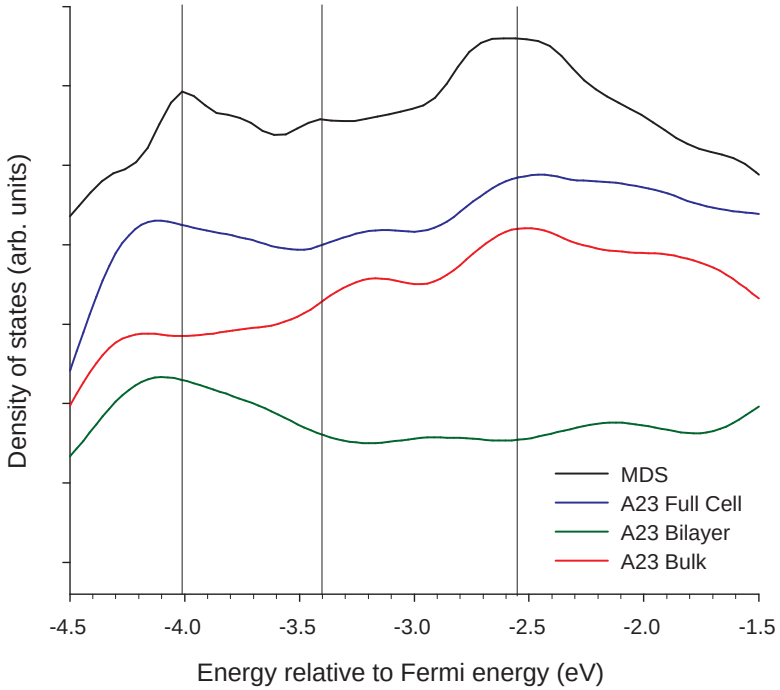

Figure 5.14: Deconvoluted metastable de-excitation spectrum of hydrogenated 2D Ho silicide on Si(111) compared to depth resolved partial density of states spectra calculated using density functional theory for the best fit model (A23). The near bulk states are responsible for the larger peak at around -2.5 eV.

slightly less good for the two higher energy features, which layer-resolved DOS calculated by DFT have shown arise from the top silicide layer. This suggests a difference in the electronic structure of the top buckled bilayer between the 2D and 3D silicide structures. Which could arise from a small change in the buckled Si surface rumpling, or the layer spacing between the Ho and buckled Si bilayer. The results indicate the extreme surface sensitivity of MDS.

The DOS calculated from parameters obtained experimentally agrees much better with that from the deconvoluted MDS spectra than the relaxed theoretical model at zero Kelvin. This suggests that finite temperature does modify the electronic properties of the surface as has previously been suggested.[115,145]

Layer resolved DFT suggests that as well as obtaining contributions from the top most layer of the surface, the MDS is detecting states originating deep within the surface. These must extend to the vacuum to be detectable in this way.

A comparison has also been conducted for the H-terminated surface between deconvoluted MDS and DFT for different possible H atom locations. The best agreement occurs with DFT for a model with two hydrogen atoms per unit cell: one surface site and one interstitial subsurface site. DFT has shown this to be the lowest energy state for absorption or adsorption of either one or two H atoms.

Again, DFT indicates contributions to features in the deconvoluted MDS spectrum arise from both the bulk and surface of the structure. There are also differences in the energy of states between the DFT and deconvoluted MDS; more so than in the clean silicide surface. This may again be due to temperature assumptions of the DFT model, or imperfections in the termination which is suggested by the incomplete buckling reversal.

Chapter 6

Iron Nanoclusters on Silicon Substrates

6.1 Introduction

Whilst much is known about the behaviour of individual atoms and bulk, solid state materials, far less is known about the physics governing the intermediate region. This is partly due to the difficulty in modelling nanoscale systems that consist of a relatively high number of atoms, and also to the difficulty in creating such structures of which nanoclusters are a subcategory. These are groups of between 5 - 25,000 atoms[146] which are preformed as nanoparticles under UHV conditions and subsequently may be deposited onto substrates, embedded into matrices,[147] or injected into liquids to form suspensions.[148] Such nanoclusters do not necessarily assume the same properties of bulk materials or their constituent atoms making them attractive for a variety of applications and fundamental studies.

6.1.1 Aims

This chapter aims to provide details of the surfaces properties of clusters by investigating the extent of the surface spin asymmetry present within the cluster-covered surface as well as identifying the electronic states that arise in such a surface.

It also acts as an initial study to highlight areas of interesting potential where more in-depth investigations could be directed in the future. These include investigations of the structural properties of the clusters and how these are modified by annealing, the effects of oxidation on clusters and also a partial characterisation of the clusters produced by the Small Leicester University Mesoscopic Particle Source (SLUMPS) from the University of

Leicester.

6.1.2 Properties

Clusters hold a fundamental interest, as the evolution of a material's properties may be studied as a function of increasing cluster size on an atom by atom basis. The electronic and magnetic properties of these nanoclusters differ from larger clusters and bulk materials due to the high proportion of atoms on the cluster surface and the reduced coordination number, $\langle n \rangle$, which is determined by the number of nearest neighbour atoms.[149]

Nanoclusters generally consist of preferred numbers of atoms referred to as magic numbers. For noble metals and alloys, these correspond to filled electronic shells,[150] whereas for transition metals they correspond with stable atomic geometries of complete geometric shells.[151,152] For larger clusters, faceting occurs to reduce the surface energy.[153,154]

As a system increases in size, a band structure develops. As such, nanoclusters exhibit much narrower valence bands around E_F than a bulk material which narrow further as the cluster size reduces as illustrated in figure 6.1. Such a narrowing modifies the material's properties from those of the bulk.[155]

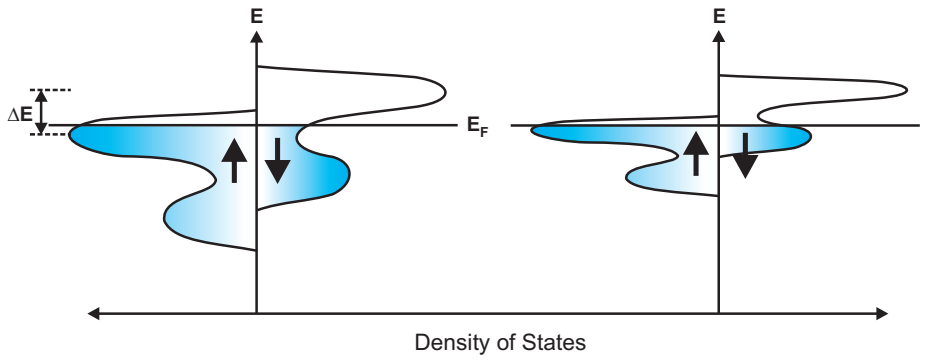

Figure 6.1: Narrowing of spin asymmetric valence band states around the Fermi energy leading to a greater spin asymmetry at E_F. The DOS on the left represents a bulk system, whilst that on the right represents a nanocluster. ΔE is the exchange energy of the system.

Magnetic Properties

Whilst many individual atoms exhibit non-zero magnetic moments as a result of localised orbital electrons, relatively few elements in the solid state maintain this magnetic moment,

as the causes of magnetism on the larger scale are quite different where valence band electrons are no longer localised. Nanoclusters occupy an intermediate state, and because of this, their magnetic properties are known to differ from those of the atomic and solid state.

In transition metals such as Fe, the ferromagnetic properties arise predominantly from the spin angular momentum, m_S, of the 3*d* states. As the valence band narrows in nanoclusters, the asymmetry in the spin-split DOS for the 3*d* states is exaggerated. This greater spin asymmetry around E_F leads to an increased spin magnetic moment. For instance, Fe_{12} clusters exhibit a moment of 5.4 μ_B per atom compared to the bulk value of 2.2 μ_B per atom. Upon the addition of an extra Fe atom, this is reduced to the bulk value, as this forms a more stable geometry which has the effect of quenching the orbital angular momentum and reducing m_S.[156] Such an increase in the spin asymmetry can cause materials that do not display signs of ferromagnetism in the bulk to display ferromagnetic behaviour as nanoclusters, as is the case with Rh.[157]

Similarly to the spin angular momentum, the orbital angular momentum, m_L, also increases with decreasing coordination number due to a combination of spin-orbit coupling and the reduced symmetry of the cluster. This lessens the quenching of m_L originating through band formation and delocalisation.[158] It has previously been shown that the orbital moment only increases away from bulk values within two atoms of the surface; however, this increase is marked.[159] This indicates the importance of atomic structure on the magnetic properties; and as such, the surface magnetism of the clusters is also expected to differ greatly.

A combination of m_S and m_L in clusters may lead to very large moment increases from bulk values. For example, in Fe, Co and Ni clusters between 20 and 700 atoms the moment is enhanced by up to 40% relative to bulk values;[160,161] and for clusters of Fe 250 atoms in size, m_S increases by 10 % and m_L by 250 % relative to the bulk leading to a total moment which is 15 % greater.[162]

As can be seen from figure 6.2, m_L decreases much more rapidly than m_S with increasing $\langle n \rangle$ as the orbital moment is much more sensitive to neighbouring atoms.

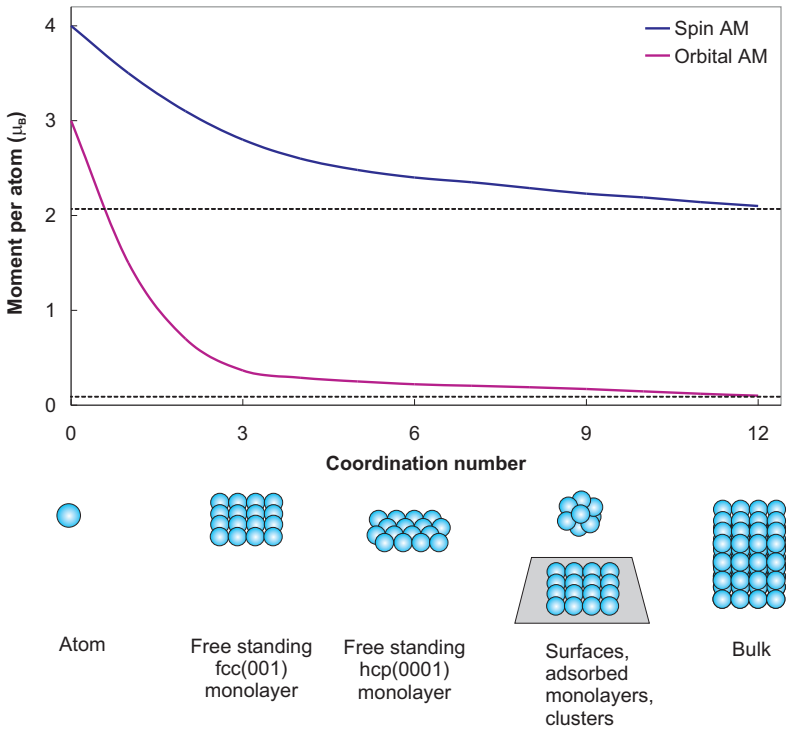

Figure 6.2: A sketch of the trends of spin and orbital angular momentum with changing coordination number.[146]

Domains

As nanoclusters are smaller than ~ 100 nm, the size above which domain wall formation may start to become energetically favourable, the clusters will be single domain, where alignment with an applied field is achieved purely by rotation of the magnetisation vector. As such, the clusters are governed by an Arrhenius relationship whereby the magnetisation after the removal of an applied field relaxes at a rate given by:

$$\frac{1}{\tau} = f_0 \exp\left(\frac{-KV}{k_B T}\right), \tag{6.1}$$

where τ is the relaxation time, f_0 is the attempt frequency, KV is the anisotropy energy, where K is the anisotropy, and V is the particle volume, and $k_B T$ is the thermal energy. For a minimum relaxation time of approximately 100 s and an attempt frequency of 10^9 s^{-1},[163] KV must be greater than approximately 25 $k_B T$ for ferromagnetic behaviour to occur. If values for $k_B T$ at room temperature are on the order of the anisotropy energy or greater, relaxation times will be extremely short, and the clusters will display superparamagnetic behaviour. The blocking temperature, the temperature for which half the moments are still pinned, will be low. For instance, in 5 nm Co nanoclusters it is 25 K; however, this

increases with particle size.[149]

The value of *K* will have contributions from the crystal anisotropy, the shape anisotropy, the stress anisotropy and the surface anisotropy, however it is thought that the shape anisotropy will dominate as for Fe, the crystal anisotropy, $K_{crystal}$ = 4.2×10^5 erg cc^{-1},[164] and the shape anisotropy for a prolate spheroid is given by:

$$K_{shape} = \frac{1}{2}(N_a - N_c){M_S}^2, \tag{6.2}$$

where N_a and N_c are demagnetising coefficients along the *a* and *c* axes of the spheroid and M_S is the saturation magnetisation. For an a/c value of just 1.1, for Fe, K_{shape} = 6.9 $\times$ 10^5 erg cc^{-1}.[165] The surface and stress anisotropies are expected to be small compared to the crystal and shape anisotropies.[166,167]

Cluster Surfaces

It is well known that low dimensional systems such as thin film surfaces can have unusual magnetic properties. Predictions have been made of an enhancement of the total magnetic moment at the surfaces of ferromagnets due to greater coupling between spins as moments are localised.[168,25] This may lead to enhanced Curie temperatures at thin film surfaces as was demonstrated in Gd(0001) by Weller *et al.*[168]

Whilst research into the surface effects in clusters has been extremely limited, the work that has been conducted also suggests that the unusual surface properties of low dimensional systems are extended to clusters. It is known that m_L increases rapidly towards a surface from the bulk due to lower quenching, and should therefore become significant in small clusters with high surface to bulk ratios. In fact, it has previously been shown that the magnetic moments of TiO nanoparticles originate only from the surface layers.[169] Also, a theoretical study by Dimitrov and Wysin has shown an increase in the coercivity in the surface atoms on clusters which is attributed to the high anisotropy energy at the surface arising from reduced nearest neighbour numbers and breaks in translational symmetry.[167] This anisotropy increases with decreasing cluster size.[170,171] It is also suggested that the surface moments are not completely coupled to the bulk spins and as such, the clusters are not completely single domain.[167,172] This leads to hysteresis within the particles.

6.1.3 Materials

The simplest nanoclusters are those constructed of single elements. It is these clusters that are discussed within this chapter. As it is extremely difficult to study free clusters with many techniques, it is usual to deposit them onto a substrate. By doing this, the nanoclusters' free particle magnetic behaviour will be modified by a cluster-surface interaction. Such interactions have been shown to decrease the moment from that of free clusters,[158,173] however the spin and orbital moments remain significantly greater than bulk values.[147,174] When coverage is sufficient to form a continuous layer on the substrate, bulk values have been shown to return.[173]

The co-deposition of clusters alongside an atomic vapour of a material such as Cu allows a matrix of clusters to be built up as a nanostructured, granular film, whereby the sizes and proportion of clusters may be controlled independently to preserve the clusters' unique properties which are desirable for some applications.[146,175] Even in a matrix state, the higher-than-bulk moments may be retained.[147,174,176]

6.1.4 Applications

Cluster properties can be tuned by controlling their size using mass selection. This gives them great potential as components in future nanoscale applications. Already, work is being conducted into forming memory storage devices out of nanoclusters with each cluster working as an individual bit; although currently, their blocking temperatures remain significantly below room temperature.[177]

Another potential application is as magnetic field sensors. GMR in granular films is well known, and has now been demonstrated in cluster assembled films.[149] The ability to alter the particle size and fraction of clusters in a matrix is not possible in other granular materials and allows for the films to be tuned to the necessary requirements.

Recently, the possibility of medical applications for nanoclusters have been realized. Iron oxide nanoclusters have been coated with a biocompatible polymer and injected into water for use in magnetic fluid hyperthermia.[148] A move to Fe nanoparticles with stable oxide coatings would allow a reduced concentration of material to be used due to their greater specific moment than pure oxide particles.[178] Work is also being conducted on using ferromagnetic nanoclusters for targeted drug delivery and cancer treatment.[178]

6.1.5 Growth Methods

A variety of different methods exist to produce nanoclusters including gas aggregation,[179] laser evaporation,[180] and seeded supersonic nozzle sources suited to alkali metal clusters.[149] All of these production methods rely on gas condensation. In this work, clusters are produced using the gas aggregation method using SLUMPS described later in this chapter.

6.2 The Cluster Source

SLUMPS was transported to York towards the end of this project and attached directly onto the MDS sample preparation chamber so that clusters could be deposited *in situ* to prevent contamination and allow all possible characterisation techniques available on the analysis chamber to be utilised. A schematic diagram of the source is provided as figure 6.3.

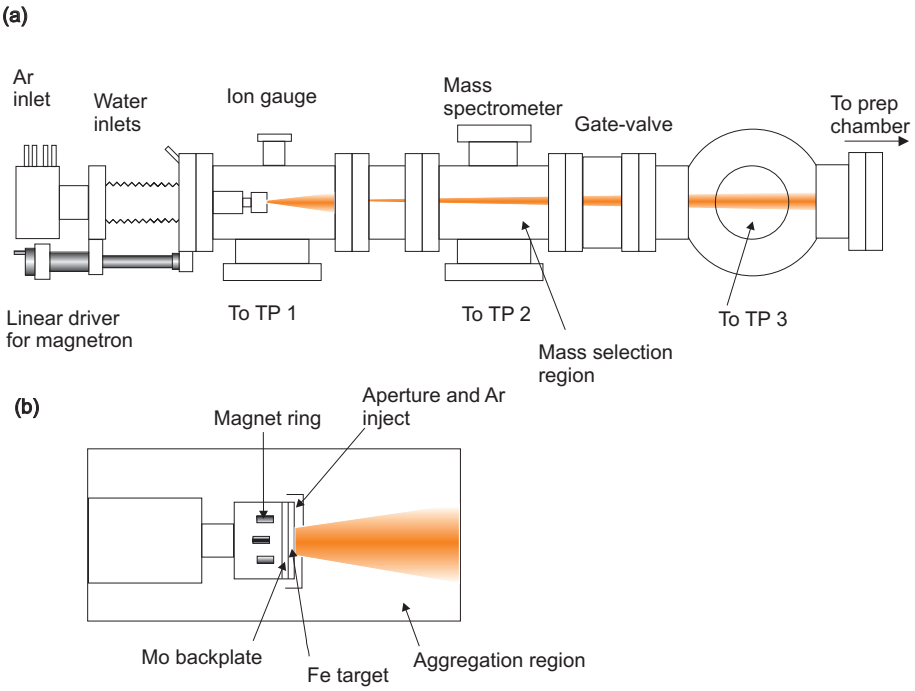

Figure 6.3: (a) Schematic diagram of the cluster source. (b) Magnified view of the magnetron cluster production region within the source. A similar cluster source is described in reference 181.

To operate the cluster source, Ar of 99.9995% purity is inlet through a leak-valve into a uniform ring injector around the sputter target at the front of the magnetron at a pressure of $\sim$ 0.1 mbar. The sputter target is elevated to a high voltage to form an Ar^+ plasma

region in front of it. A magnet ring behind the target ensures that ions bombard into the target and sputter off a small amount of the material (in the case of this work, Fe) generally as monomers or dimers. This material is then swept with the gas flow through a high pressure aggregation region where the clusters form. The cluster beam continues through an aperture into the mass selection region (not used in this project), and then into another chamber before entering the sample preparation chamber. At all these stages, the gas load is reduced by turbomolecular pumps, so that upon entering the final chamber in the cluster source, the pressure has been reduced to 1×10^{-5} mbar. Part way through the project, after the SPMDS experiments discussed within this chapter were completed, the turbomolecular pump on the mass selection chamber (labelled TP 2) failed. As no alternative was available, the cluster source was used with the remaining pumps only. This resulted in a pressure in the final chamber of the cluster source of 1×10^{-4} mbar. The effects of this change to the cluster characteristics was investigated using SEM, TEM, MDS and AGFM. Only the geometry of the clusters were thought to have altered significantly as less cubic clusters were observed.

6.2.1 Sample Preparation

Initially, clusters were deposited onto Si(111) as it is known that clusters adhere to the surface from preliminary studies, it is straightforward to obtain a clean surface and its electronic properties and the spectra produced by the clean surface are well known. The samples were cut from a lightly-doped, *n*-type wafer and were cleaned by dc heating, initially by degassing the samples for at least 8 hours at 400 °C followed by flashing several times at 1200 °C for a minute to remove the oxide before being allowed to cool to 900 °C. The sample was subsequently slow-cooled at less than 100 °C per minute to room temperature. LEED patterns were checked to ensure the formation of the 7×7 reconstruction. The Ar pressure in the magnetron was increased to $\sim$0.1 mbar and the magnetron set to a power of 35 W. The gate-valve to the preparation chamber was then opened to allow the source to deposit. Deposition rates were calibrated using a quartz crystal rate-meter and were much higher than would be required for epitaxial growth with typical rates of around 0.4 nm min^{-1}. After deposition, the sample was transferred to the analysis chamber.

All depositions quoted in this chapter are those of a body centred cubic (bcc) Fe film of uniform thickness across the sample.

6.3 Results and Discussion

6.3.1 SEM and TEM Results

Once UHV measurements had been completed, the samples were removed from the system and investigated using an FEI Sirion S-FEG SEM capable of high resolution SEM and energy dispersive x-ray spectrometry (EDS) for elemental mapping. Images obtained for four cluster coverages are provided in figure 6.4.

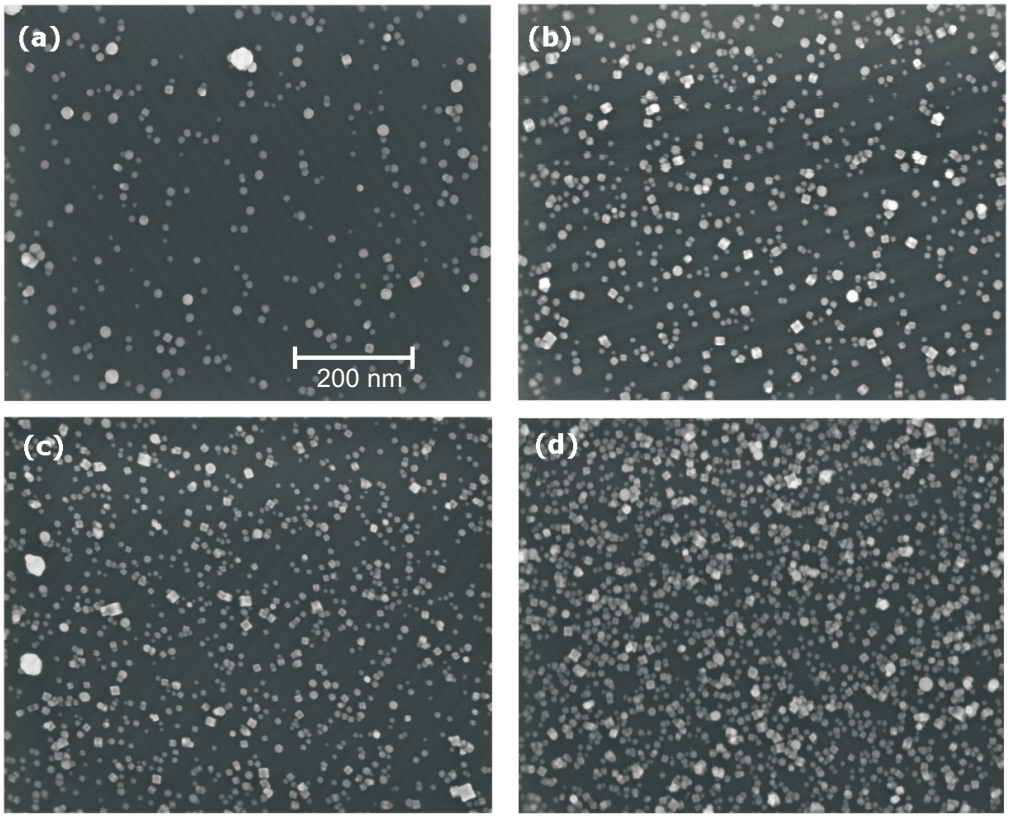

Figure 6.4: SEM images obtained with a 5 kV beam energy of the Si(111) surface with (a) 0.3 nm, (b) 0.6 nm, (c) 0.8 nm and (d) 2.5 nm of Fe cluster deposition coverage. The scale bar in image (a) is valid for all images.

The images show different amounts of Fe clusters deposited on the clean Si(111) 7×7 surface with the Si step edges just visible in the background. Both spheroid and cuboid clusters are apparent for all the coverages.

The clusters on the Si surfaces show no evidence of directional alignment relative to the substrate. This indicates that either the clusters are strongly bonded to the surface by chemisorption as they land, and therefore cannot move into more favourable orienta-

tions, or that there is very little difference in energy between different cluster orientations relative to the substrate. STM evidence and previous studies suggests the latter by physisorption.[182]

The clusters do not seem to be randomly distributed across the surface and in some cases appear to form loose chains. This may be a result of magnetic interactions between the clusters prior to landing on the substrate, or it may even be possible that movement occurs after they have landed, but such movement must be limited, as all the clusters do not condense onto the same part of the substrate. This alignment occurs between both cuboid and spheroid clusters.

While most of the cuboid clusters appear to rest on a face, a small minority appear to rest on a vertex or apex. This may occur when clusters land on surface features such as impurities or step edges, and immediately bind to them, preventing further movement.

The proportional cluster coverages on the Si surface were calculated using ImageJ image analysis software for the samples illustrated in figure 6.4. These coverages were estimated as (a) 7.9 %, (b) 15.0 %, (c) 17.9 % and (d) 37.5 %. These increase in an approximately linear fashion with the nominal coverage, as measured by the quartz crystal ratemeter.

The cluster size distributions measured using a Zeiss electro-mechanical grain size analyser for the four SEM image coverages are presented in figure 6.5. The sample sizes used to determine the distribution were 309, 508, 928 and 614 clusters for the 0.3, 0.6, 0.8 and 2.5 nm coverages respectively. The cluster size is defined as the diameter or the width depending on whether the cluster is a spheroid or a cuboid.

All the distributions occur over a very similar range, with mean diameters of (14.3$\pm$0.3), (13.5$\pm$0.3), (12.8$\pm$0.2) and (11.8$\pm$0.2) nm for the 0.3, 0.6, 0.8 and 2.5 nm coverages respectively. Any differences in the distributions are thought to occur due to variations within the source itself, such as plasma power or Ar pressure. All the distributions exhibit a peak at around 12 nm, and with the exception of the 2.5 nm sample, they also exhibit a shoulder or a peak at 16 nm. It is predicted and previously demonstrated that the size distributions produced by gas aggregation sources such as this are log-normal and are determined by collision statistics.[183,184] Only the 2.5 nm sample distribution appears to be log-normal. The other distributions all have tendencies towards a bimodal distribution, however this may be due to an insufficient sample size. Low resolution TEM has been

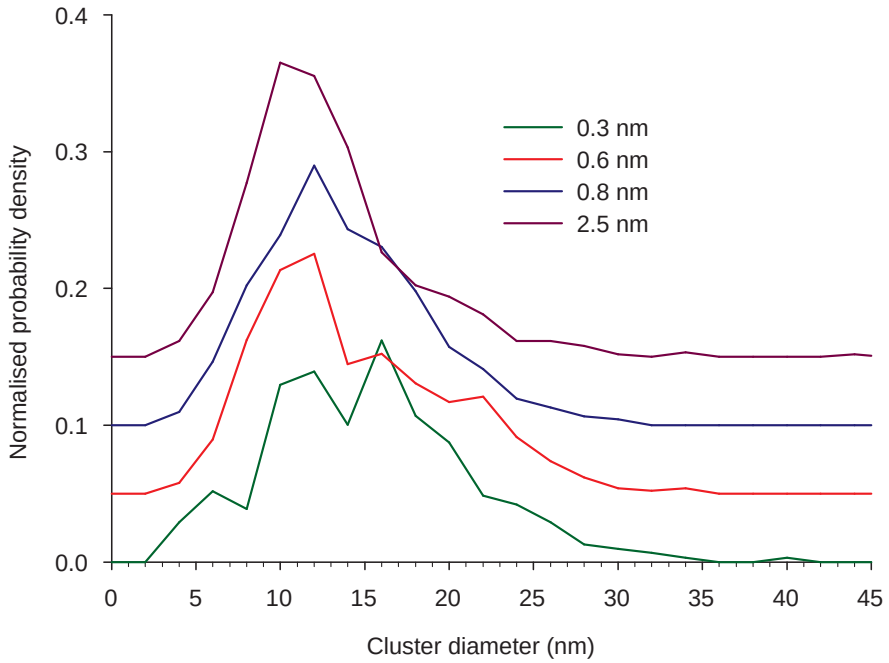

Figure 6.5: The size distribution measured using a grain size analyser for the samples upon which SPMDS was conducted. Some of the distributions appear to be bimodal.

conducted to ascertain whether this is indeed the case, and should provide more accurate size measurements due to the technique's higher resolution. For TEM, clusters were deposited on holey carbon film TEM grids and imaged with a JEOL 2011 TEM. One such TEM image is provided in figure 6.6.

Now it is possible to see that some of the spheroid clusters are faceted, with both octagonal top profiles consistent with a truncated rhombic dodecahedral geometry, and hexagonal top profiles, which are consistent with both cubic clusters and truncated rhombic dodecahedra. However, for either of these geometries to be observed as having an hexagonal top profile, the clusters would need to balance on an apex, which although demonstrated on the Si surface, is somewhat rare. It is therefore possible that the hexagonal profile clusters are yet another morphology that the clusters may assume. High resolution (HR) TEM has been used to capture these morphologies. Results are presented in figure 6.7.

Vystavel *et al.* have previously conducted a study of Fe nanoclusters from a source similar to SLUMPS, but producing clusters of 9 nm average size (including a 2 nm oxide shell).[185] After annealing the samples, some of the clusters had truncated rhombic dodecahedral structure, although spheroidal ones were also observed.

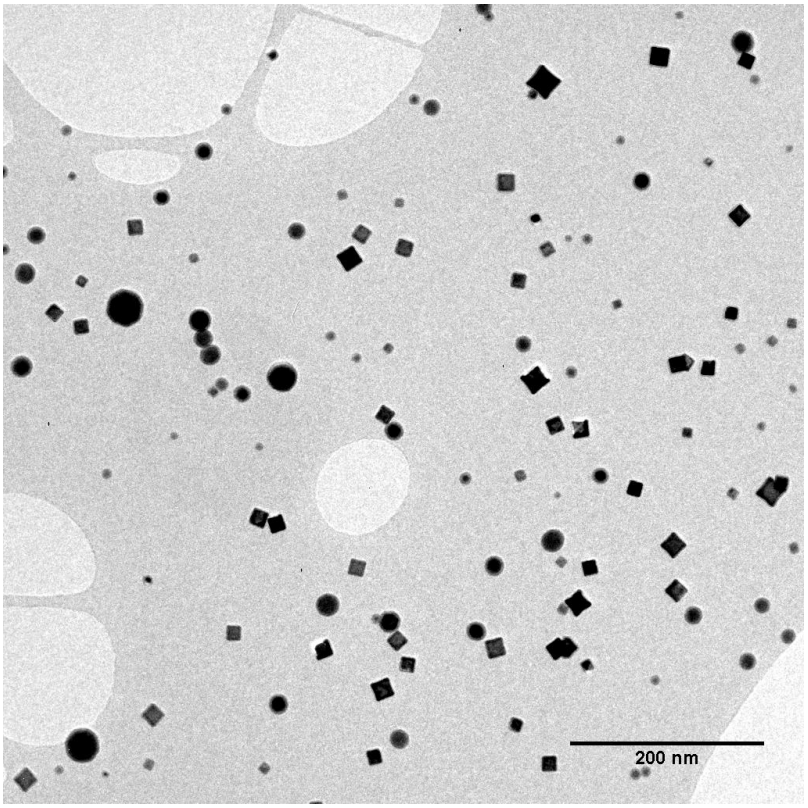

Figure 6.6: Low resolution TEM image of a 0.5 nm cluster coverage deposited on a carbon film. Both cubic and faceted clusters are present. Image obtained by Dr. R. Kröger.

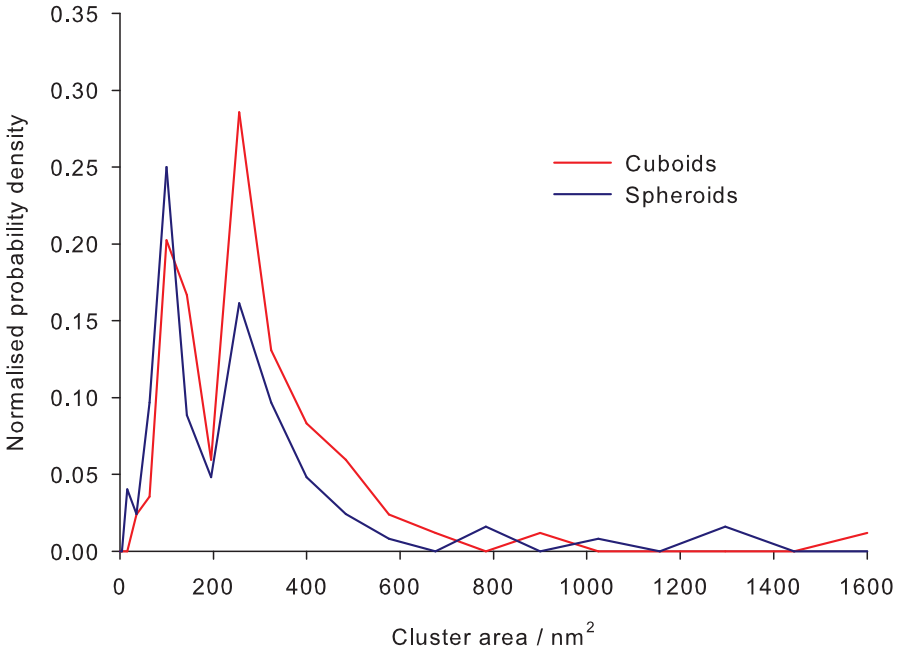

Figure 6.7: TEM images of (a) a hexagonal top profile cluster, (b) an octagonal profile cluster and (c) a rectangular top profile cluster with smaller spheroid clusters. Images obtained with the assistance of Steffan Lea.

Wang *et al.* have also used a gas aggregation source to produce Fe clusters. It was noted that nanoparticles smaller than $\sim$ 20 nm are generally round, where those greater than this size tend to be faceted.[186] In this study, cubic clusters were observed along with truncated rhombic dodecahedral ones. Previous studies have demonstrated that Fe clusters tend to be faceted with 12 $\{110\}$ planes that are truncated by 6 $\{001\}$ planes (resulting in a truncated, rhombic dodecahedral geometry), but the degree of truncation depends on the deposition temperature.[187] For a cubic cluster to form, the geometry must be completely bound by these 6 $\{001\}$ planes.

If surface energy dominates, the cluster geometry will be determined by the rate of growth in the particular crystal directions, which is governed by the surface energy of the lattice plane perpendicular to the direction of growth. For bcc structures, the $\{110\}$ planes are the closest packed, and therefore the lowest energy surface. Cubic structures terminated by $\{001\}$ surfaces have relatively high surface energies. From previous studies, evidence suggests that these are less likely to occur for high temperature depositions.[186] This implies that growth kinetics dominate over surface energy in cubic cluster formation.

A theoretical study investigating the energetics of geometries of Fe clusters by Besley *et al.*[188] suggests that the truncated rhombic dodecahedral geometry is the most stable for systems consisting of between 2,000 and at least 10,000 atoms. This compares to approximately 230,000 atoms in a typical 14 nm dimension cubic cluster reported here. In a study by Depuis *et al.* where Fe clusters were produced in a laser vaporisation source, only spheroid clusters were noted.[189]

The fact that the SLUMPS cluster source is able to produce different cluster morphologies simultaneously suggests that there are competing processes for cluster formation occurring in the source, and the conditions within the source are not uniform. Conditions that may vary include the magnetron power and gas pressure, as these will determine the time and energetics of formation.

The size distribution from the combination of several low resolution TEM images all from the same 0.5 nm coverage sample are provided in figure 6.8.

As the contrast with the background is better than with SEM, ImageJ has been used to calculate a distribution of the area of surface that the clusters cover. The distribution has been separated into cuboid clusters and spheroid clusters, to observe any size difference between the two. It is very apparent that the distributions for both the cuboids and

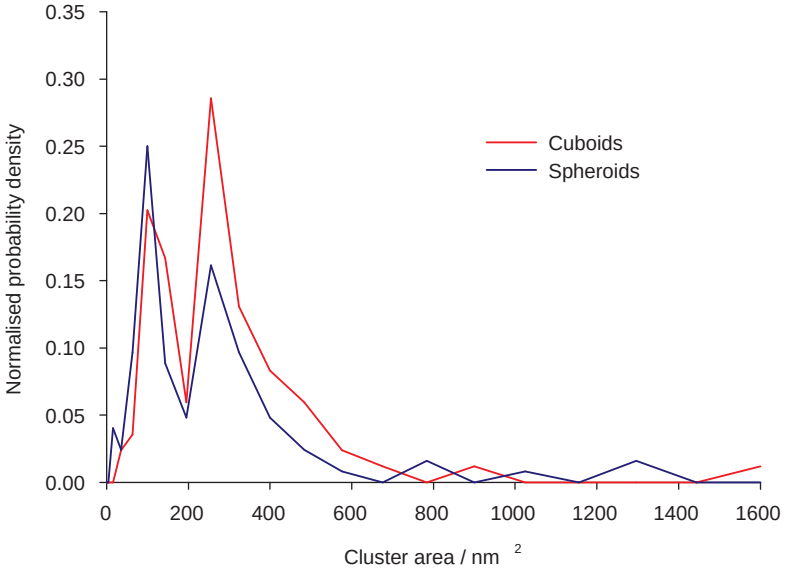

Figure 6.8: Size distribution of clusters from low resolution TEM images. The distributions for both cluster types are clearly bimodal.

spheroids are bimodal, and so the difference in geometry does not seem to depend on the cluster size.

It is also apparent that a large proportion of the clusters are cubic even for very low sizes, which contradicts previous studies that suggest that smaller clusters are likely to possess a spherical morphology.[186,187]

The ratio of the sides of the cubic clusters has been measured from the low resolution TEM images for a number of cuboid clusters and found to be 1:1, showing that they predominantly seem to have square top profiles.

High resolution TEM has been conducted on a cuboid cluster exposed to atmosphere to determine its crystal structure and also the phase of the oxide coating (figure 6.9).

The crystal planes of the cluster and the oxide layer are very apparent. The oxide layer also seems to have formed a crystal structure with few faults and a clean interface with the Fe surface.

Diffraction measurements on the cluster conducted by Dr. R. Kröger reveal that it consists of a bcc structure with the surfaces in the high-energy $\{001\}$ planes, and furthermore that the oxide is Fe_3O_4 with a $\langle 110 \rangle$ surface direction. This is revealed to be the lowest mismatch orientation to the $\{001\}$ Fe surface at 3% and is the same orientation that occurs

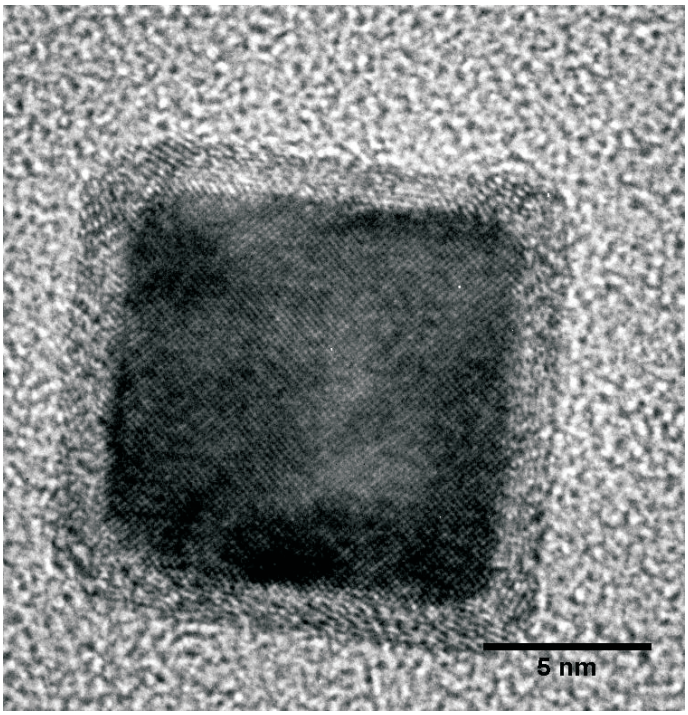

Figure 6.9: HRTEM image of an Fe nanocluster deposited on a carbon grid. The oxide layer is clearly visible. Image obtained by Dr. Roland Kröger.

on bulk Fe surfaces.[186,190]

From the low resolution TEM image, it is possible to measure the average thickness of the oxide layer on the clusters. This was found to be (2.7 ± 0.1) nm which corresponds with previously reported oxide thicknesses on cubic clusters,[186] and is independent of cluster size.[178] For an average sized cubic cluster with 12 nm dimensions inclusive of such an oxide coating, the pre-oxidation cluster size has been calculated as 10.7 nm assuming a single crystal fcc Fe_3O_4 oxide layer with a lattice constant of 0.8397 nm.[191]

Mössbauer spectroscopy has previously been conducted by Depuis *et al.*[189] who noted that for 2-6 nm clusters, 20 % of a deposited sample exposed to atmosphere consisted of γ-Fe_2O_3 (maghemite) and Fe_3O_4 (magnetite) which suggests that more than one oxide phase may occur on Fe clusters, with the latter being more abundant. It was also suggested that these oxides could be removed by annealing the samples to 500 °C.

Figure 6.10 shows an STM image of an 0.8 nm coverage cluster surface on Si(111). The sample was grown in the MDS system and then transferred in atmosphere to the STM, as it was not possible to couple SLUMPS to the STM system. Because of this, the Si(111) surface has been severely contaminated, which reduces the image quality. Very

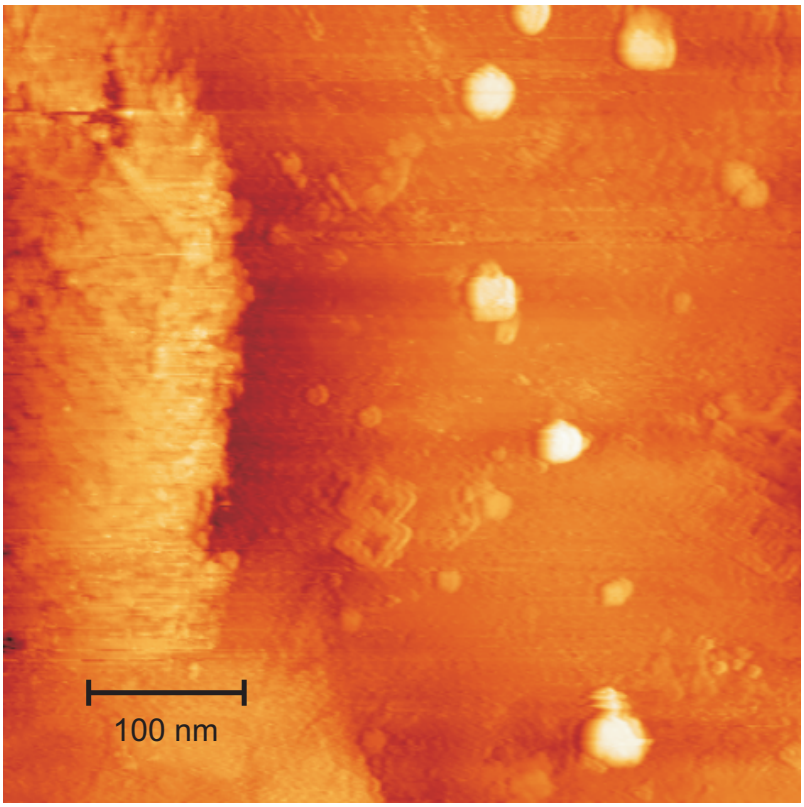

Figure 6.10: STM of a 400 nm × 400 nm area of an 0.8 nm cluster covered surface on Si(111) after exposure to atmosphere. The sample was imaged at 0.1 nA and 2.1 V.

few clusters are apparent on the surface - much fewer than would be expected. It is thought that the STM tip may push the clusters around on the surface. This has been witnessed in previous unpublished STM studies of Fe clusters on graphite and Si by researchers at the Universities of Leicester and Nottingham.[182] This indicates that clusters are very poorly bound to the substrate, most likely by physisorption.

The few clusters that are apparent in the image have a height:width ratio of almost 1:2, suggesting that they are oblate. These may have suffered from a high energy impact on the surface which has altered their shape. However, as landing energies are less than 0.5 eV per atom, this seems unlikely.[149] It is also expected that these clusters have oxidised on top and around the sides, which would alter the height:width ratio, but not by the amount witnessed. A tip convolution factor will also increase the clusters' apparent size.[192] From the image, it is also evident that there is a significant multiple tip effect, where a cluster may be attached to the STM tip.

A large cluster (∼200 nm) was found on the substrate surface on which to conduct elemental mapping with EDS. The results are shown in figure 6.11.

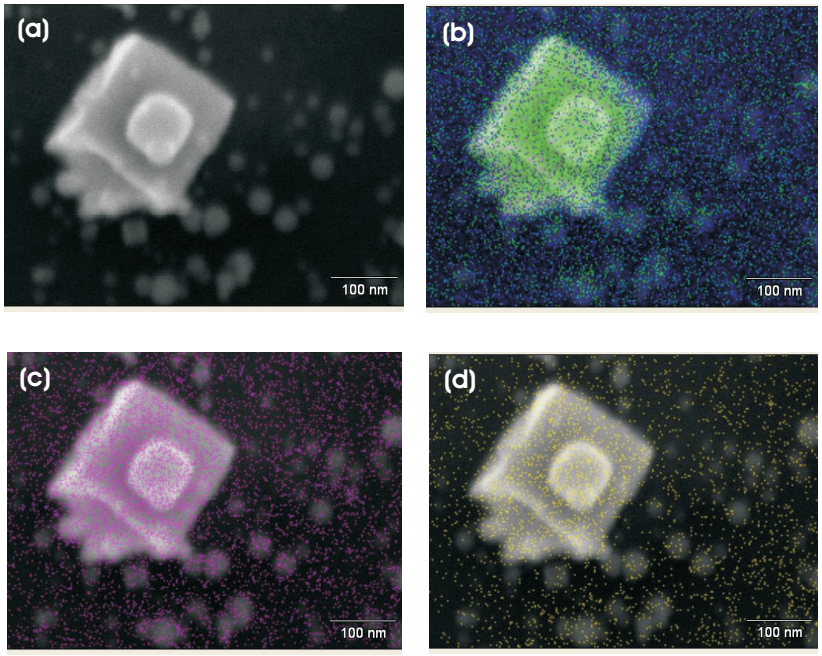

Figure 6.11: EDS of a large cluster deposited on Si(111). (a) is the original secondary electron grey scale image, (b) shows the Fe and Si contributions in green and purple respectively, (c) shows the contribution from O in pink and (d) shows the C contribution in yellow. A 20 keV electron beam was used.

The spatially resolved EDS image shows a high Fe content with a minimal presence of Si on the cluster, which indicates that the entire particle has not formed a silicide on impact. As the sample has been exposed to atmosphere to transport it to the SEM, an oxide layer has formed on both the cluster and the substrate.

6.3.2 MDS

As soon as Fe clusters had been deposited onto the substrate in the preparation chamber, samples were transferred into the analysis chamber where MDS and SPMDS were conducted. Figure 6.12 shows the MDS spectra for the four different cluster coverages on Si(111) shown in figure 6.4, alongside the spectrum for Si(111) 7 $\times$ 7.

As the coverage increases, the overall emission also increases up until the 2.5 nm coverage, where a significant change occurs. The shapes of the spectra do not appear to change from that of the Si(111) 7 $\times$ 7 surface. However, when a 2.5 nm coverage is deposited, the electron emission is significantly reduced and the lower energy electrons are not present at all in the spectrum. In the SEM images, it is apparent, that for the 2.5

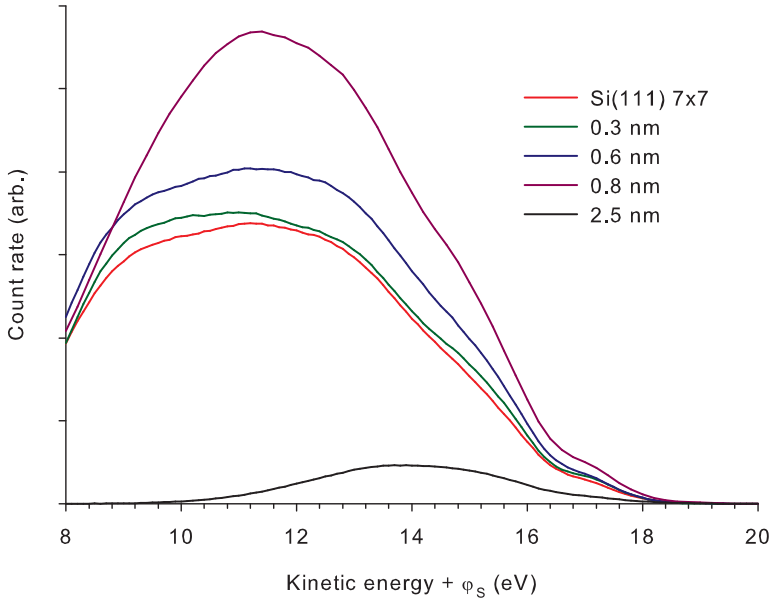

Figure 6.12: MDS spectra for various cluster coverages on the Si(111) surface. The Si(111) 7 × 7 spectrum is shown for comparison.

nm sample, as the coverage is so high, many of the clusters are in contact with one another. This might have the effect of creating long-range magnetic order over the sample, and may thus result in a net magnetic field. If sufficiently great, this would alter the trajectories of the emitted electrons, especially those of low energy, so they may not reach the analyser. For this reason, no further MDS or SPMDS measurements are provided for the 2.5 nm sample.

All the spectra exhibit a gradual decline in electron intensity towards the high kinetic energy cut-off where both electrons in the transition process originate from E_F. This suggests that upon cluster deposition, the de-excitation mechanism remains as RI+AN, as would be expected for a conducting surface such as Fe.[62,193]

The normalised spectra for the same samples, excluding the 2.5 nm one are presented in figure 6.13 to highlight the similarities in feature intensity on different coverage samples. The spectrum emission was normalised at an energy where Si bulk states are thought to dominate.

It is now expected that there will be a superposition of the Si(111) 7 × 7 spectrum and the spectrum arising from the clusters; but as the surface progresses from clean Si to the cluster covered surface, no significant changes are observed in the spectrum. The

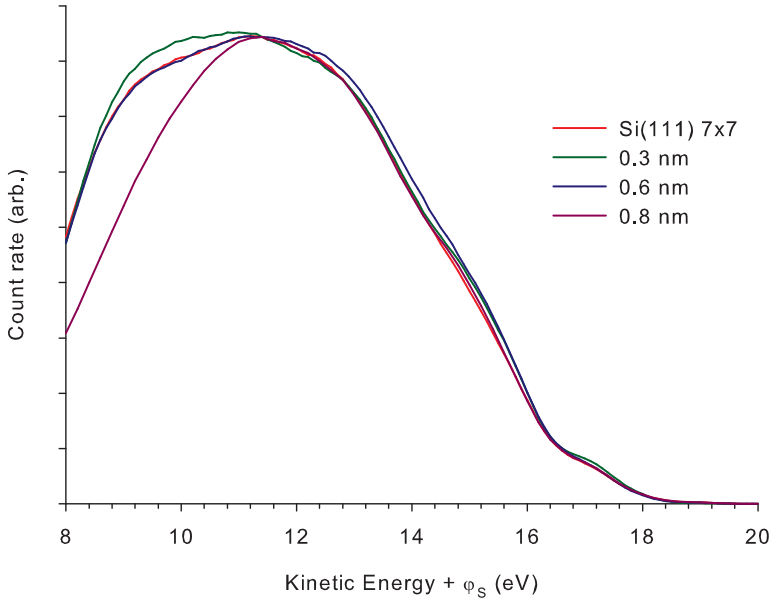

Figure 6.13: Normalised MDS spectra for various cluster coverages on Si(111). The Si(111) 7 $\times$ 7 spectrum is provided for comparison.

difference in the 0.8 nm coverage spectrum at lower energies is the result of changes in the secondary electron count which may be due to a slightly different sample position, or the composition of the sample itself, but either way, this does not appear to effect the spectral features at higher energy.

As the high energy shoulder in the Si(111) 7 $\times$ 7 spectrum at approximately 17.5 eV is known to be due to the Si surface states (see Chapter 5), one would expect this to be the first feature to alter as the surface states are covered by cluster deposition, although this does not appear to be the case. It was decided to deposit clusters on a Si(001) surface in case any features caused by Fe happen to coincide in energy with those of the Si(111) 7 $\times$ 7 features. MDS results for a 0.6 nm coverage on Si(001) and those for the Si(001) 2 $\times$ 1 system are provided in figure 6.14.

It is now evident that by comparing the cluster covered spectrum to that of the clean surface, the clusters are modifying the spectrum. The energies for which the states on the cluster covered Si(001) occur correspond with those seen previously on the Si(111) cluster covered surface, suggesting that the spectral features that occur as a result of cluster deposition are located at the same energies as those for the Si(111) 7 $\times$ 7 spectrum.

It is known from the Fe(001) surface band structure, that *d* states dominate between ap-

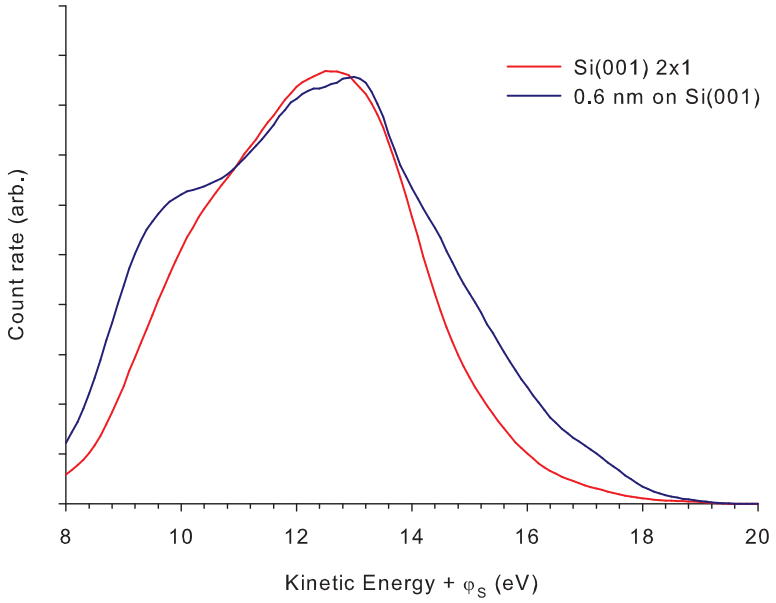

Figure 6.14: MDS of 0.6 nm cluster coverage on Si(001) and of the Si(001) 2 $\times$ 1 surface for comparison.

proximately 0-4 eV relative to E_F.[194,195,196] One might therefore expect the MDS features in this range (approximately 15-19 eV in the MDS spectrum) to result from these states. There may however be exceptions due to the possible contraction of the DOS towards E_F as a result of the reduced co-ordination number of the cluster system. The AN process will also be weighted towards *s-p* states, as even though these have an extremely low DOS at E_F compared to the *d* states, they protrude into the vacuum much further, resulting in a high de-excitation probability.[73,195]

The spectrum of a greater than 30 nm thickness film of bcc Fe(001) on MgO(001) obtained by Yamauchi and Kurahashi[193] is presented as figure 6.15 to demonstrate how different the spectrum is for bulk Fe compared to Fe clusters and also to endeavour to identify features from the cluster-covered spectra.

It is immediately apparent that the shape of the Fe(001) spectrum is quite different to the cluster spectra, exhibiting much broader features. The high energy peak at 16.5 eV is attributed to *d* electronic states and the shoulder at around 11.5 eV is in the energy region where *s-p* states are dominant.[195]

The bulk Fe(001) spectrum has a kinetic energy maximum at about 19 eV which appears to be similar to the cluster covered surface. However, we cannot determine the

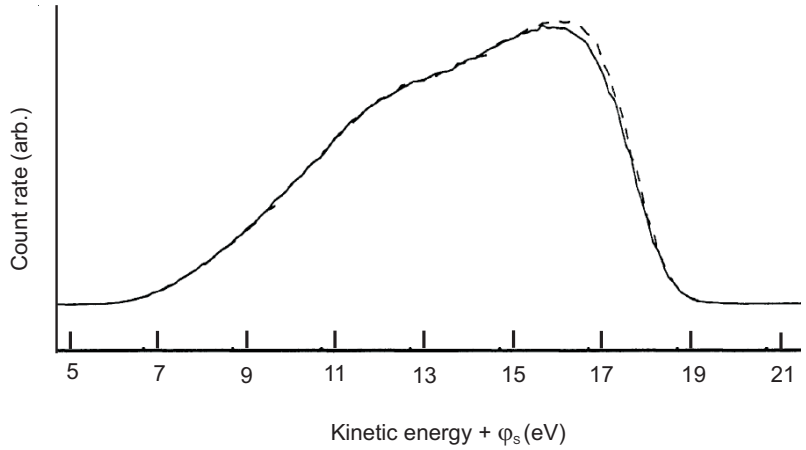

Figure 6.15: MDS spectrum for bulk bcc Fe(001) surface obtained by Yamauchi and Kurahashi.[193] The two different spectra shown (broken and solid lines) are for different incident He polarisations. A work-function of 4.7 eV (that of bulk Fe) has been assumed.

work-function of the clusters alone as any measurement made will not be able to differentiate between the exposed Si and the clusters. Bulk Fe has a work-function of 4.7 eV,[197] but this could well be different in clusters due to size effects. The Si(111) 7×7 surface has a work-function of about 4.55 eV for the doping concentrations used here. As an accurate work-function is necessary for the energy scale conversion in the deconvolution process, in this instance, it has not been performed. However, to determine the approximate *kinetic energies* of the states involved, a differentiation has been performed and is illustrated in figure 6.16 along with the original data for a 0.6 nm cluster coverage on Si(111).

All states indicated in figure 6.16 were present in the differentiated spectra for all investigated coverages at similar energies. Differentiated spectra for the cluster covered and clean Si(001) surface suggest that the two highest energy states indicated in figure 6.16 have contributions from the clusters. The highest energy feature in the cluster covered spectrum occurs at 17 eV. This is at a slightly higher energy than the high-energy feature in the bulk Fe spectrum from the *3d* band electrons.[198,199,200] If there is a contraction of the DOS towards E_F, it would be expected that this *d* band moves closer to the kinetic energy maximum, as seems to be the case.

The effects of the contraction of states around E_F has previously been observed in Fe clusters of 12 nm diameter using X-ray magnetic circular dichroism,[158] and as the clusters investigated in this thesis are of similar size, one would also expect to observe a modification in the DOS here, possibly to a greater extent due to the high proportions of cuboid clusters which have a greater fraction of surface atoms than more spherical geometries.

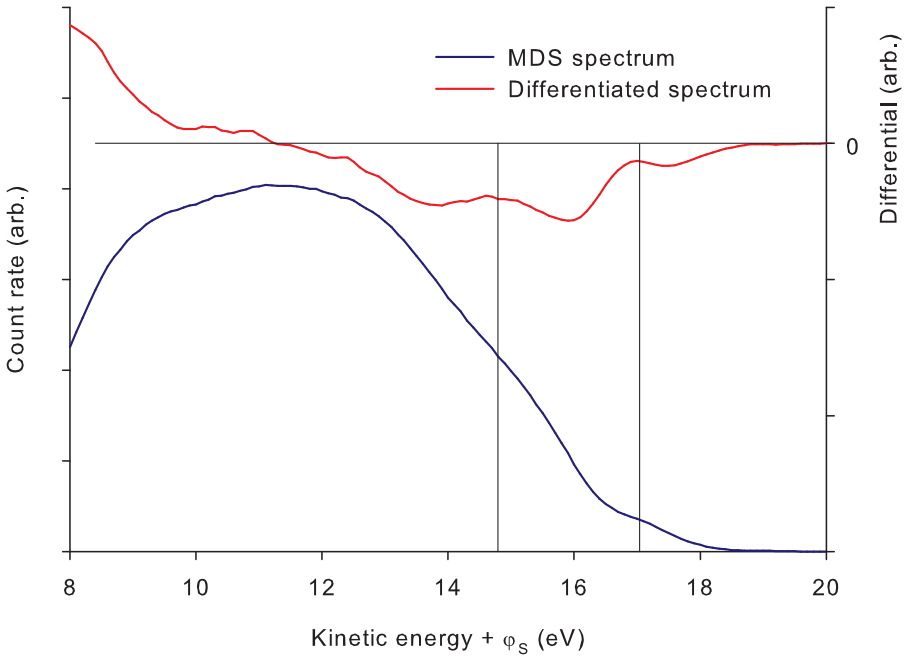

Figure 6.16: MDS and differentiated spectrum of 0.6 nm of clusters deposite on Si(111).

This should result in a lower average number of nearest neighbour atoms and hence a lower coordination number. As we have a distribution of cluster sizes, it is expected that the amount by which the DOS narrows, will also vary across this distribution. This will create broader features than would occur for clusters of a very small size distribution.

The second highest state occurs at 14.6 eV, although no feature is apparent at this energy in the bulk Fe MDS spectrum shown in figure 6.15. As the contraction of the DOS occurs, the density of the states becomes more pronounced (see figure 6.1) which leads to features that are not apparent in a bulk spectrum becoming apparent as the coordination number is decreased. In fact, the calculated DOS for bulk Fe and Fe surfaces, do exhibit a number of smaller peaks due to *d* states at higher binding energies.[194,201] It is also possible that this could be due to *s*-*p* states protruding into the vacuum.[73]

The peak between, 12-13 eV, is the part of the spectrum where bulk states usually begin to dominate. While emission occurs in the bulk Fe spectrum around this energy, attributed to *s*-*p* states,[200] there will be a significant contribution from the *p* states of the exposed Si (as discussed in Chapter 5). All states below this energy will be dominated by bulk states from both the Fe and Si. At even lower energies, secondary electrons will dominate the spectrum.

As there is not thought to be any reaction between the clusters and the surface, it is unlikely that any of the features arise from hybridisations of Fe and Si states. Even if this were to occur, these states would exist on the interface underneath the cluster and would not be expected to appear in the MDS spectrum.

6.3.3 SPMDS, MOKE and AGFM

To conduct SPMDS, the samples were placed between the pole pieces of the *in situ* electromagnet so that the surface normal was perpendicular to the field direction. The magnet was then turned on to produce a field of 280 Oe across the sample. The magnet was turned off and the sample was returned to the position at which MDS was conducted. The helium beam was polarised as described in Chapter 3. Sixteen scans were obtained at alternating He 2^3S polarisations. The spectra for each polarisation were then averaged, and the asymmetry between them calculated using equation 2.13. The polarisation has not, however, been taken into account. A positive asymmetry corresponds to a dominance of the spin minority state.

Spectra of a magnetised sample of 0.8 nm of clusters deposited on Si(111) from the two possible He polarisations as well as the asymmetry between them are illustrated in figure 6.17.

From the graph, it is evident that there is an initial, sharp rise in the asymmetry at about 10.5 eV. This is slightly below the region in which the *d* state asymmetry begins to dominate in the bulk or surface DOS.[194,201] In the SPMDS spectra for Fe(100) and Fe(110) films, an asymmetry does not become apparent until approximately 14.7 eV, at the start of the primary peak.[193,202] Spin polarised photo-emission spectroscopy (SPPES) studies of bcc Fe do however indicate a fairly constant asymmetry at higher binding energies (between 5 and 20 eV binding energy) which are still attributed to the *3d* electrons.[203] It is possible that the low energy asymmetry in the SPMDS is caused by the spin splitting of the *s* and *p* bands due to hybridisations with *d* states.[194] This would explain the rapid rise in the asymmetry at a peak in one of these states. The low energy asymmetry may instead be indicative of some contamination on the surface, as Förster *et al.* have shown that the presence of even small amounts of O on the Fe(110) surface can reduce the energy at which the asymmetry first becomes apparent.[204]

At higher kinetic energies, there is a steady rise in the asymmetry as the *d* states be-

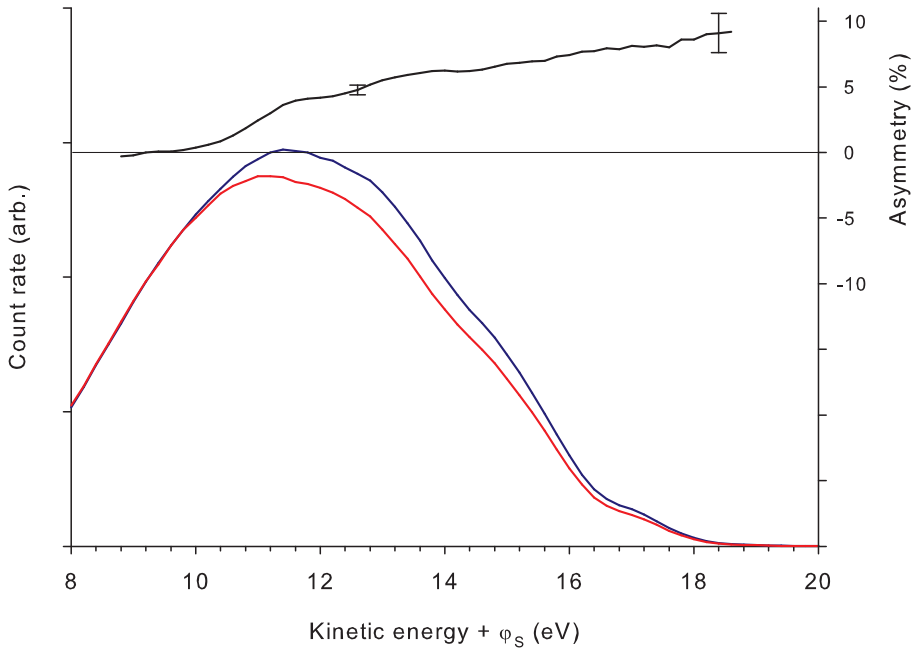

Figure 6.17: Comparison of the two spectra arising from different He* spin polarisations for an 0.8 nm cluster coverage on Si(111) and the associated asymmetry. The asymmetry data have been 3-point smoothed. Error bars are given for one standard error.

come more dominant. It is also possible that if the Si states reduce at a greater rate than the Fe states at higher energy, there will be an increased relative contribution from the Fe *3d* states, which would also cause this rise in asymmetry. As with MDS spectra, the asymmetry is not expected to exhibit sharp features due to the convolution process.

Figure 6.18 shows the asymmetries in the SPMDS spectra for three different cluster coverages on a Si(111) substrate. The asymmetry graph for the Si(111) 7 $\times$ 7 surface is displayed for reference.

As mentioned previously, if RI+AN is occurring on the surface, the asymmetry from SPMDS will not be a true reflection of the asymmetry in the spin-split DOS due to a convolution of the spin states. Also, as *s-p* states penetrate further into the vacuum than the *d* states, they provide a relatively large contribution to the AN process, which will have the effect of reducing the overall asymmetry if these states have a lower asymmetry in their spin-split DOS than the *d* states.[195,73]

The asymmetry of the Si(111) 7 $\times$ 7 spectrum is insignificant, as would be expected, but has fairly large standard errors towards E_F due to the low count rate. On the 0.3 nm

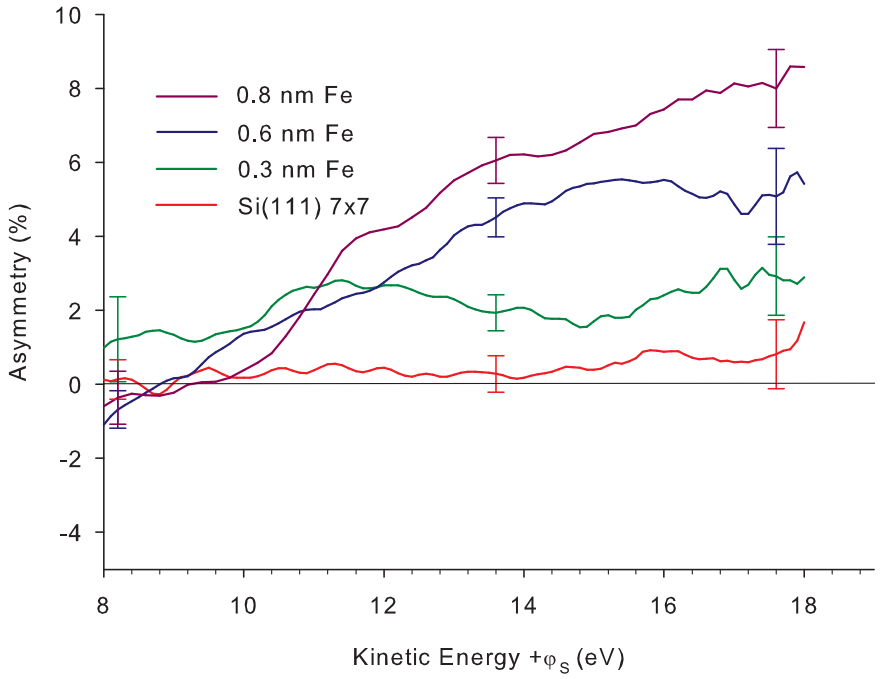

Figure 6.18: Asymmetry in the SPMDS spectra for various coverages of Fe clusters on Si(111). Data have been 3-point smoothed. Error bars provided are for one standard error.

sample, there appears to be an asymmetry in the spectrum even as low as 8 eV; however, the error bars are also quite large at this energy, so this may not be significant. A later rise occurs between 6 and 7 eV which corresponds to the main peak in the MDS spectrum. The asymmetry then reduces again towards where the *d* states dominate in the spectrum, before increasing again towards the kinetic energy maximum, as would be expected. At an energy of 18.0 eV the asymmetry is 2.9 %. For an Fe(001) film at this energy, a typical asymmetry is 4 % which increases with an almost linear rise in energy.[193]

The 0.6 and 0.8 nm coverages display a fairly linear increase in asymmetry with energy. The asymmetry shape is however, slightly different to that of the 0.3 nm sample. This is unusual as the same states should be present for all these coverages, just to different extents. This suggests that any structure within the asymmetries may not be significant. The asymmetries for the 0.6 and 0.8 nm samples towards the kinetic energy maximum at 18 eV are 5.4 % and 8.6 %. These maximum asymmetries seem to increase in an approximately linear way with coverage as is shown in figure 6.19.

This rise in asymmetry is to be expected, as for lower coverages, much of the signal will arise from the spin-symmetric states of the Si, and their contribution will reduce

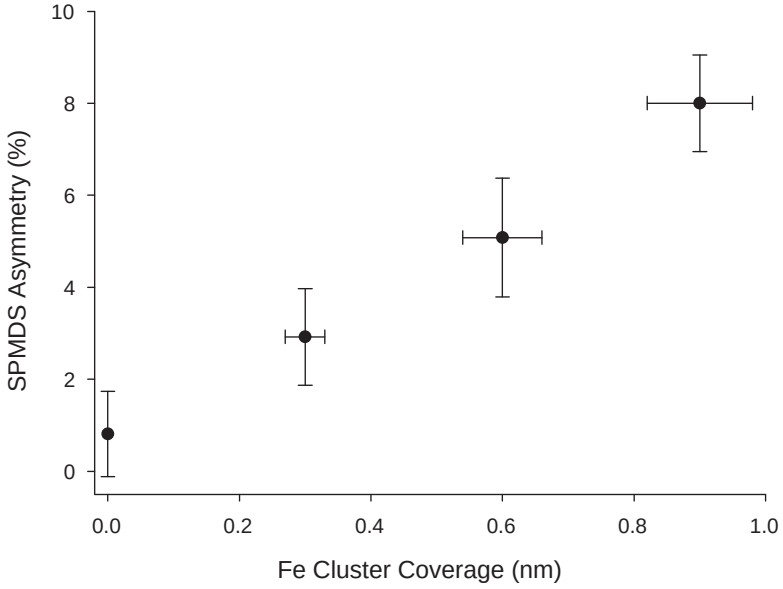

Figure 6.19: Graph of cluster coverage against SPMDS asymmetry at 18 eV. There is an approximately linear rise in asymmetry with cluster coverage.

the observed asymmetry. This linear trend cannot however be extrapolated to very high coverages, as inter-particle interactions will become significant, and so the asymmetry would then reduce to the bulk value.[158] Even so, the areal asymmetry observed for the 0.8 nm coverage is much higher than for a bulk Fe surface ((47.9 $\pm$ 8.4) % at 18.0 eV for the clusters compared with 4 % for the bulk surface).[193] Thin Fe films have previously been reported to give asymmetry values higher than those of the bulk, with thin films of Fe deposited on W(110) and MgO(100) exhibiting asymmetries of up to 24 % and 9% respectively.[204,205] Again, the areal asymmetry for Fe clusters is also greater than the areal asymmetries for these surfaces. It should be noted that values for areal asymmetries assume that all the clusters contribute to the asymmetry, which is not expected to be the case for any clusters that are superparamagnetic.

Oxygen Exposure

After the asymmetry was measured for the 0.3 nm cluster coverage on Si(111), O_2 was admitted into the chamber at a pressure of 1.3×10^{-6} mbar for 20 seconds, to give an exposure to the sample of 20 Langmuir (L). MDS and SPMDS were conducted again, and the asymmetry was calculated. The MDS spectra before and after O_2 exposure are shown in figure 6.20 along with the differentiated spectrum for the O_2 exposed sample.

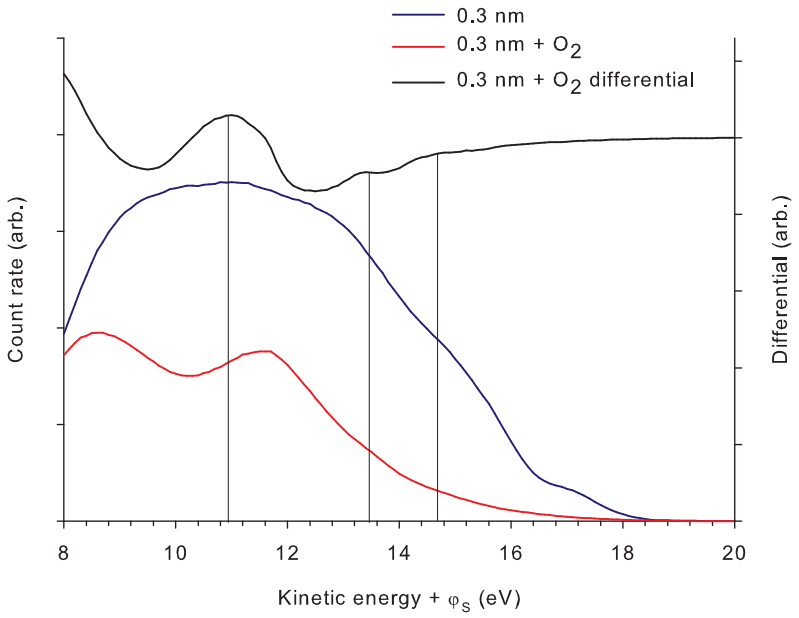

Figure 6.20: The modification of the MDS spectrum of 0.3 nm clusters on Si(111) upon exposure to 20 L of O_2. The differentiated spectrum of the O_2 exposed sample is also shown.

The spectrum shape changes enormously as a result of oxygen exposure. There is a very large reduction in the electron count rate over much of the spectrum. As with the unexposed surface, the electron count diminishes gradually towards E_F indicating that RI+AN is still the dominant de-excitation process. This observation corresponds with oxidation on Fe films.[73,193,196,204,206] Previous results for SiO_x however, reveal the de-excitation mechanism to change to AD, but such samples were prepared under much greater oxygen exposures and at elevated temperatures.[207] Although some oxidation of the Si will have occurred, it does not seem enough to alter the de-excitation mechanism noticeably; but it is possible that there is a limited amount of AD occurring on the surface.

There are now two peaks in the spectrum at 8.6 and 11.5 eV. The spectrum also exhibits a very drawn out high-energy tail, which the differentiated spectrum indicates arises from at least two other possible features in the DOS. Spectra of high O_2 exposures on Fe(100) films indicate a peak at around 9 eV (kinetic energy) and another between 7 and 5 eV (kinetic energy) depending on the oxygen exposure.[193] The latter is attributed to the AN process where one electron involved in the transition originates from the Fe 3*d* state close to E_F and the other is from an O band. It is thought that this is the source of the peak observed at 11.5 eV in our spectrum. An oxygen peak arising from the *2p* band centred at 6 eV binding energy is thought to cause emission in the high-energy tail of the MDS

spectrum.[208] Previous MDS spectra on the SiO_x surface also reveal a peak at 7 eV as well as one at 4 eV, both due to O *2p* states.[207] The oxide reported was formed through much higher sample exposures whilst holding the sample at 900 °C, and so is likely to be a very different stoichiometry to the oxide formed in our oxidation procedure (i.e. closer to SiO_2). The oxide presence on the Si may, however explain the peak at 8.6 eV which does not occur in the oxidised Fe film spectrum.

Figure 6.21 shows the SPMDS asymmetry graphs for 0.3 nm of clusters on Si(111) before and after exposure to 20 L of O_2.

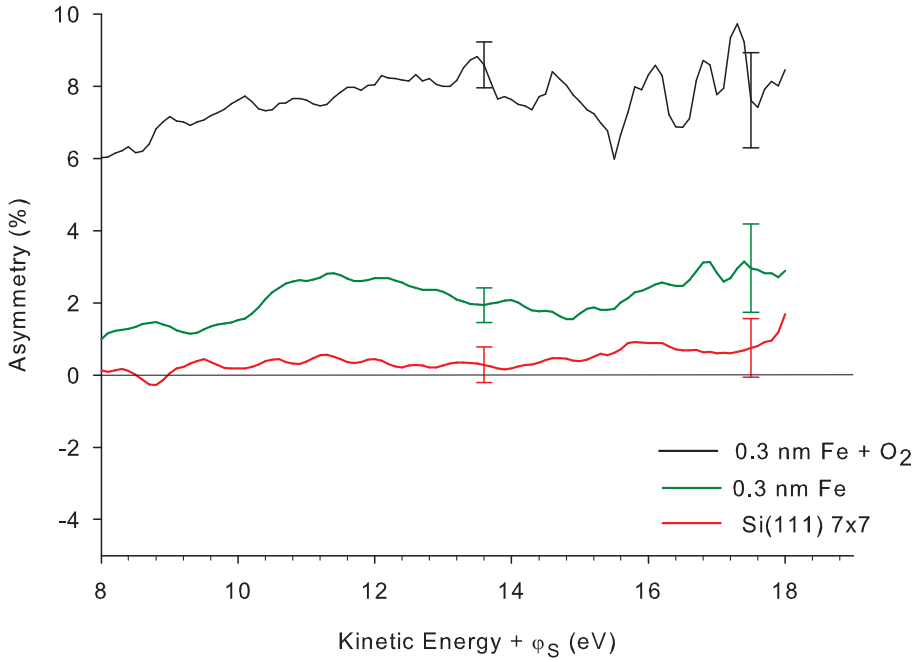

Figure 6.21: Change in the SPMDS asymmetry upon the reaction of Fe with O_2. Error bars shown are for one standard error. Data have been 3-point smoothed.

A noticeable increase in the asymmetry upon oxygen exposure has occurred, changing from (2.9 ± 1.8) % at 17.5 eV on the unexposed surface to (8.5 ± 2.6) % at 18.0 eV. The overall shape of the asymmetry appears similar.

There are two reasons why the calculated asymmetry might increase upon oxygen exposure: The first is that the de-excitation mechanism of the clusters may change from the two-stage RI+AN to AD. In the two-stage process, as discussed in Chapter 2, the asymmetry in the electron counts from different incoming He polarisations does not completely reflect the asymmetry in the SDOS, being reduced by the presence of the other spin states, as while the neutralising electron must originate from the opposite spin state to that of the

approaching He ion, the emitted electron may originate from either spin state in the surface. However, in the case of AD, the electron that tunnels from the surface to the He, must be of the opposing spin state, and so the asymmetry from SPMDS is a true reflection of the asymmetry in the SDOS. This would lead to a greater asymmetry in SPMDS for AD than for RI+AN, even for the same asymmetry in the SDOS. However, as discussed previously, from the MDS spectrum, there is no evidence of a change in de-excitation mechanism. The other possibility is that the asymmetry in the SDOS does increase upon oxygen exposure which would also be reflected in an increase in the SPMDS asymmetry, even if the de-excitation mechanism remained as RI+AN. Previously, on the Fe(110) surface, upon the exposure to 16 L of O_2, the asymmetry was seen to shrink and also reverse over some parts of the spectrum compared to the clean surface.[73] Yamauchi and Kurahashi also witnessed a reversal in asymmetry upon O_2 exposure on 30 nm Fe films grown on MgO(100).[193] The magnitude of the asymmetry at E_F was reduced to almost zero upon O_2 exposures of 20 L. A reversal in asymmetry relative to the clean surface occurs at approximately 11-14 eV. It is suggested that the presence of the asymmetry in the high exposure cases is due to the formation of Fe_3O_4, however in all these studies, the stoichiometry and phase of the iron oxide was not actually investigated.[44]

Kurahashi *et al.* have noted that the Fe/O_2 system occurs in three regimes for different O_2 exposures on Fe films.[206] At low exposures (0-3 L), dissociative chemisorption of the O occurs which results in a reversal in the sign of the asymmetry relative to that of the Fe surface. In the region of 3-20 L exposure, oxygen incorporation occurs, and finally, at exposures of greater than 20 L, a 3D oxide forms and the asymmetry reverses back to that seen on the clean Fe surface with a similar magnitude. Measurements suggest that the phase of this oxide is Fe_3O_4. These results indicate that the clusters may be coated in a 3D oxide after 20 L exposure to O_2, possibly of the Fe_3O_4 phase, which would explain why the asymmetry has not reversed in sign compared to the clean cluster surface.

In fact, if large amounts of Fe_3O_4 were present on the surface, we would expect a much greater asymmetry than on the Fe surface as the oxide has been predicted to be half metallic.[209] A polarisation of approximately 80% has been demonstrated at E_F using spin resolved photoelectron spectroscopy.[210] When we consider the areal density of the clusters, the asymmetry observed is even greater than this, and even without considering the areal density, it is still greater than the SPMDS asymmetry noted for the Fe_3O_4 surface.[206]

The SPMDS asymmetry is fairly constant across the energy range, only falling off at

low energies. This differs from the SPMDS asymmetry observed for the Fe_3O_4 surface, which sees a steep incline towards the kinetic energy maximum, but as the film and cluster MDS surfaces exhibit different features, it is not too surprising that the asymmetries also differ.

The SPMDS asymmetry is present across the regions of the spectrum previously attributed to the Fe $3d$ and O $2p$ states, suggesting a spin splitting of both bands. Hammond *et al.* have previously witnessed a spin-split O *2p* band at -6 eV on an O/Fe(110) film.[73]

AGFM and MOKE Bulk Measurements

Once the samples had been removed from the chamber, AGFM was conducted on them to determine the clusters' bulk magnetic properties. Figure 6.22 shows the hysteresis loops for the four cluster coverages upon which SEM has been performed.

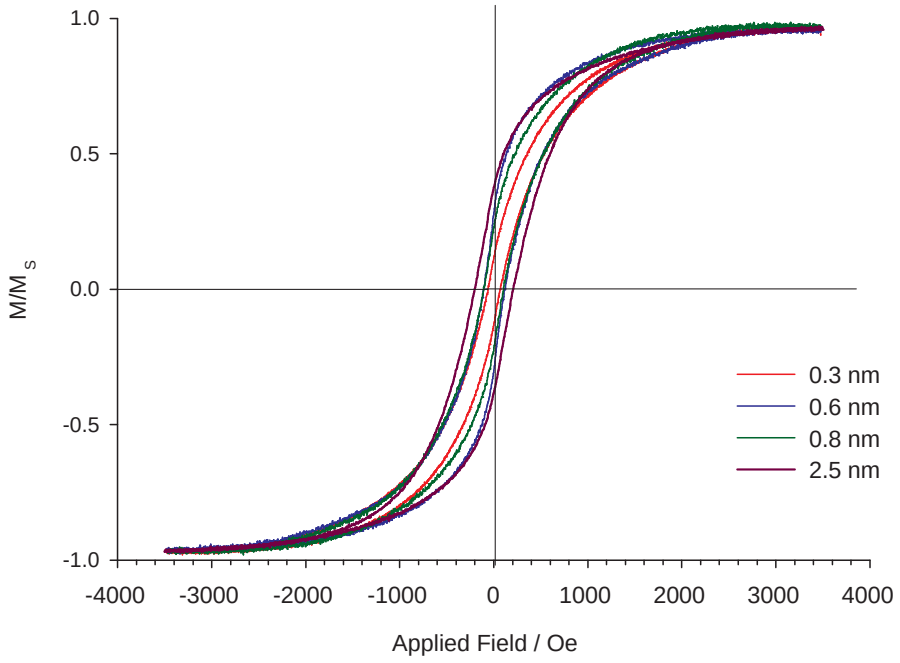

Figure 6.22: Hysteresis loops obtained at room temperature for various cluster coverages on Si(111) obtained with AGFM. The loops have been normalised to the saturation magnetisations.

The three lowest coverage samples all have very similar coercivities between 80 and 90 Oe. As the coercivity is caused predominantly by shape anisotropy, this is expected, as clusters on these samples should be of similar shapes, and for these coverages, interactions

between clusters are limited. The 2.5 nm sample has a significantly greater coercivity of approximately 220 Oe. By this coverage, there are many clusters in contact with one another. This will modify both the switching field distribution and the coercivity of the sample as both the effective shapes and sizes of the clusters are altered.

Clusters on a sample will have a range of shapes and sizes which leads to a range of switching fields and will cause the loops to be less square, as the applied field at which a moment becomes aligned with the applied field will vary with cluster shape and size. Differences with the squareness of the loops are visible. There may be a trend towards squarer loops with increasing coverage, but the 0.8 nm sample appears to be an exception to this. Again, cluster interaction with increasing coverage will alter the switching field distribution and hence the squareness of the loops.

Loops over wider field ranges suggest a further paramagnetic contribution at fields greater than those needed to saturate the ferromagnetic clusters. This contribution will arise from the very small clusters that are not blocked and so are superparamagnetic. Magnetisation saturation occurs in all samples in the region of 5-10 kOe.

What is abundantly clear is that by magnetising the samples at only 280 Oe in the chamber using the *in situ* magnet, the samples would not have been anywhere near their remanence magnetisation once the applied field had been removed. This will also reduce the asymmetry in the DOS and hence the asymmetry observed in the SPMDS spectrum, from the potential maximum.

As most clusters are expected to be single domain particles, the change in magnetisation within a cluster is going to be purely from domain rotation. For uniaxial, single domain particles with randomly orientated easy axes in three dimensions it is expected that $M_r/M_s = 0.5$ for blocked systems,[165] where M_r is the remanent magnetisation and M_s is the saturation magnetisation. For cubic anisotropy, this fraction increases to 0.82.[149] In a system also containing unblocked particles, this ratio will decrease, and reach zero when all particles are superparamagnetic.

For the 0.3 nm sample, $M_r/M_s \approx 0.1$. This figure suggests that a large proportion of the clusters in our sample are unblocked at room temperature contributing to superparamagnetic behaviour. This corresponds with previous results which suggest that for Fe clusters produced in a similar fashion, those smaller than around 15 nm are superparamagnetic.[178]

Hysteresis measurements were repeated some weeks later, and the coercivity was found to have reduced by around 30 Oe for the 0.6 nm and 0.8 nm samples and 10 Oe for the 0.3 nm sample. As it is known from the TEM experiments, Fe_3O_4 forms upon exposure to atmosphere, creating a shell around the Fe cluster. It is unlikely that the core of the cluster is also oxidising to this stoichiometry as the coercivity of bulk Fe_3O_4 is greater than that of bulk Fe (115-150 Oe for Fe_3O_4 compared to 80 Oe for Fe).[211,212] It is possible that the surface and core are further oxidising to one of the phases of Fe_2O_3 such as the α phase (haematite), which is weakly ferromagnetic at room temperature and has previously been shown in nanoparticle form to have a coercivity of 40 Oe.[213] Oxidation from Fe_3O_4 to Fe_2O_3 has previously been observed at room temperature in the presence of oxygen.[214] This process is likely to be accelerated in nanoclusters with their high surface to bulk ratio

SEM images were taken again at a later date, but no increase in cluster size was detectable, although it is likely that any size increase due to oxidation would be in the order of angstroms and so would not be apparent.

Although *in situ* MOKE was attempted on the samples and hysteresis was observed as shown in figure 6.23, it is clear that the fields that can be generated within the chamber (up to 400 Oe) are nowhere near large enough to saturate the samples, and that even at this high coverage, the resolution of the detector is not high enough.

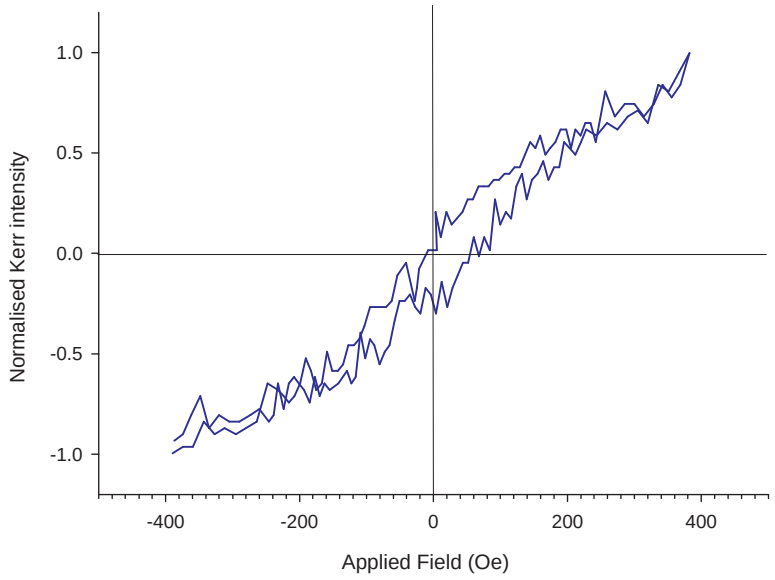

Figure 6.23: Hystereris graph of 2.5 nm of clusters deposited on Si(111) obtained with MOKE. The graph shown is averaged over 23 loops.

The remanence of the hysteresis loop is negligible, which seems to contradict the existence of the SPMDS asymmetry for even lower coverages which have been exposed to the same field strength. However, it is known that a high frequency noise exists on the amplifier used in MOKE which provides the magnetic field to the *in situ* magnet. The magnitude of this noise is enough to cause an alternating field of approximately 30 Oe peak to peak on top of the dc signal. This will have a demagnetising effect on the sample and will hence reduce the observed remanent value. For SPMDS, the samples were magnetised with the same magnet, but connected to a stable dc power supply.

By knowing the remanence of the sample that exists after magnetisation in the chamber, and the maximum remanence, after the sample has been magnetised at the saturation magnetisation, it would be possible to correct the SPMDS asymmetry for the fact that the sample is not saturated by the magnet *in situ*.

After these experiments were conducted, it was deemed necessary to change some components on both the sample preparation and analysis chambers. After this was done, the chamber was re-baked, but no further SPMDS asymmetries could be detected. Clusters produced in the source were analysed with SEM and AGFM, but were not found to have altered magnetic or structural properties. The Stern-Gerlach analyser was reattached to the beam line to investigate whether the He beam was still polarised. It was not found to have altered significantly. The magnetic field strength was also checked and found not to have altered. It is therefore thought that the inability to detect an asymmetry is caused by sample contamination, and although the base pressure of the chambers has not increased, there may now be a new or increased proportion of a particular contaminant in at least one of the chambers. Work conducted by Sun *et al.* on the Fe(110) surface show that exposure to 1 L of CO reduces the asymmetry seen in SPMDS, but for higher coverages of CO, the asymmetry increases again. It is conceivable that for even smaller doses of CO, the asymmetry observed is further reduced.[202] The presence of water on Fe films has also previously been shown to significantly reduce the asymmetry observed in SPMDS.[44]

As no further progress could be made on investigating the surface magnetic properties of clusters, it was decided to conduct an investigation on the effects of annealing clusters on substrates.

6.3.4 Effects of Cluster Annealing

It was decided to anneal the cluster covered samples to see if any reaction would occur between the substrate and the nanoclusters, or whether any change in cluster morphology would result.

Clusters of varying coverages were deposited onto Si(001), and MDS spectra were obtained. The samples were then annealed at various temperatures for 15 mins and allowed to cool to room temperature before more MDS measurements were taken. The samples were then removed from the vacuum system and investigated with SEM and AGFM.

Figure 6.24 shows SEM images of the cluster covered surface before and after annealing at different temperatures.

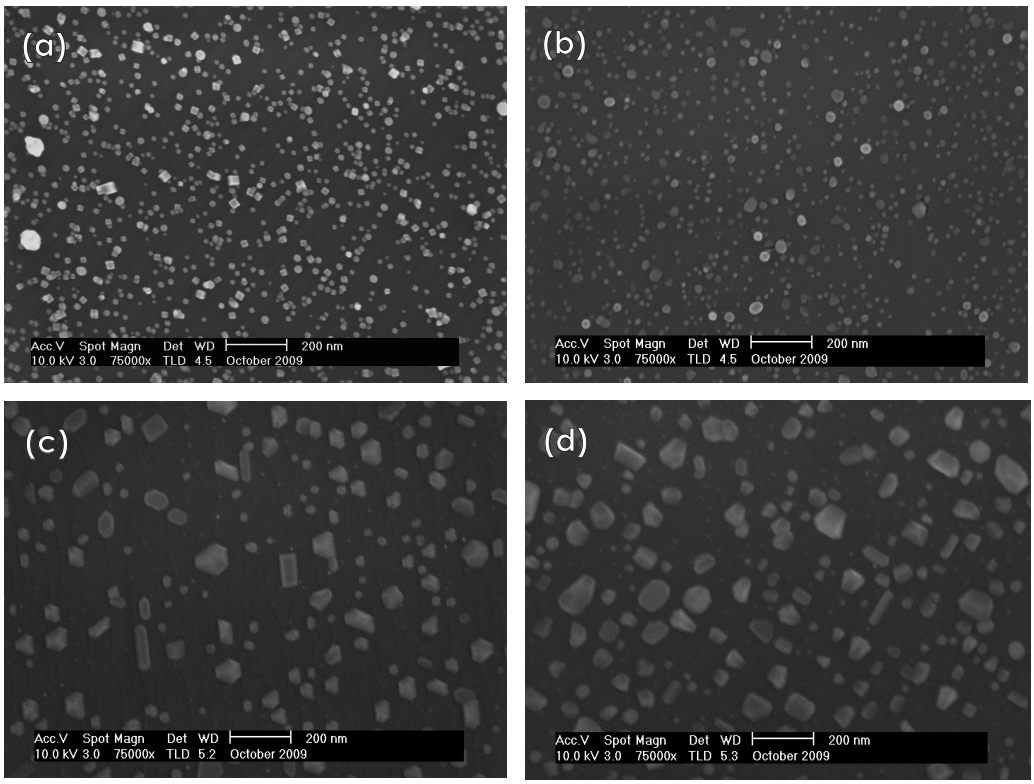

Figure 6.24: SEM images obtained for a 10 kV beam energy of (a) 0.8 nm of clusters deposited onto Si(111), (b), the same coverage annealed for 15 minutes at 500 °C (c) shows a 2.5 nm cluster coverage on the Si(111) surface after a 15 minute anneal at 800 °C and (d) shows a 4 nm cluster coverage on the Si(001) surface after an 800 °C anneal for 15 minutes.

From figure 6.24 it is apparent that before annealing, there are a large proportion of cubic clusters on the surface. After annealing for 15 minutes at 500 °C, no cubic clusters appear to remain. This could be due to the clusters reacting with the Si and forming iron

silicide ($FeSi_x$), or that the clusters are assuming a more energetically favourable geometry by faceting.

When the samples have been annealed to 800 °C the surface appears markedly different. The number of particles on the surface has reduced, but the size of the particles is greatly increased and they appear orientated relative to each other on the substrate. In figure 6.24(c) on the Si(111) surface, the orientation occurs along axes at 120° to one another, whereas on the Si(001) surface in figure 6.24(d), these axes of orientation are at 90° to one another. This suggests that the particles are epitaxially formed on the substrate and are aligned with the substrates' crystal direction. From these images it is also apparent that the particles occur in many, heavily faceted shapes. This apparent size increase is either due to the clusters increasing in volume by reacting with the substrate, or remaining the same volume and spreading out across the substrate. Clusters in the two 800 °C annealed samples appear darker than the unannealed one. This is likely to be due to the decrease in the clusters average atomic number as a silicide is formed. It is also possible that upon annealing, the island thickness becomes more uniform, resulting in a similar number of backscattered electrons across different islands.

EDS was conducted on a sample of 4 nm cluster coverage on Si(111) annealed to 800 °C. The spectral image is presented in figure 6.25.

The EDS images suggest that the bright features on the surface contain Fe to a higher extent than the background, but also contain less Si than the background. As the resolution from a 3.5 kV beam is $\sim$ 40 nm for Fe and $\sim$ 80 nm for Si (as calculated by Win X-Ray), it is impossible to say whether there is Si within the bright features, or likewise, if there is Fe within the surrounding areas. If the clusters have formed an Fe silicide, it is expected that the proportion of x-rays generated from Si within the clusters would be reduced compared to the substrate anyway. EDS does not therefore provide conclusive evidence to whether a silicide has formed. It is apparent that the bright features are oxidised to a greater extent than the background.

If an iron silicide does form at any point, there are many possible stoichiometries that it could assume. The $FeSi_x$ system is a very complex one where many different stable and metastable phases may co-exist after formation under the same conditions on the same sample.[215,216] Of these, ϵ-FeSi, α-$FeSi_2$ and γ-$FeSi_2$ are metallic while β-$FeSi_2$ and Fe_3Si are semiconducting, where the latter is also ferromagnetic. As yet, there are no reports on

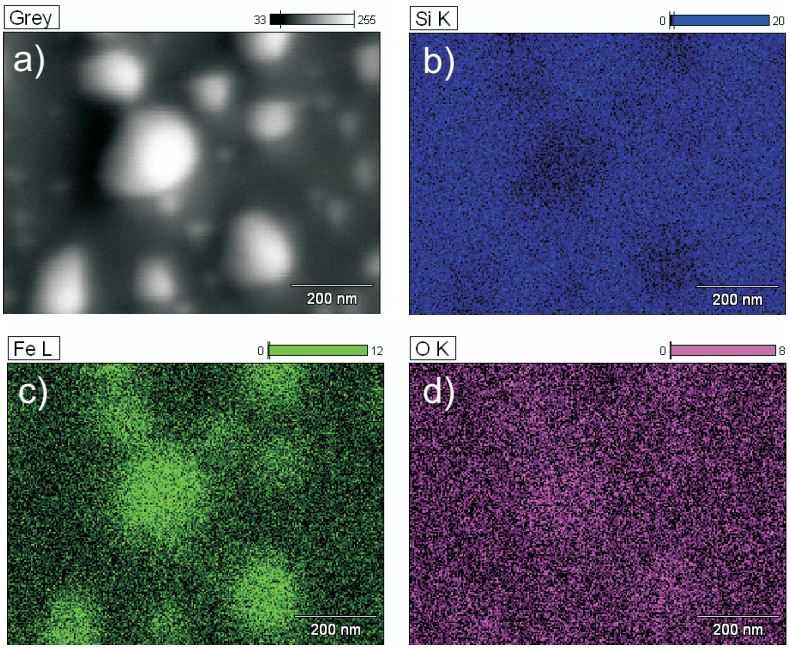

Figure 6.25: EDS images of 4 nm of clusters on Si(111) annealed at 800 °C. Image a) shows the greyscale image, b) shows the Si contribution in blue, c) the Fe contribution in green and d) the O contribution in pink. A 3.5 kV beam was used for EDS.

annealing Fe clusters on a Si substrate. Annealing thin films of Fe deposited on a Si(001) surface at 500 °C has been seen to produce many coexistent phases or completely β-$FeSi_2$, depending on the coverage. Annealing at 800 °C produces silicide islands, of the α-$FeSi_2$ stoichiometry.[216] On the Si(111) 7 $\times$ 7 surface, the β phase is also a possibility at 500 °C along with a polycrystalline phase.[215]

Grainsize analysis was conducted on the annealed surface; this time using ImageJ to estimate the average area the clusters occupy. This size distribution is provided as figure 6.26.

Between the unannealed surface and the one annealed to 500 °C, there is little change in the areas the clusters occupy. This suggests that any reactions between the clusters and the substrate either have not occurred or are limited; however after the 800 °C anneal, there is a very big change in cluster size as shown in the SEM image. It is possible that Ostwald ripening is occurring to increase the size of the clusters on the surface upon annealing to 800 °C, however, this size increase could also be entirely due to reaction with Si.

Figure 6.27 shows a more detailed region of a 2.5 nm cluster coverage on Si(111) substrate after a 15 minute anneal at 500 °C.

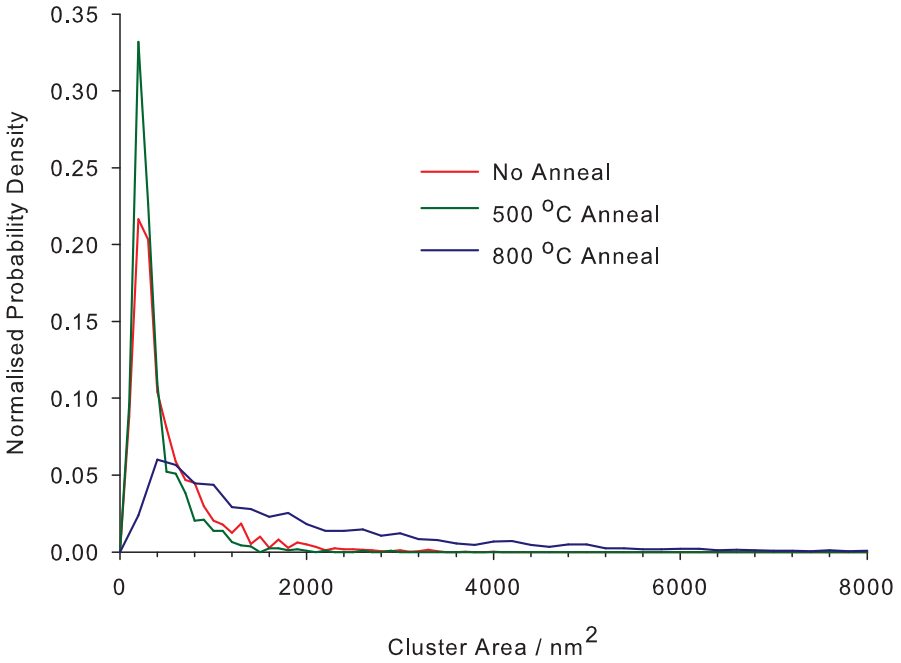

Figure 6.26: Size distribution of 2.5 nm of clusters deposited upon Si(111) after annealing at different temperatures for 15 minutes.

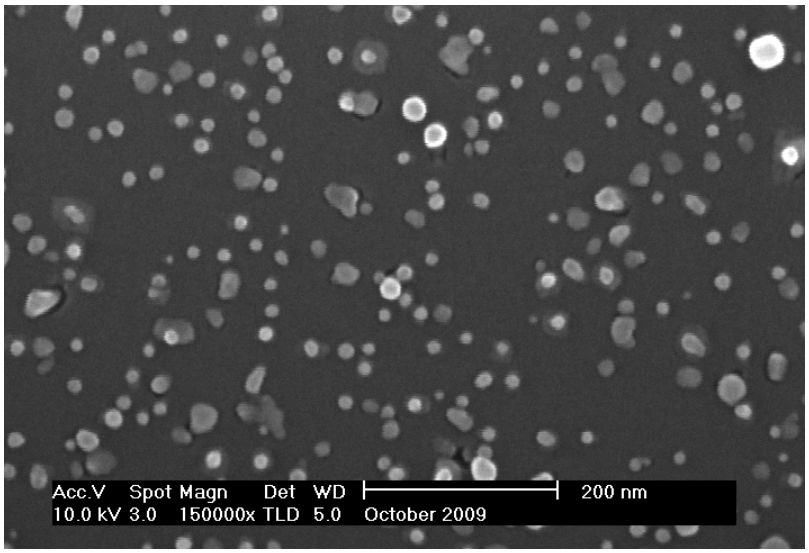

Figure 6.27: SEM image obtained on an 0.8 nm sample of clusters deposited upon Si(111) and annealed at 500 °C for 15 minutes. Dark patches are apparent surrounding some of the clusters.

It is apparent that some of the clusters are situated on top of other, darker, larger and more angular regions. This is likely to be the initial silicide formation where a cluster reacts directly with the substrate underneath it. This is further supported by the existence of holes around the edges of some clusters visible as dark regions on the substrate, where Si has migrated away to form the silicide. It is also apparent that some ordering of crystal orientation is starting to occur in the darker crystalline structures. Such reactions are not apparent in figure 6.24 (c), even though the surface was prepared under the same conditions. This suggests that the annealing temperature of 500 °C is very close to the initial onset of silicide formation.

Figure 6.28 compares MDS spectra obtained after annealing 0.8 nm cluster covered Si(001) surfaces at varying temperatures for 15 mins. The Si(001) 2 × 1 spectrum is displayed for reference.

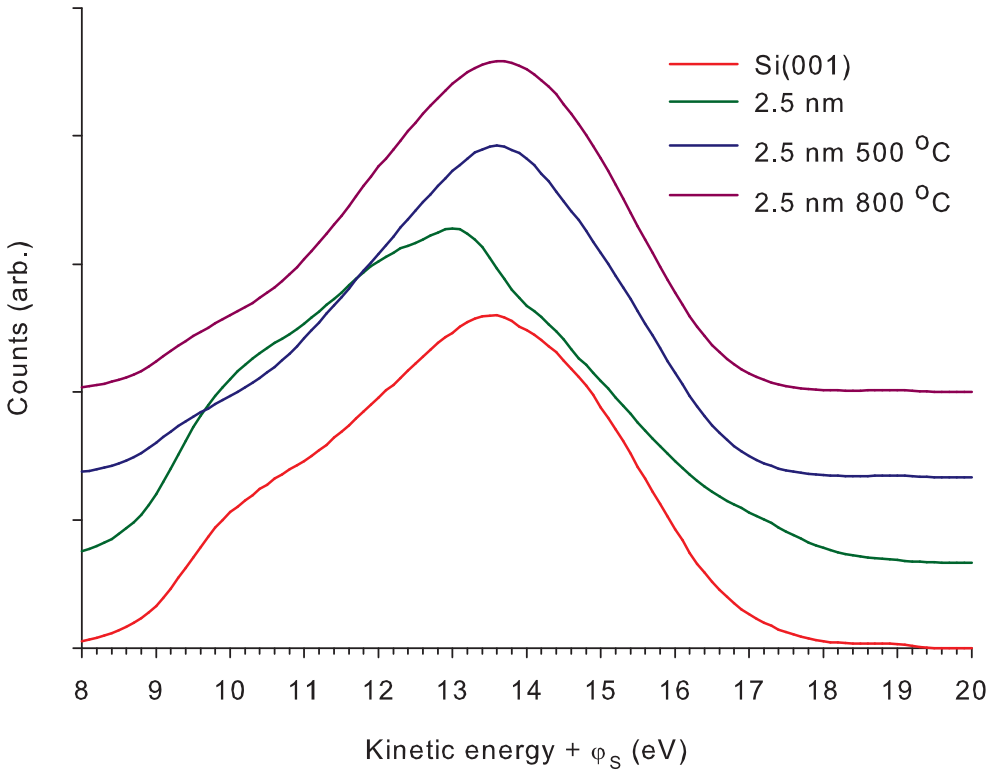

Figure 6.28: MDS spectra of 2.5 nm Fe clusters deposited on Si(001) and annealed at various temperatures for 15 minutes. Spectra have been offset and normalised for clarity.

While the unannealed surface displays the features attributed to cluster deposition, after the anneal to 500 °C, the spectrum appears very similar to that of the clean Si(001)

2×1 surface. By this temperature, SEM indicates that the complete reaction with the substrate has not formed, and it seems as though we still have clusters on the surface. The main difference between the annealed and unannealed clusters apparent in the SEM images is the shape, but although this will affect the electronic structure of the system, it is not thought that this would be very significant when considering the large size distribution of the clusters which would cause a much greater difference in the fraction of surface atoms. It is possible that Si is migrating from the surface and coating the clusters as a precursor to Fe silicide formation. Si migration on the Si(001) surface has already been demonstrated at similar temperatures in Chapter 4. As MDS is so surface sensitive, at higher kinetic energies, where the states arising at the surface of the clusters occur, these would be replaced by electronic states from the Si.

To investigate the bulk magnetic properties of the annealed clusters, samples were removed from the vacuum system and investigated with AGFM.

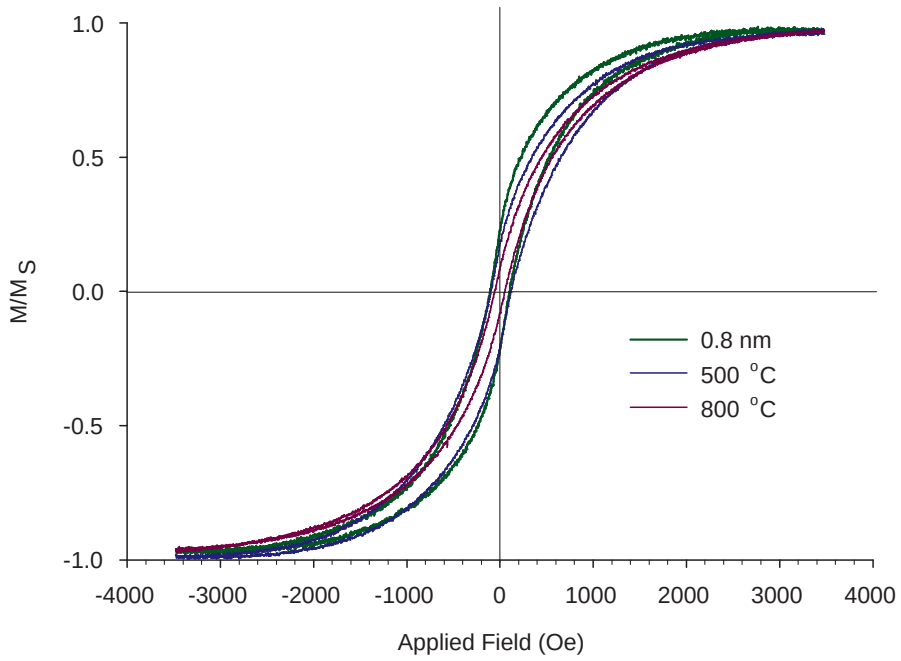

Figure 6.29: Hysteresis loops produced by AGFM of 0.8 nm cluster samples on Si(001) annealed at various temperatures.

After the 500 °C anneal, the coercivity of the loop remains similar to the unannealed sample, but the shape of the hysteresis loop is more elongated. As previously stated, it is thought that shape anisotropy will be the dominant source of anisotropy for the clusters, and as clusters become less cubic as a result of annealing, the clusters will become more

uniaxial. As such, clusters with a hard axis in the direction of the magnetic field will be more difficult to magnetise in that direction, and as a result, the switching field distribution will increase leading to less square hysteresis loops as observed.

After the 800 °C anneal, the coercivity has reduced to 54 Oe and the loop is even more elongated. There is still hysteresis, indicating that the sample is still ferromagnetic. The only ferromagnetic Fe silicides are the iron rich, stable Fe_3Si and the metastable Fe_5Si_3. It is also possible that there is unreacted Fe on the surface, but none was apparent in the SEM images. Such a reduction in the coercivity upon annealing fits with the trend for the conversion from Fe to Fe_3Si. Liew *et al.* has previously grown 46 nm thick Fe_3Si films and observed coercivities of between 1 and 11 Oe depending on the growth conditions used.[217] Fe_5Si_3 has a much greater coercivity of 250 Oe for a film of a similar thickness.[218] This compares with coercivities of 80 Oe for bulk Fe.[211]

6.4 Conclusions

Using SPMDS it has been shown that even for low coverages of Fe nanoclusters on Si substrates, there is a positive asymmetry in the spin-split DOS from the surface of the clusters. The investigation of different cluster coverages has revealed that this asymmetry increases in an approximately linear fashion with the coverage, however this is only expected up until a certain point where inter-particle interactions will become significant. If the areal density of the clusters is taken in to account, the asymmetry appears enhanced when compared to previous studies of Fe films, which suggests, along with a comparison between the MDS spectra of an Fe film and Fe clusters, that there is a narrowing of the DOS that occurs towards the Fermi energy.

SPMDS has also shown that when the cluster-covered surface is exposed to oxygen, the asymmetry in the SPMDS increases. It is thought that an oxide shell of Fe_3O_4 is formed, as this oxide stoichiometry has been determined upon exposure to atmosphere. AGFM measurements suggest that this oxide shell is modified over time.

Size distributions calculated from TEM and SEM images of clusters deposited on TEM grids and Si substrates respectively suggest that the cluster source can produce a bimodal size distribution. This is contrary to theory which suggests that cluster dimensions should assume a log-normal distribution. From SEM images, this seems most prominent for lower

coverages, and might therefore be dependent on the time the source has been operational. SEM and TEM have also been used to show that the cluster source produces a variety of cluster geometries including cuboids and ones which could be truncated rhombic dodecahedral. STM results confirm previous conclusions that upon deposition on Si substrates, only physisorption occurs.

After annealing the clusters deposited on the Si substrate at 800 °C, SEM images suggest that an Fe silicide forms consisting of silicide islands on top of the substrate. AGFM results suggest that this silicide is ferromagnetic with a coercivity reduced from that of the unannealed clusters. This indicates that the silicide may be the Fe rich Fe_3Si stoichiometry.

Chapter 7

Conclusions and Further Work

7.1 General Conclusions

This work has demonstrated the extreme surface sensitivity of MDS and how it may be applied in conjunction with other techniques to fully explore the surface electronic and magnetic properties of a material. The ability to conduct SPMDS with this particular instrument has also been demonstrated on Fe nanoclusters deposited on silicon substrates.

Three different materials systems have been investigated within this thesis, and MDS has been able to provide a new insight into the characteristics of all of them. The main conclusions for these systems are provided hereafter.

7.1.1 Holmium Silicide on Si(001)

The surface reconstructions of Ho silicides formed after less than 1 ML of Ho deposition on Si(001) have been investigated with STM, LEED, MDS and UPS to determine the coverage and temperature conditions favourable for nanowire and surface reconstruction formation as well as the growth modes involved.

It has been shown that the 2×4 reconstruction occurs for nominal coverages of 0.2 - 0.4 ML of Ho when the substrate is held at 500 °C, whereas the 2×7 reconstruction forms at coverages of 0.3 - 0.9 ML under the same temperature conditions. If the temperature during deposition is increased, the upper limit at which the 2×4 reconstruction occurs also increases, as the Ho is more mobile and relocates to form more NWs. This leaves less Ho to form the reconstructions. The formation of these NWs is energetically preferable to

the formation of the reconstructed surface.

The complementary information these techniques provide has indicated that Ho atoms occur on the surface as part of both 2×7 and 2×4 reconstructions. STM has revealed that for NW formation, Si relocates from step edges to react with the RE. The length of NWs is predominantly limited by interactions with NWs forming in a perpendicular direction. A comparison between MDS and UPS reveals how much more surface sensitive the former is, and how, unlike the UPS spectra, there is no contribution from the Ho $4f$ states in the MDS spectra. MDS has also indicated that the electronic properties of both the 2×7 and 2×4 surface reconstructions are very similar.

7.1.2 Holmium Silicide on Si(111)

Two dimensional and 3D RE silicides on Si(111) have been investigated with MDS, LEED, UPS, STM and DFT. The electronic states present within both the UPS and MDS spectra have been discussed. It has been shown using MDS that the surface electronic structure of 2D and 3D RE silicides on Si(111) differs due to changes in the surface Si bi-layer.

An MDS spectral deconvolution technique has been shown to produce an effective surface DOS for the silicide containing three distinct features at high energy. A comparison of the effective DOS and the theoretical DOS calculated with DFT reveal the surface sensitivity of MDS, but also the amount by which some, more bulk-like states can penetrate into the vacuum. Previously, it has been assumed that MDS is a probe of the outermost surface layer of a material,[35] however this result shows that the electronic states present at the surface do not necessarily arise from the surface layer. A layer-resolved theoretical DOS reveals that differences in electronic structure between the 2D and 3D silicide arise from the buckled Si bilayer, possibly due to a change in rumpling amplitude, or the spacing between the RE layer and the bilayer. A DOS based on parameters derived from other experimental techniques is shown to match the deconvoluted MDS better than the DOS based on theoretically derived parameters, possibly as a result of the zero Kelvin assumption that is used in these particular DFT calculations.

A comparison of deconvoluted MDS and a theoretical DOS calculated with DFT reveals that upon exposure to atomic H, there are two H sorption sites per unit cell on the surface of the 2D Ho silicide: one surface site and one interstitial subsurface site. Occu-

pation of these sites is thought to be concomitant.

7.1.3 Iron Nanoclusters

A preliminary study into the electronic, magnetic and structural properties of Fe nanoclusters deposited onto a Si substrate has been conducted using a variety of techniques including MDS and SPMDS.

Whilst the lowest energy cluster geometry has been previously shown to be a truncated rhombic dodecahedron, many cubic clusters with high-energy $\{001\}$ surfaces have been observed. This suggests that for many clusters, growth kinetics and not surface energy is the determining factor of cluster morphology. Size distributions of the deposited clusters have revealed that in some instances, a bimodal distribution may occur.

The MDS spectrum from the Fe cluster covered surface is quite different to the spectrum from bulk or thin-film Fe. It is thought that this is due to the narrowing of the valence bands of the clusters as an effect of their reduced co-ordination number. The electronic states that contribute to the MDS spectra have been discussed.

An asymmetry in the SPMDS spectra has been detected and attributed to the spin-split DOS of the Fe nanoclusters. This asymmetry has been shown to increase with cluster coverage, and is shown to increase dramatically when the clusters are exposed to oxygen. The areal asymmetries before and after oxidation are greater than those for Fe and Fe oxide thin film and bulk surfaces. An increased asymmetry is again indicative of a narrowed valence band.

When exposed to atmosphere, a uniform, epitaxial Fe_3O_4 oxide layer has been shown to occur on one cubic cluster investigated with TEM. Other TEM results suggest that the formation of an oxide shell is common for such clusters. This has potential implications for future medical applications.[178]

Upon annealing the clusters, an Fe silicide is thought to develop consisting of small islands across the Si substrate surface. AGFM results suggest that this silicide is ferromagnetic with a lower coercivity than the cluster covered surface. This suggests that the silicide is of the Fe_3Si stoichiometry.

7.1.4 Instrument Development

A sample preparation chamber with fast-entry lock has been added to the system allowing for the future developments to the system. An *in situ* MOKE has been constructed to be used on the sample analysis chamber so that bulk magnetic properties of a material may be compared to the SPMDS asymmetry. An interlock system has been constructed to protect the beam-line from a range of different potential problems, such as pump malfunction or a break in supply to cooling water.

7.2 Further Work

7.2.1 Instrument and Technique Development

As it has been shown that even small magnetic fields affect the MDS spectrum produced in the current experimental arrangement, it is not possible to conduct SPMDS of samples whilst a magnetic field is applied, or to investigate samples with high magnetisations. To allow such measurements, it is necessary to modify the method of collecting the electron spectrum. This could be done by measuring the current emitted from the sample for different sample biases for different incident He polarisations. Such a technique would allow systems such as nanoclusters to be investigated at saturation.

For samples that require very large applied fields to saturate them, an *in situ* magnet may prove inadequate. An *ex situ* superconducting magnet could be mounted on the outside of the chamber to produce such a field. If the magnet was rotatable around the analysis chamber, this would allow the samples to be magnetised in different directions, and the relationship between magnetisation direction and asymmetry could be investigated.

Currently only a very simple deconvolution method has been used to retrieve the effective DOS, which has the potential to produce spurious features. Many other deconvolution techniques exist based on fitting splines to the experimental data. Such methods should be compared to the current method to investigate whether any significant differences in the results arise.

The MOKE analyser could be made more sensitive by replacing the interface device with one capable of a higher input voltage resolution. Noise on the system seems to be

predominantly caused by the turbo pump on the analysis chamber. If the mounts for the laser and analyser could be dampened or decoupled from the chamber itself, this noise could be reduced, and a higher signal to noise ratio could be achieved.

One of the current drawbacks of MDS is its lack of spatial resolution. The utilisation of laser cooling to collimate and focus the metastable beam has allowed the possibility of metastable de-excitation microscopy. Such a modification would allow the study of the surface electronic properties of individual features on a surface, however further reductions in the metastable beam spot size would be necessary. Current methods of metastable electron emission microscopy flood the entire sample with metastable atoms. In these systems, the resolution is governed by the electron optics of the analyser, and currently have a resolution of approximately 300 nm.[36] The resolution of a metastable microscope which uses a focused metastable spot would ultimately be governed by the aberrations of the focusing optics. Calculations suggest that spot sizes of 10-20 nm are possible.[219]

7.2.2 Future Experiments

In this thesis, MDS of $HoSi_2$ has been conducted. Recent work indicates that whilst depositing Mn directly onto Si leads to a disordered surface, depositing Mn onto a cool $HoSi_2$ surface and then annealing results in a well-ordered Mn layer.[220] If the same could be done with a ferromagnetic material such as Fe or a Heusler alloy, this would lead to the possibility of using such a material as a spin-injector into Si. Investigating these materials with SPMDS would reveal some of the magnetic properties of the overlayers, whilst MDS would provide interesting electronic information.

The work conducted on magnetic Fe nanoclusters has revealed many potential directions of further research:

As it is possible to mass-select clusters from SLUMPS, a natural progression of this work would be to investigate how the MDS spectrum changes with changing cluster size as the coordination number is modified. The magnitude of the SPMDS asymmetry would also be expected to change as a result of cluster size. As even without mass selection, a sizeable proportion of clusters produced in the source are superparamagnetic, a field would need to be applied during the acquisition of SPMDS spectra to ensure magnetisation.

With modifications to the method of spectral acquisition, the SPMDS asymmetry could be investigated at higher cluster coverages to determine the maximum asymmetry achievable, and at what coverage cluster-cluster interactions become significant.

So far, only the effect of a 20 L O_2 exposure on the clusters has been investigated. It is not known whether this is enough to cause complete oxidation. A study of the effects of differing oxygen exposures on the cluster surface would reveal whether the same regimes of reaction occur as on the Fe thin-film surface as noticed by Kurahashi *et al.*[206] Further oxygen exposure may increase the magnitude of the asymmetry, whereas a smaller amount might reverse it.

Kurahashi *et al.* have shown that upon hydrogen exposure, the asymmetry in the SPMDS spectrum of Fe_3O_4 increases to $>50\%$.[221] It would be interesting to H-terminate the clusters and the oxygen exposed clusters to determine whether the asymmetry of the system could be further increased.

TEM and SEM have shown the presence of different cluster morphologies. It would be straightforward to change the Ar pressure in the source and the magnetron power to investigate their relationship with the cluster morphology. This might also provide insight into the origin of the bimodal distribution. The source should also be further characterised to determine whether the length of time the source has been in operation affects the cluster shape and size.

To determine whether the silicide formed upon annealing the clusters is Fe_3Si, quantitive Auger microscopy could be used to check the composition of the islands which would also be able to deduce whether a wetting layer to island growth has occurred on the surface. The structure of the silicide could be investigated using MEIS. The effects of annealing conditions and initial cluster coverage on island size should also be investigated.

As the cluster geometries and size distributions have been characterised, it would be possible to model the bulk magnetic properties of the systems investigated using the methods of Stoner and Wohlfarth,[165] assuming uniaxial, single-domain behaviour where there is no interaction between the clusters. These results could be compared to those obtained experimentally to determine the contribution of surface effects, which are not taken into account by the theory. The proportions of clusters expected to be in a superparamagnetic state could also be approximated using the Néel Arrhenius law (equation 6.1.2).

Recent work conducted in collaboration with the Department of Chemistry on crotyl alcohol deposited on Pd(111) and the Department of Physics and Astronomy at the University of Leicester on C_{60} deposited on Si(111), demonstrates MDS's potential when looking at organic molecular systems. Such a technique can be used to detect states not observable in UPS. There are many potential organic systems that could be investigated in this way.

Bibliography

1. Duke, C. B. *Chem. Rev.* **96**, 1237 (1996).

2. Davisson, C. and Germer, L. H. *Nature* **119**, 558 (1927).

3. Briggs, D. and Seah, M. P., editors. *Practical Surface Analysis*, volume 1. Wiley (Chichester), (1990).

4. Prutton, M. *Introduction to Surface Physics*. Oxford University Press (Oxford), (1994).

5. Kerr, J. *Phil. Mag.* **3**, 321 (1877).

6. Bland, J. and Heinrich, B., editors. *Ultrathin Magnetic Structures*, volume 2, 297. Springer (Berlin) (1994).

7. Akdogan, N., Nefedov, A., Westerholt, K., Zabel, H., Becker, H.-W., Somsen, C., Khaibullin, R., and Tagirov, L. *J. Phys. D: Appl. Phys.* **41**, 165001 (2008).

8. O'Grady, K., Lewis, V. G., and Dickson, D. P. E. *J. Appl. Phys.* **73**, 5608 (1993).

9. Binnig, G. and Rohrer, H. *Phys. Rev. Lett.* **50**, 120 (1986).

10. Knoll, M. *Z. Tech. Phys.* **16**, 467 (1935).

11. Segall, M., Lindan, P., Probert, M., Pickard, C., Hasnip, P., Clark, S., and Payne, M. *J. Phys.: Cond. Mat.* **14**, 2717 (2002).

12. Pratt, A. and Jacka, M. *J. Phys. D: Appl. Phys* **42**, 055308 (2009).

13. Ishii, H., Masuda, S., and Harada, Y. *J. Electron Spectrosc.* **52**, 125 (1971).

14. Thompson, R. D., Tsaur, B. Y., and Tu, K. N. *Appl. Phys. Lett.* **38**, 535 (1981).

15. Baglin, J. E., d'Heurle, F. M., and Petersson, C. S. *Appl. Phys. Lett.* **36**, 594 (1980).

16. Netzer, F. P. *J. Phys.: Condens. Matt.* **7**, 991 (1995).

17. Wood, T. J., Bonet, C., Noakes, T. C. Q., Bailey, P., and Tear, S. P. *Phys. Rev. B* **73**, 235405 (2006).

18. Rogero, C., Martín-Gago, J. A., and Cerdá, J. I. *Phys. Rev. B* **74**, 121404(R) (2006).

19. Saintenoy, S., Wetzel, P., Pirri, C., Bolmont, D., and Gewinner, G. *Surf. Sci.* **349**, 145 (1996).

20. Wetzel, P., Pirri, C., and Gewinner, G. *Europhys. Lett.* **38**, 359 (1997).

21. Preinesburger, C., Vandré, S., Kalka, T., and Dähne-Prietsch, M. *J. Phys. D: Appl. Phys.* **31**, L43 (1998).

22. Bowler, D. R. *J. Phys.: Condens. Mat.* **16**, R721 (2004).

23. Liu, B. Z. and Nogami, J. *Surf. Sci.* **540**, 136 (2003).

24. Weller, D., Alvarado, S. F., Gudat, W., Schroder, K., and Campagna, M. *Phys. Rev. Lett.* **54**, 1555 (1985).

25. Richter, R., Gay, J. G., and Smith, J. R. *Phys. Rev. Lett.* **54**, 2704 (1985).

26. Webb, H. W. *Phys. Rev.* **24**, 113 (1924).

27. Penning, F. *Naturwissenschaften* **15**, 818 (1927).

28. Oliphant, M. L. E. *Proc. Roy. Soc. London A* **124**, 793 (1929).

29. Massey, H. S. W. *Proc. Cambridge Phil. Soc.* **26**, 386 (1930).

30. Cobas, A. and Lamb, W. E. *Phys. Rev.* **65**, 327 (1944).

31. Hagstrum, H. D. *Phys. Rev.* **96**, 325 (1954).

32. Hagstrum, H. D. *Phys. Rev.* **89**, 244 (1953).

33. Hagstrum, H. D. *Phys. Rev.* **91**, 543 (1953).

34. Hagstrum, H. D. *Electron and Ion Spectroscopy of Solids*, 273. Plenum (New York) (1978).

35. Harada, Y., Masuda, S., and Ozaki, H. *Chem. Rev.* **97**, 1897 (1997).

36. Yamamato, S., Masuda, S., Yasufuku, H., Ueno, N., Harada, Y., Ichinokawa, T., Kato, M., and Sakai, Y. *J. Appl. Phys.* **82**, 2954 (1997).

37. Hänsch, T. W. and Schawlow, A. *Opt. Commun.* **13**, 68 (1975).

38. Aspect, A., Vansteenkiste, N., Kaiser, R., Haberland, H., and Karrais, M. *Chem. Phys* **145**, 307 (1990).

39. Pratt, A., Roskoss, A., Menard, H., and Jacka, M. *Rev. Sci. Ins.* **76**, 53102 (2005).

40. Dalfovo, F., Giorgini, S., Pitaevskii, L. P., and Stringari, S. *Rev. Mod. Phys.* **71**, 463 (1999).

41. Rothe, E. W., Neynaber, R. H., and Trujillo, S. M. *J. Chem. Phys.* **42**, 3310 (1965).

42. Swansson, J. A., Baldwin, K. G. H., Hoogerland, M. D., Truscott, A. G., and Buckman, S. J. *App. Phys B* **79**, 485 (2004).

43. Sesselmann, W., Woratschek, B., Küppers, J., Ertl, G., and Haberland, H. *Phys. Rev. B* **35**, 1547 (1987).

44. Kurahashi, M., Sun, X., and Yamauchi, Y. *Surf. Sci.* **601**, 1371 (2007).

45. Masuda, S., Ishii, H., and Harada, Y. *Surf. Sci.* **242**, 400 (1991).

46. Pasquali, L., Nannarone, S., Canepa, M., and Mattera, L. *Phys. Rev. B* **52**, 17335 (1995).

47. Masuda, S., Hayashi, H., and Harada, Y. *Phys. Rev. B* **42**, 3582 (1990).

48. Yasafuku, H., Meguro, K., Akatsuka, S., Setoyama, H., Kera, S., Azuma, Y., Okudaira, K., Hasegawa, S., Harada, Y., and Ueno, N. *Jpn. J. Appl. Phys.* **39**, 1706 (2000).

49. Sesselmann, W., Woratschek, B., Ertl, G., Küppers, J., and Haberland, H. *Surf. Sci.* **146**, 17 (1984).

50. Ozaki, H. and Harada, Y. *J. Am. Chem. Soc* **112**, 5735 (2000).

51. Hagstrum, H. D. and Becker, G. E. *Phys. Rev. B* **4**, 4187 (1971).

52. Mularie, W. and Peria, W. *Surf. Sci.* **26**, 125 (1971).

53. Boiziau, C., Garot, C., Nuvolone, R., and Roussel, J. *Surf. Sci.* **91**, 313 (1980).

54. Tagle, J., Sáez, V., Rojo, J., and Salmerón, M. *Surf. Sci.* **77**, 77 (1978).

55. Stern, W. and Gerlach, O. *Z. Phys* **9**, 353 (1922).

56. Kastler, A. *J. Phys. -Paris* **11**, 255 (1950).

57. Brossel, J., Kastler, A., and Winter, J. *J. Phys et Radium* **13**, 668 (1952).

58. Schearer, L. D. *Adv. Quantum Elec.* **2**, 239 (1961).

59. Riddle, T. W., Onellion, M., Dunning, F. B., and Walters, G. K. *Rev. Sci. Instrum.* **52**, 797 (1981).

60. Keliher, P. J., Dunning, F. B., O'Neill, M. R., Rundel, R. D., and Walters, G. K. *Phys. Rev. A* **11**, 1271 (1975).

61. Onellion, M., Hart, M. W., Dunning, F. B., and Walters, G. K. *Phys. Rev. Lett.* **52**, 380 (1984).

62. Penn, D. R. and Apell, P. *Phys. Rev. B* **41**, 3303 (1990).

63. Eisberg, R. and Resnick, R. *Quantum Physics of Atoms, Molecules, Solids, Nuclei and Particles*. Wiley, (1985).

64. Dunning, F. B. and Hulet, R. G., editors. *Experimental methods in the physical sciences*, volume 29B, 191–215. Academic Press (San Diego) (1996). Atomic, molecular and optical physics: atoms and molecules.

65. Morgner, H. *Advances in Atomic, Molecular, and Optical Physics*, volume 42, 387. Academic Press (New York) (2000).

66. Lu, W., Hoogerland, M. D., Milic, D., Baldwin, K. G. H., and Buckman, S. J. *Rev. Sci. Instrum.* **72**, 2558 (2001).

67. Witte, G. *J. Phys.: Condens. Mat.* **16**, 2937 (2007).

68. Hagstrum, H. D., Takeishi, Y., and Pretzer, D. D. *Phys. Rev.* **139**, A526 (1965).

69. Salmi, L. A. *Phys. Rev. B* **46**, 4180 (1992).

70. Masuda, S., Ishii, H., and Harada, Y. *Solid State Commun.* **82**, 587 (1992).

71. Dunning, F. B., Nordlander, P., and Walters, G. K. *Phys. Rev. B* **44**, 3246 (1991).

72. Appelbaum, J. A. and Hamann, D. R. *Phys. Rev. B* **6**, 1122 (1972).

73. Hammond, M. S. Dunning, F. B. and Walters, G. K. *Phys. Rev. B* **45**, 3674 (1992).

74. Lancaster, J. C., Kontur, F. J., Walters, G. K., and Dunning, F. B. *Phys. Rev. B* **67**, 115413 (2003).

75. Hart, M. W., Hammond, M. S., Dunning, F. B., and Walters, G. K. *Phys. Rev. B* **39**, 5488 (1989).

76. Dunning, F. B., Oro, D. M., Soletsky, P. A., Zhang, X., Nordlander, P., and Walters, G. K. *Z. Phys. D* **30**, 239 (1994).

77. Pratt, A. *A Laser Colled Helium 2^3S Beam for Surface Analysis*. PhD thesis, University of York, (2005).

78. Dose, V., Fauster, T., and Gossmann, H. J. *J. Comput. Phys.* **41**, 34 (1981).

79. Onsgaard, J., Morgen, P., and Creaser, R. *J. Vac. Sci. Technol.* **15**, 44 (1978).

80. Norde, H., de Sousa Pires, J., d'Heurle, F., Pesavento, F., Petersson, S., and Tove, P. A. *Appl. Phys. Lett.* **38**, 865 (1981).

81. Chen, Y., Ohlberg, D. A. A., Medeiros-Ribeiro, G., Chang, Y. A., and Williams, R. S. *Appl. Phys. Lett.* **76**, 4004 (2000).

82. Yeom, H. W., Takeda, S., Rotenberg, E., Matsuda, I., Horikoshi, K., Schaefer, J., Lee, C. M., Kevan, S. D., Ohta, T., Nagao, T., and Hasegawa, S. *Phys. Rev. Lett.* **82**, 4898 (1999).

83. Zeng, C., Kent, P. R. C., Kim, T., Li, A., and Weitering, H. H. *Nat. Mater.* **7**, 539 (2008).

84. Tu, K. N., Thompson, R. D., and Tsaur, B. Y. *Appl. Phys. Lett.* **38**, 626 (1981).

85. Durkan, C. and Wellan, M. E. *Ultramicroscopy* **82**, 125 (2000).

86. Chen, Y., Ohlberg, D. A. A., Li, X., Stewart, D. R., Williams, R. S., Jeppesen, J. O., Nielsen, K. A., Stoddart, J. F., Olynick, D. L., and Anderson, E. *Appl. Phys. Lett.* **82**, 1610 (2003).

87. Collier, C. P., Mattersteig, G., Wong, E. W., Luo, Y., Beverly, K., Sampaio, J., Raymo, F. M., Stoddart, J. F., and Heath, J. R. *Science* **289**, 1172 (2000).

88. Collier, C. P., Wong, E. W., Belohradský, M., Raymo, F. M., Stoddart, J. F., Kuekes, P. J., Williams, R. S., and Heath, J. R. *Science* **285**, 391 (1999).

89. Pahun, L., Campidelli, Y., d'Avitaya, F. A., and Badoz, P. A. *Appl. Phys. Lett.* **60**, 1166 (1992).

90. Xia, J.-B., Ren, S.-F., and Chang, Y.-C. *Phys. Rev. B* **43**, 1692 (1991).

91. Nogami, J., Liu, B. Z., Katkov, M. V., Ohbuchi, C., and Birge, N. O. *Phys. Rev. B* **63**, 233305 (2001).

92. Knapp, J. A., Picraux, S. T., Wu, C. S., and Lau, S. S. *Appl. Phys. Lett.* **44**, 747 (1984).

93. Youn, C., Jungling, K., and Grannemann, W. W. *J. Vac. Sci. Technol. A* **6**, 2474 (1988).

94. Kaatz, F. H., Graham, W. R., and der Spiegel, J. V. *Appl. Phys. Lett.* **62**, 1748 (1993).

95. Ragan, R., Chen, Y., Ohlberg, D. A. A., Medeiros-Ribeiro, G., and Williams, R. S. *J. Cryst. Growth* **251**, 657 (2003).

96. Perälä, R., Kuzmin, M., Laukkanen, P., Ahola-Tuomi, M., Punkkinen, M., and Väyrynen, I. *Surf. Sci.* **603**, 102 (2009).

97. Tabata, T., Argu, T., and Murata, Y. *Surf. Sci.* **179**, L63 (1987).

98. LaFemina, J. P. *Surf. Sci. Rep.* **13**, 133 (1992).

99. Ohbuchi, C. and Nogami, J. *Phys. Rev. B* **66**, 165323 (2002).

100. Chen, G., Ding, X., Li, Z., and Wang, X. *J. Phys.: Condens. Mat.* **14**, 10075 (2002).

101. Yang, J., Cai, Q., Wang, X.-D., and Koch, R. *Surf. Interface Anal.* **36**, 104 (2004).

102. Ma, C. L., Picozzi, S., Wangand, X., and Yang, Z. Q. *Eur. Phy. J. B* **59**, 297 (2007).

103. Petroff, P. M. and DenBaars, S. P. *Superlattices Microst.* **15**, 15 (1994).

104. Kuzmin, M., Laukkanen, P., Perl, R. E., Vaara, R. L., and Vyrynen, I. J. *Appl. Surf. Sci.* **222**, 394 (2004).

105. Knapp, J. A. and Picraux, S. T. *Appl. Phys. Lett.* **48**, 466 (1986).

106. Vantomme, A., Wu, M. F., Hogg, S., Wahl, U., Deweerd, W., Pattyn, H., Langouche, G., Jin, S., and Bender, H. *Nucl. Instrum. Methods* **147**, 261 (1999).

107. Pasquali, L. and Nannarone, S. *Nucl. Instrum. Methods B* **230**, 340 (2005).

108. Pasquali, L., D'Addato, S., and Nannarone, S. *Phys. Rev. B* **65**, 115417 (2002).

109. Swartzentruber, B. S., Mo, Y.-W., Webb, M. B., and Lagally, M. G. *J. Vac. Sci. Technol. A* **7**, 2901 (1989).

110. Lee, D. and Kim, S. *Appl. Phys. Lett.* **82**, 2619 (2003).

111. Liu, B. Z. and Nogami, J. *Surf. Sci.* **488**, 399 (2001).

112. Hollinger, G. and Himpsel, F. J. *J. Vac. Sci. Technol. A* **1**, 640 (1983).

113. Magaud, L., Veuillen, J. Y., Lollman, D., Nguyen Tan, T. A., Papaconstantopoulos, D. A., and Mehl, M. J. *Phys. Rev. B* **46**, 1299 (1992).

114. Woffinden, C. W., Pratt, A., Eames, C., Ménard, H., and Tear, S. P. *Phys. Rev. B* **97**, 1897 (2009).

115. Rogero, C., Polop, C., Magaud, L., Sacedon, J. L., de Andres, P. L., and Martín-Gago, J. A. *Phys. Rev. B* **66**, 235421 (2002).

116. Bonet, C., Spence, D., and Tear, S. *Surf. Sci.* **504**, 183 (2002).

117. Wood, T., Bonet, C., Noakes, T., Bailey, P., and Tear, S. *Surf. Sci.* **598**, 120 (2005).

118. Duverger, E., Palmino, F., Ehret, E., and Labrune, J.-C. *Surf. Sci.* **595**, 40 (2005).

119. Perkins, E., Bonet, C., and Tear, S. *Phys. Rev. B* **72**, 195406 (2005).

120. Roge, T., Palmino, F., Savall, C., Labrune, J., Wetzel, P., and Gewinner, G. *Phys. Rev. B* **51**, 10998 (1995).

121. Wetzel, P., Saintenoy, S., Pirri, C., Bolmont, D., Gewinner, G., Roge, T., Palmino, F., Savall, C., and Labrune, J. *Surf. Sci.* **355**, 13 (1996).

122. Martín-Gago, J., Gómez-Rodriguez, J., and Veuillen, J. *Phys. Rev. B* **55**, 5136 (1997).

123. Stauffer, L., Mharchi, A., Pirri, C., Wetzel, P., Bolmont, D., Gewinner, G., and Minot, C. *Phys. Rev. B* **47**, 10555 (1993).

124. Rogero, C., Koitzsch, C., Gonzalez, M. E., Aebi, P., Cerdá, J., and Martín-Gago, J. A. *Phys. Rev. B* **69**, 54312 (2004).

125. Cocoletzi, G. H., de la Cruz, M. T. R., and Takeuchi, N. *Surf. Sci.* **602**, 644 (2008).

126. Greeley, J. and Mavrikakis, M. *Catal. Today* **111**, 52 (2006).

127. Desplobain, S., Gautier, G., Ventura, L., and Bouillon, P. *Phys. Stat. Sol. (a)* **206**, 1282 (2009).

128. Angot, T., Koulmann, J., and Gerwinner, G. *Europhys. Lett.* **35**, 215 (1996).

129. Wetzel, P., Angot, T., Pirri, C., and Gewinner, G. *Surf. Sci.* **383**, 340 (1997).

130. Tuilier, M. H., Pirri, C., Berling, D., Bolmont, D., Gewinner, G., and Wetzel, P. *Surf. Sci.* **555**, 94 (2004).

131. Kitayama, H., Tear, S. P., Spence, D. J., and Urano, T. *Surf. Sci.* **482-485**, 1481 (2001).

132. Spence, D. J., Tear, S. P., Noakes, T. C. Q., and Bailey, P. *Phys. Rev. B.* **61**, 5707 (2000).

133. Sonnet, P., Stauffer, L., Saintenoy, S., Pirri, C., Wetzel, P., Gewinner, G., and Minot, C. *Phys. Rev. B* **56**, 15171 (1997).

134. Eames, C., Woffinden, C. W., Probert, M., Pratt, A., and Tear, S. P. *Surf. Sci.* **In Press** (2010).

135. Wachs, A. L., Miller, T., Hsieh, T. C., Shapiro, A. P., and Chiang, T. C. *Phys. Rev. B* **32**, 2326 (1985).

136. Appelbaum, J. and Hamann, D. *Phys. Rev. Lett.* **31**, 106 (1973).

137. Azizan, M., Tan, T. N., Cinti, R., Baptist, R., and Chauvet, G. *Surf. Sci.* **178**, 17 (1986).

138. Pratt, A., Woffinden, C., Bonet, C., and Tear, S. *Phys. Rev. B* **78**, 155430 (2008).

139. Qian, G.-X. and Chadi, D. *J. Vac. Sci. Technol. A* **5**, 906 (1987).

140. Takayanagi, K., Tanishiro, Y., Takahashi, M., and Takahashi, S. *Phys. Rev. Lett.* **68**, 1355 (1985).

141. Pandey, K. *Phys. Rev. B* **14**, 1557 (1976).

142. Perkins, E. W., Scott, I. M., and Tear, S. P. *Surf. Sci.* **578**, 80 (2005).

143. Bonet, C., Scott, I., Spence, D., Wood, T., Noakes, T., Bailey, P., and Tear, S. *Phys. Rev. B* **72**, 165407 (2005).

144. Rogero, C., de Andres, P. L., and Martín-Gago, J. A. *Phys. Rev. B* **71**, 165306 (2005).

145. Spence, D. J., Noakes, T. C. Q., Bailey, P., and Tear, S. P. *Phys. Rev. B.* **62**, 5016 (2000).

146. Binns, C. *Surf. Sci. Rep.* **44**, 1 (2001).

147. Eastham, D. A. and Kirkman, I. W. *J. Phys.: Condens. Mat.* **12**, L525 (2000).

148. Gonzales-Weimuller, M., Zeisberger, M., and Krishnan, K. M. *J. Magn. Magn. Mater.* **321**, 1947 (2009).

149. Binns, C. *J. Nanosci. Nanotechno.* **1**, 243 (2001).

150. Yamada, Y. and A. W. Castleman, J. *J. Chem. Phys.* **97**, 4543 (1992).

151. Sakurai, M., Watanabe, K., Sumiyama, K., and Suzuki, K. *J. Chem. Phys.* **111**, 235 (1999).

152. Martin, T. P., Bergmann, T., Göhlich, H., and Lange, T. *Chem. Phys. Lett.* **172**, 209 (1990).

153. Wolf, D. *Philos. Mag. A* **63**, 337 (1991).

154. Spencer, M. J. S., Hung, A., Snook, I. K., and Yarovsky, I. *Surf. Sci.* **513**, 389 (2002).

155. Lee, K., Callaway, J., Kwong, K., Tang, R., and Ziegler, A. *Phys. Rev. B* **31**, 1796 (1985).

156. Knickelbein, M. B. *Chem. Phys. Lett.* **353**, 221 (2002).

157. Cox, A. J., Louderback, J. G., Apsel, S. E., and Bloomfield, L. A. *Phys. Rev. B* **49**, 12295 (1994).

158. Bansmann, J., Baker, S., Binns, C., Blackman, J., Bucher, J.-P., Dorantes-Dávila, J., Dupuis, V., Favre, L., Kechrakos, D., Kleibert, A., Meiwes-Broer, K.-H., Pastor, G., Perez, A., Toulemonde, O., Trohidou, K., Tuaillon, J., and Xie, Y. *Surf. Sci. Rep.* **56**, 189 (2005).

159. Guirado-López, R. A., Dorantes-Dávila, J., and Pastor, G. M. *Phys. Rev. Lett.* **90**, 226402 (2003).

160. Billas, I. M. L., Becker, J. A., Châtelain, A., and de Heer, W. A. *Phys. Rev. Lett.* **71**, 4067 (1993).

161. Douglass, D. C., Cox, A. J., Bucher, J. P., and Bloomfield, L. A. *Phys. Rev. B* **47**, 12874 (1993).

162. Binns, C., Baker, S., Maher, M., Thornton, S., Louch, S., Dhesi, S., and Brookes, N. *Eur. Phys. J. D* **16**, 189 (2001).

163. Kneller, E. *Magnetism and Metallurgy*, 374. Academic (New York) (1969).

164. Bozorth, R. M. *Ferromagnetism*, 482. D. Van Nostand (Princeton) (1951).

165. Stoner, E. C. and Wolfarth, E. P. *Phil. Trans. Roy. Soc. A* **240**, 599 (1948).

166. Cullity, B. D. and Graham, C. D. *Introduction to Magnetic Materials*, 274. Wiley (1972).

167. Dimitrov, D. A. and Wysin, G. M. *Phys. Rev. B* **51**, 11947 (1995).

168. Weller, D., Alvarado, S. F., Gudat, W., Schröder, K., and Campagna, M. *Phys. Rev. Lett.* **54**, 1555 (1985).

169. Wei, X., Skomski, R., Balamurugan, B., Sun, Z. G., Ducharme, S., and Sellmyer, D. J. *J. Appl. Phys.* **105**, 07C517 (2009).

170. Chen, J. P., Sorensen, C. M., Klabunde, K. J., and Hadjipanayis, G. C. *J. Appl. Phys.* **76**, 6316 (1994).

171. Bødker, F., Mørup, S., and Linderoth, S. *Phys. Rev. Lett.* **72**, 282 (1994).

172. Respaud, M. *J. Appl. Phys.* **86**, 556 (1999).

173. Edmonds, K. W., Binns, C., Baker, S. H., Thornton, S. C., Norris, C., Goedkoop, J. B., Finazzi, M., and Brookes, N. B. *Phys. Rev. B* **60**, 472 (1999).

174. Edmonds, K. W., Binns, C., Baker, S. H., Maher, M. J., Thornton, S. C., Tjernberg, O., and Brookes, N. B. *J. Magn. Magn. Mater.* **220**, 25 (2000).

175. Baker, S. H., Asaduzzaman, A. M., Roy, M., Gurman, S. J., Binns, C., Blackman, J. A., and Xie, Y. *Phys. Rev. B* **78**, 014422 (2008).

176. Binns, C., Louch, S., Baker, S., Edmonds, K., Maher, M., and Thornton, S. *IEEE Trans. Magn.* **38**, 141 (2002).

177. Perez, A., Dupuis, V., Tuaillon-Combes, J., Bardotti, L., Prevel, B., Bernstein, E., Mélinon, P., Favre, L., Hannour, A., and Jamet, M. *Adv. Eng. Mater.* **6**, 475 (2005).

178. Qiang, Y., Antony, J., Sharma, A., Nutting, J., Sikes, D., and Meyer, D. *J. Nanoparticle Res.* **8**, 489 (2005).

179. Baker, S. H., Thornton, S. C., Keen, A. M., Preston, T. I., Norris, C., Edmonds, K. W., and Binns, C. *Rev. Sci. Inst.* **68**, 1853 (1997).

180. Milani, P. and deHeer, W. A. *Rev. Sci. Inst.* **61**, 1835 (1990).

181. Baker, S. H., Thornton, S. C., Edmonds, K. W., Maher, M. J., Norris, C., and Binns, C. *Rev. Sci. Instrum.* **71**, 3178 (2000).

182. Binns, C. Private Communication, (2009).

183. Granqvist, C. G. and Buhrman, R. A. *J. Appl. Phys.* **47**, 2200 (1976).

184. Upward, M. D., Cotier, B. N., Moriarty, P., Beton, P. H., Baker, S. H., Binns, C., and Edmonds, K. *J. Vac. Sci. Technol. B* **18**, 2646 (2000).

185. Vystavel, T., Palasantzas, G., Koch, S. A., and Hosson, J. T. M. D. *Appl. Phys. Lett.* **82**, 197 (2003).

186. Wang, C. M., Baer, D. R., Amonette, J. E., Engelhard, M. H., Qiang, Y., and Antony, J. *Nanotech.* **18**, 255603 (2007).

187. Saito, Y., Mihama, K., and Uyeda, R. *Japan. J. Appl. Phys.* **19**, 1603 (1980).

188. Besley, N. A., Johnston, R. L., Stace, A. J., and Uppenbrink, J. *J. Mol. Struc. - THERMOCHEM* **341**, 75 (1995).

189. Depuis, V., Perez, J. P., Tuaillon, J., Paillard, V., Mélinon, P., Perez, A., Barbara, B., Thomas, L., Fayeulle, S., and Gay, J. M. *J. Appl. Phys.* **76**, 6676 (1994).

190. Kuroda, K., Cahan, B. D., Nazri, G., Yeager, E., and Mitchell, T. E. *J. Electrochem. Soc.* **129**, 2163 (1982).

191. Wyckoff, R. W. G. *Crystal Structures*, volume 1-3. Interscience (New York), (1982).

192. Klyachko, D. and Chen, D. M. *Surf. Sci.* **446**, 98 (2000).

193. Yamauchi, Y. and Kurahashi, M. *Appl. Surf. Sci.* **169**, 236 (2001).

194. Ohnishi, S., Freeman, A. J., and Weinert, M. *Phys. Rev. B* **28**, 6741 (1983).

195. Salvietti, M., Moroni, R., Ferro, P., Canepa, M., and Mattera, L. *Phys. Rev. B* **54**, 14758 (1996).

196. Ferro, P., Moroni, R., Salvietti, M., Canepa, M., and Mattera, L. *Surf. Sci.* **407**, 212 (1998).

197. Ueda, K. and Shimizu, R. *Surf. Sci.* **43**, 77 (1974).

198. Canepa, M., Salvietti, M., Campora, A., and Mattera, L. *J. Electron Spectrosc.* **76**, 471 (1995). Proceedings of the Sixth International Conference on Electron Spectroscopy.

199. Turner, A. M. and Erskine, J. L. *Phys. Rev. B* **30**, 6675 (1984).

200. Heimann, P. and Neddermeyer, H. *Phys. Rev. B* **18**, 3537 Oct (1978).

201. Zhong, W., Overney, G., and Tománek, D. *Phys. Rev. B* **47**, 95 (1993).

202. Sun, X., Förster, S., Li, Q. X., Kurahashi, M., Suzuki, T., Zhang, J. W., Yamauchi, Y., Baum, G., and Steidl, H. *Phys. Rev. B* **75**, 035419 (2007).

203. Sinković, B., Shekel, E., and Hulbert, S. L. *Phys. Rev. B* **52**, R8696 (1995).

204. Förster, S., Baum, G., Müller, M., and Steidl, H. *Phys. Rev. B* **66**, 134427 (2002).

205. Moroni, R., Bisio, F., Canepa, M., and Mattera, L. *Surf. Sci.* **433-435**, 676 (1999).

206. Kurahashi, M., Sun, X., Entani, S., and Yamauchi, Y. *Appl. Phys. Lett.* **93**, 132505 (2008).

207. Ishii, H., Masuda, S., and Harada, Y. *Surf. Sci.* **239**, 222 (1990).

208. Clarke, A., Brookes, N. B., Johnson, P. D., Weinert, M., Sinković, B., and Smith, N. V. *Phys. Rev. B* **41**, 9659 (1990).

209. Zhang, Z. and Satpathy, S. *Phys. Rev. B* **44**, 13319 (1991).

210. Dedkov, Y. S., Rüdiger, U., and Güntherodt, G. *Phys. Rev. B* **65**, 064417 Jan (2002).

211. Jiles, D. *Introduction to Magnetism and Magnetic Materials*. Chapman and Hall (London), (1991).

212. Ko, S. P., Soh, J. Y., and Kim, Y. K. *IEEE T. Magn.* **41**, 3304 (2005).

213. Zysler, R. D., Vasquez-Mansilla, M., Arciprete, C., Dimitrijewits, M., Rodriguez-Sierra, D., and Saragovi, C. *J. Magn. Magn. Mater.* **224**, 39 (2001).

214. Tang, J., Myers, M., Bosnick, K. A., and Brus, L. E. *J. Phys. Chem. B* **107**, 7501 (2003).

215. Kataoka, K., Hattori, K., Miyatake, Y., and Daimon, H. *Phys. Rev. B* **74**, 155406 (2006).

216. Chrost, J., Hinarejos, J. J., Segovia, P., Michel, E. G., and Miranda, R. *Surf. Sci.* **371**, 297 (1997).

217. Liew, S. L., Seng, D. H. L., Tan, H. R., and Chi, D. *Mater. Res. Soc. Symp. Proc.* **1183**, FF10 (2009).

218. Sawatzky, E. *IEEE T. Magn.* **7**, 374 (1971).

219. Dubetsky, B. and Berman, P. R. *Phys. Rev. A* **58**, 2413 (1998).

220. Reakes, M. B., Eames, C., and Tear, S. P. *J. Phys: Condens. Mat.* **21**, 265001 (2009).

221. Kurahashi, M., Sun, X., and Yamauchi, Y. *Appl. Phys. Lett.* **submitted** (2009).